



Title	Surface reaction mechanisms of plasma-assisted atomic layer etching for advanced semiconductor devices
Author(s)	平田, 瑛子
Citation	大阪大学, 2021, 博士論文
Version Type	VoR
URL	https://doi.org/10.18910/85387
rights	
Note	

The University of Osaka Institutional Knowledge Archive : OUKA

<https://ir.library.osaka-u.ac.jp/>

The University of Osaka

Doctoral Dissertation

Surface reaction mechanisms of plasma-assisted
atomic layer etching
for advanced semiconductor devices

先端半導体デバイス用プラズマ支援
原子層エッチングの表面反応機構

Akiko Hirata

June 2021

Graduate School of Engineering,
Osaka University

Contents

ABSTRACT	1
CHAPTER 1 INTRODUCTION.....	4
1.1 INTRODUCTION	5
1.2 DRY ETCHING (PLASMA ETCHING)	7
1.3 PLASMA ETCHING USING HYDROGEN.....	9
1.4 ATOMIC LAYER ETCHING	10
1.5 OBJECTIVES OF THIS DISSERTATION	12
REFERENCES	15
CHAPTER 2 EXPERIMENTAL CONDITIONS	18
2.1 EXPERIMENTAL EQUIPMENT CONDITIONS	19
2.2 ANALYSIS TECHNOLOGY.....	20
REFERENCES	21
CHAPTER 3 MECHANISM OF ITO ETCHING USING H₂ PLASMA	22
3.1 INTRODUCTION	23
3.2 EXPERIMENTAL CONDITIONS.....	24
3.3 ITO ETCHING EVALUATION	25
3.4 EFFECTS OF HYDROGEN-DAMAGED LAYER ON ITO ETCHING	26
3.5 ELEMENTARY SURFACE REACTION OF ITO ETCHING USING BEAM EXPERIMENTS.....	29
3.6 REACTION MECHANISM OF ITO ETCHING	31
3.7 CONCLUSIONS	33
REFERENCES	33
CHAPTER 4 MECHANISM OF ITO CYCLIC ETCHING.....	35
4.1 INTRODUCTION	36
4.2 EXPERIMENTAL CONDITIONS.....	37
4.3 EFFECT OF HYDROGEN-INDUCED MODIFICATION.....	38
4.4 SELECTIVE ETCHING OF H-MODIFIED ITO.....	41
4.5 HIGHLY SELECTIVE CYCLIC ETCHING OVER MASK MATERIALS	43
4.6 ETCHED ITO PROFILE.....	46

4.7 CONCLUSIONS	48
REFERENCES	48
CHAPTER 5 DAMAGE RECOVERY AND LOW-DAMAGE ITO ETCHING.....	51
5.1 INTRODUCTION	52
5.2 EXPERIMENTAL CONDITIONS.....	53
5.3 ORIGIN OF THE ITO ROUGHNESS AFTER CH ₄ /H ₂ /AR PLASMA ETCHING.....	54
5.4 ANALYSIS OF ITO DAMAGES.....	56
5.5 RECOVERY OF REDUCED ITO	58
5.6 POSSIBILITY OF ITO ETCHING WITH H ₂ /CO PLASMA	61
5.7 CONCLUSIONS	64
REFERENCES	65
CHAPTER 6 SURFACE REACTION MECHANISM OF SiN ALE	67
6.1 INTRODUCTION	68
6.2 EXPERIMENTAL CONDITIONS.....	69
6.3 ACCURACY EVALUATION OF FILM THICKNESS MEASUREMENTS	71
6.4 SiN ALE ETCH STOP	72
6.5 ANALYSIS OF ETCH-STOP MECHANISM.....	74
6.6 PROPOSED SEQUENCE FOR STABLE ALE.....	77
6.7 SiN ALE FLUCTUATION	79
6.8 CONCLUSIONS	83
REFERENCES	84
CHAPTER 7 STABILIZATION OF SiN BY MULTI-STEP ALE.....	85
7.1 INTRODUCTION	86
7.2 EXPERIMENTAL CONDITIONS.....	87
7.3 MECHANISM OF SiN ETCH-STOP	89
7.4 SUPPRESSION OF ETCH-STOP AND THE ISSUE OF SURFACE OXIDATION.....	91
7.5 PLASMA-ENHANCED MULTI-STEP ATOMIC LAYER ETCHING	93
7.6 CONCLUSIONS	96
REFERENCES	97
CHAPTER 8 MECHANISM OF ALE DAMAGE GENERATION.....	99
8.1 INTRODUCTION	100
8.2 EXPERIMENTAL CONDITIONS.....	101
8.3 Si DAMAGE ANALYSIS IN SiN ALE OVER ETCH.....	102

8.4 DAMAGE ANALYSIS IN LOW ION ENERGY	104
8.5 DAMAGE REDUCTION BY A PROTECTIVE FILM	107
8.6 CONCLUSIONS	110
REFERENCES	110
CHAPTER 9 SUMMARY	112
1) MECHANISM OF ITO ETCHING USING H ₂ PLASMA	113
2) MECHANISM OF ITO CYCLIC ETCHING	113
3) DAMAGE RECOVERY AND LOW - DAMAGE ITO ETCHING	114
4) SURFACE REACTION MECHANISM OF SiN ALE	115
5) STABILIZATION OF SiN BY MULTI-STEP ALE.....	115
6) MECHANISM OF ALE DAMAGE GENERATION.....	116
RESEARCH ACHIEVEMENT	117
ACKNOWLEDGMENTS.....	122

Abstract

Semiconductor devices are constantly being reduced in size for miniaturization and high functionality. Dry etching is a key technology for fine-pattern transfer to the materials, accurate control of etched profile and minimization of damage are required. A dielectric film of SiN is widely used as a spacer material for sidewall of gate electrode and etch stop layer at the bottom of contact holes. In the sidewall spacer, high-precision anisotropic etching is performed to control the profile and dimensions of the gate stacks. In addition, damage to the underlying Si substrate during sidewall spacer/contact hole etching affects the device characteristics. Thus, highly precise etching at the atomic/molecular level and extremely low damage to the substrate are strongly required for the dielectric film etching used in the advanced semiconductor devices. Further, transparent conductive films are also used in various kind of devices. Tin-doped Indium oxide (ITO) is one of the most popular Transparent Conductive Oxide (TCO) and difficult-to-etch materials. To improve the performance of devices, precise anisotropic etching of ITO without generating damage is strongly required, similar to the conventional silicon-based materials. However, the mechanism of ITO etching is under investigation, we investigated the dry etching mechanism of ITO by using an CCP system. It has been found that ITO was reduced by incident hydrogen species in the H₂/Ar plasma, and an In-rich layer was formed on the surface. The In-rich layer had a higher sputtering yield, resulting in an increase in the etch rate in the H₂/Ar plasma. ITO etching is determined by the balance between the formation of an In-rich damaged layer by H ion irradiation and sputtering by relatively heavy inert gas ions. For application to small-dimension device fabrication, we need highly selective etching of ITO/mask materials. By applying the etching mechanism of ITO, we investigated the cyclic etching of ITO using hydrogen plasma followed by Ar plasma and developed a method to improve the etch rate selectivity for

ITO over mask materials. Cyclic etching was investigated using hydrogen plasma, followed by Ar plasma for highly selective etching of ITO/SiO₂. Silicon, which is generated from the top electrode, was deposited on the SiO₂ surface selectively during the cyclic process. Therefore, highly selective etching of ITO over SiO₂ (mask material) can be achieved by the selective surface adsorption of a protective film. And it was suggested that cyclic etching by selective surface adsorption of Si can precisely control the etch rates of ITO and SiO₂, resulting in an almost infinite selectivity for ITO over SiO₂ and in improved profile controllability. However, the residual metallic-In causes degradation of device performances, low-damage etching or damage recovery processes are urgently required. To solve these issues, we investigated the potential of both damage recovery and low-damage etching process that uses simultaneous injection of hydrogen and oxygen. When using H₂/CO plasma, the final resistivity was close to that of the initial sample. With hydrogen and oxygen-mixed plasma, we were able to achieve low-damage etching by controlling the balance between surface reduction and oxidation.

Next, we expanded the application from difficult-to-etch materials to general dielectric films, and we examined the SiN ALE of the dielectric film. When ALE is used for device manufacturing, process stability and suppression of fluctuation, which depend on the chamber conditions. We investigate SiN ALE stability with process optimization of the surface adsorption and desorption steps by using an CCP system., and we clarify the rate fluctuation mechanism. Excess polymer deposition, which originates from residual carbon after desorption step, causes the etch stop of SiN ALE. Thus, a thick residual carbon layer causes an etch stop, and suppression of C deposition is required for stable SiN ALE. Addition of O₂ to the desorption step or a three-step O₂ ashing process can suppress C deposition and realize stable ALE. Also, CF_x desorption from the chamber wall causes etch enhancement of ALE. The desorbed CF₂ enhance the EPC at the wafer edge during Ar desorption. We found that control of fluorine and carbon amounts is critical for stable SiN ALE. To realize stable SiN ALE, it is necessary to keep the same surface

conditions in every cycle. Next, the plasma source dependence of the etch-stop mechanisms are unknown. We investigate the effect of the surface condition on the stability of the EPC in SiN ALE by using an ICP system. It was confirmed the etch-stop as well as the CCP system, it is caused by polymer deposition. MD simulation shows that Si-C bonds remain on the SiN surface after the ALE process. The remaining Si-C bonds are a trigger for carbon accumulation. The etch-stop is suppressed with an O₂ flash step. However, the EPC decreases after one cycle of ALE, which is caused by the surface oxidation of SiN. For a stable ALE process, by combining the three-step SiN ALE with a subsequent SiO₂ ALE to remove residual SiO₂, multi-step ALE is realized.

One of the advantages of ALE is reported to be low-damage etching. We investigate the underlying Si damage in ALE of SiN and clarify the mechanism of damage generation, which result in the low damage etching in ALE. During over etching of the underlying Si after SiN ALE, plasma-induced damage was induced on the Si substrate. As the remaining Si damage degrades the electrical performance, precise control of the incident ion energy is indispensable to minimize damage generation. On-wafer IEDF measurement revealed that the damage thickness measured by SE was defined by the incident ion energy at the high energy peak of the IEDF. Adsorbed polymer can effectively reduce the underlying Si damage, owing to the ion energy loss in the polymer layer. Si damage generation was greatly suppressed by sequential deposition of a protective film during ALE. To suppress the damage generation during the ALE process, precise control of the ion energy, thickness of adsorbed polymer, and Ar desorption time are strongly required. For low-damage ALE, a very low ion energy is required.

CHAPTER 1

Introduction

1.1 Introduction

Semiconductor devices such as 3D NAND flash memory, Dynamic Random-Access Memory (DRAM), logic devices, image sensors, etc. are constantly being reduced in size for miniaturization and high functionality. Dry etching is a key technology for fine-pattern transfer to the materials, used in semiconductor devices. Plasma is used to remove the substrate materials in dry etching. Accurate control of etched profile and minimization of damage are required. Etching damage means defects and impurity elements in Si crystals and is known to deteriorate device characteristics. Figure 1-1 shows the technology roadmap for semiconductor logic and memory devices extracted from the International Roadmap for Devices and Systems (IRDS2020)¹⁾. As can be seen from the minimum device dimensions, fine etching of 10 nm or less is required, and therefore, etching controllability at the atomic level is indispensable. In the traditional metal-oxide-semiconductor field-effect transistors (MOSFETs), silicon dioxide (SiO₂) is the most popular gate dielectric material. SiO₂ has the excellent material and electrical properties such as sufficient insulating properties, low interface trap density, low gate leakage current and excellent thermal stability at typical Si processing temperature. Furthermore, SiO₂ has the advantage that it can be easily formed by thermal oxidation of Si. Thus, the SiO₂ has been primary choice of gate dielectric and other insulating materials in silicon-based devices.

CHAPTER 1

2020 IRDS Executive Summary Drivers-ORTC								
YEAR OF PRODUCTION	2019	2020	2022	2025	2028	2031	2032	2034
Logic device technology naming [4] NEW node definition	G54M38	G48M36	G45M24	G45M20	G40M16	G38M16T2	G38M16T3	G38M16T4
Logic industry "Node Range" Labeling (nm)	"7"	"5"	"3"	"2.1"	"1.5"	"1.0nm- eq"	"1.0nm- eq"	"0.7nm- eq"
Logic device structure options	FinFET	FinFET	FinFET LGAA	LGAA	LGAA VGAA	LGAA-3D VGAA	LGAA-3D VGAA	LGAA-3D VGAA
LOGIC CELL AND FUNCTIONAL FABRIC TARGETS								
Average Cell Width Scaling Factor Multiplier	1	0.9	0.9	0.9	0.9	0.9	0.9	0.9
LOGIC DEVICE GROUND RULES								
MPU/SoC M0 1/2 Pitch (nm) [1,2]	18	15	12	10.5	8	8	8	8
Physical Gate Length for HP Logic (nm) [3]	20	18	16	14	12	12	12	12
Lateral GAA (nanosheet) Minimum Thickness (nm)				7	6	5	5	5
Minimum Device Width (FinFET fin, nanosheet, SRAM) or Diameter (nm)	9	7	6	7	6	6	6	6
LOGIC DEVICE ELECTRICAL								
V _{dd} (V)	0.75	0.7	0.7	0.65	0.65	0.6	0.6	0.6
DRAM TECHNOLOGY								
DRAM Min half pitch (nm) [1]	18	17.5	17	14	11	8.4	8.4	7.7
DRAM Min Half Pitch (Calculated Half pitch) (nm) [1]	20.5	17.5	18.5	15	12	10	10	8.5
DRAM Cell Size Factor: aF^2 [4]	6	6	4	4	4	4	4	4
DRAM Gb/chip target	8	8	16	16	32	32	32	32
NAND Flash								
Flash 2D NAND Flash uncontacted poly 1/2 pitch – F (nm) 2D [1][2]	15	15	15	15	15	15	15	15
Flash Product highest density (independent of 2D or 3D)	612G	1T	1T	1.5T	3T	4T	4T	4T+
Flash Product Maximum bit/cell (2D, 3D) [6]	2.4	2.4	2.4	2.4	2.4	2.4	2.4	2.4
Flash 3D NAND Maximum Number of Memory Layers [6]	48-65	64-95	96-128	128-192	256-384	384-512	384-512	512+

Notes for Table ES2:

Logic Notes

[1] Industry naming convention (x0.7 with respect to earlier node) showing a full PPA (performance-power-area) gain from node cycle to another where SoC area typically scales with a 0.55-0.70x factor.

[2] Horizontal local interconnect (M0) pitch. This is in most of cases the tightest metal pitch in a SoC enabling the scaling of standard cell height. M0 pitch follows a scaling factor of 0.7-0.85x. When this scaling factor combined with the other scaling factors coming from the contacted poly pitch and design area scaling provide a full PPA (performance-power-area) gain to the next node where SoC area typically scales with a factor of 0.55-0.70x.

[3] Defined as distance between metallurgical source/drain junctions

[4] GxxMxxTx notation refers to Gxx: contacted gate pitch, Mxx: tightest metal pitch in nm, Tx: number of tiers. This notation illustrates the technology pitch scaling capability. On top of pitch scaling there are other elements such as cell height, fin depopulation, DTCC constructs, 3D integration, etc. that define the target area scaling (gates/mm²).

Fig.1-1 Semiconductor Logic / Memory Device Technology Roadmap. ¹⁾

In recent years, a high dielectric constant (high-k) materials are used instead of SiO₂ gate dielectric. However, SiO₂ is still used as the insulating materials such as interlayer/interlevel dielectric films. Further, a dielectric film of SiN is widely used as a spacer material for sidewall of gate electrode and etch stop layer at the bottom of contact holes. In the sidewall spacer, high-precision anisotropic etching is performed to control the profile and dimensions of the gate stacks. In addition, damage to the underlying Si substrate during sidewall spacer/contact hole etching affects the device characteristics, so it is necessary to reduce the damages. Thus, highly precise etching at the atomic/molecular level and extremely low damage to the substrate are strongly required for the dielectric film etching used in the advanced semiconductor devices.

Although the insulating film has been widely used from the early days of semiconductor devices, transparent conductive films are also used in various kind of devices. Tin-doped Indium

oxide (ITO) is one of the most popular Transparent Conductive Oxide (TCO) and widely used in amorphous silicon solar cells and organic electro-luminescence displays. As ITO has high optical transparency, good electrical conductivity, chemical inertness, hardness and excellent substrate adherence, ITO thin films are applied in many kinds of optical applications. In general, wet etching using hydrochloric acid or aqua regia has been used as a pattern transfer technique for ITO and IZO with a large area of 2 μm or more ^{2) 3)}. To improve the performance of devices, micro- or nano-level fine patterning of TCO are required ^{4,5)}. For this purpose, precise anisotropic etching of ITO without generating damage is strongly required, similar to the conventional silicon-based materials.

1.2 Dry etching (plasma etching)

Dry etching is also called reactive ion etching (RIE) or plasma etching. Anisotropic etching can be performed by converting the etching gas into plasma and chemically reacting the generated ions and reactive neutral species with the etched film. The major plasma sources used for dry etching can be divided into the inductively coupled plasma (ICP), capacitively coupled plasma (CCP), and electron cyclotron resonance (ECR) plasma. Figure 1-2 shows an overview of the CCP and ICP etching equipment used in this dissertation.

Halogen gas is generally used to etch the conventional dielectric material ^{6) 7) 8) 9) 10)}. During over etching of the underlying Si after SiN etching, plasma damage is generated in the underlying Si substrate. It is reported that the contact resistance fluctuates due to the plasma-induced damages generated in the Si substrate ¹¹⁾. Therefore, the damage suppression is an indispensable issue in plasma etching. The ion energy, generating the Si damage, has been analyzed, so far, and the energy required for displacement (movement from the lattice position) in a bulk Si crystal is called displacement energy ΔE_d . The minimum ΔE_d of Si is reported to be

12.5 eV and the averaged ΔE_d is reported to be 24.0 eV ¹²⁾. Due to the crystallographic structure of the solid, the displacement barrier to a lattice atom is not uniform in all directions. Furthermore, it has been reported that the outermost surface defects could be generated at a lower energy of 10 eV or less ¹³⁾. As the kinetic energy of at least 12.5 eV or more is applied to the Si atom, Si damage could be generated. Thus, precise control of incident ion energy is essential to minimize damage generation.

For transparent conductive materials such as ITO and ZnO, dry etching using chemically reactive plasma has been studied to generate fine patterns ^{10) 14) 15) 16)}. However, halogen-based reaction byproducts of InCl_3 and ZnCl_2 have very high boiling point from 700 to 800 °C (Table 1-1) ¹⁷⁾. Thus, dry etching of ITO and ZnO in chemically reactive plasma with substrate temperature in the range of conventional etching tool (< 60 °C) is difficult, and these materials are called difficult-to-etch materials. As the dry etching of ITO is basically physical sputtering-based process, the etching selectivity of ITO over mask materials are also an issue for the fine patterning ^{16) 18)}.

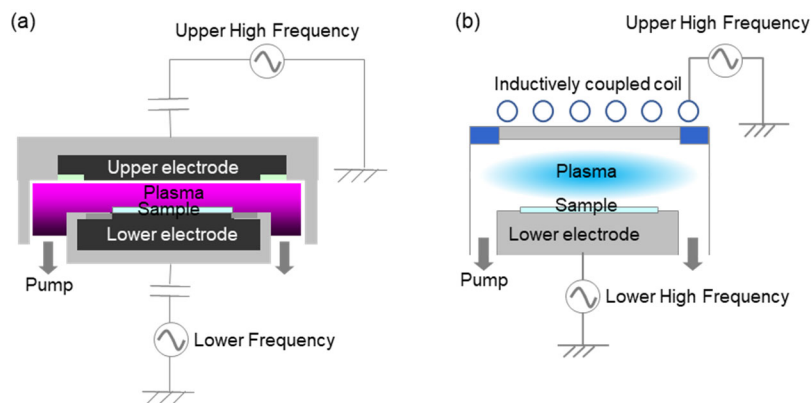


Fig.1-2 (a)CCP, (b)ICP etching equipment.

CHAPTER 1

Table 1-1 Boiling point of reaction by-product at atmospheric pressure.

reaction by-product	Boiling point [degree]
Si	3217
SiO ₂	2230
Si ₃ N ₄	-
SiF ₄	-96
SiCl ₄	57
InF ₃	>1200
InCl ₃	800
ZnF ₂	1500
ZnCl ₂	732

1.3 Plasma etching using hydrogen

It has been reported that the ITO can be etched by using H₂ ¹⁹⁾, CH₄/H₂ ¹⁴⁾ ²⁰⁾ ²¹⁾, CH₄/H₂/Ar ²²⁾, CH₄/Ar ²³⁾, CH₃OH ²⁴⁾, HBr ²⁵⁾ and HCl/CH₄ ²⁶⁾ -based (hydrogen-containing) plasmas. Therefore, the surface reaction of ITO with H and CH_x has also been studied in detail ²⁷⁾ ²⁸⁾, and it has been reported that CH₄/H₂/Ar gas improves the selectivity with the resist mask ¹⁵⁾ ²⁰⁾ ²³⁾ ²⁹⁾ ³⁰⁾. However, the mechanism of high-selective ITO etching is unclear ²²⁾ ³¹⁾. For materials other than ITO, it was clarified that ZnO etch rate was enhanced by the penetration of hydrocarbon ions ³²⁾. Hydrogen plasma was also used to etch LaAlSiO_x, which is one of the high-k materials for CMOS devices, and Co, Fe, and Ni, which are employed in magnetic tunnel junction materials for Magneto-resistive Random Access Memory (MRAM) ¹⁵⁾ ³⁰⁾ ²³⁾ ³³⁾ ³⁴⁾ ³⁵⁾ ³⁶⁾ ³⁷⁾ ³⁸⁾. It has been reported that the etch rate of magnetic materials is enhanced by adding hydrogen ³⁹⁾ ⁴⁰⁾ ⁴¹⁾. Thus, understanding of etch rate enhancement and highly selective etching of difficult-to-etch material in hydrogen-based plasma is very important in advanced devices.

Hydrogen is also important for the etching of conventional dielectric materials. $\text{CH}_3\text{F}/\text{Ar}$ and $\text{CH}_2\text{F}_2/\text{Ar}$ plasma are also generally used in the etching of SiN. In the case of SiN etching, hydrogen-incorporation with fluorocarbon-based plasma is known to improve the selectivity of SiN over SiO_2 or other mask materials, as well as the Si substrate. Therefore, it is extremely important to clarify the effect of hydrogen on the etching characteristics of both the difficult-to-etch material and the conventional dielectric films.

1.4 Atomic Layer Etching

The size of semiconductor devices is continuously being scaled down, and there is a demand for the precise control of the etched profiles and a minimization of damage during dry etching. Atomic layer etching (ALE) is a promising technology that is able to overcome these issues ^{42) 43) 44)}. ALE has been widely developed in recent years with an emphasis on Si-based, ⁴⁵⁾, dielectric-based, ^{46) 47) 48) 49) 50) 51) 52) 53) 54) 55)} and metal-based ^{56) 57) 58) 59) 60)} materials processing. In particular, logic devices are so small in size that ALE was first introduced. Since ALE has a relatively slow etch rate, it is suitable for etching film thicknesses of several 10 nm or less. The ALE generally consists of two sequential steps: the surface adsorption of a polymer and desorption steps. The desorption step can be classified into three categories that are based on chemical, physical, and thermal processes ⁶⁰⁾. Physical desorption by Ar plasma is suitable for achieving an anisotropic etched profile. One of the advantages of ALE has extremely high etch selectivity over other materials. ALE can control the ion energy at each step and the incubation time of reactive species adsorption on each materials, resulting in the highly selective etching performances ⁶¹⁾.

Another reported advantage of ALE is low damage etching, owing to the self-limited

CHAPTER 1

etching behavior. However, few reports were published related to the suppression of damage in ALE process. Thus, the mechanism of damage generation is unclear. By examining the ALE in the low energy region and analyzing and controlling the ion energy distribution on the substrate, clarification of the mechanism of ion damage generation and the damage reduction can be expected. Mechanisms of ion-induced damage generation and suppression of damage could be studied by analyzing the relationship between ion energy distribution function (IEDF) on the substrate and physical analysis of generated damages.

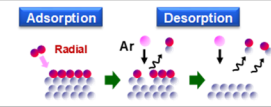
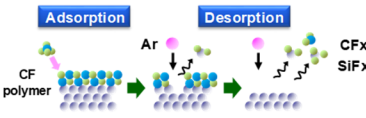
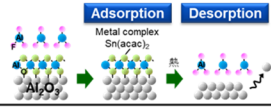
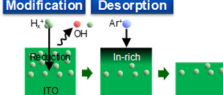
ALE for dielectric films has been developed mainly for SiO₂^{46) 47) 48) 49) 50)}. One of the applications of SiO₂ ALE is for high-aspect-ratio self-aligned contacts (SAC). SAC etching is contact hole etching of SiO₂ in the transistor fabrication formation process. By performing selective etching of the dielectric film SiO₂ over the SiN (protective film) of the gate electrode spacer, self-aligned contact can be generated, even if the overlay of lithography is misaligned. As SiO₂ ALE has a higher selectivity of SiO₂ over SiN, compared with conventional continuous wave (CW) etching, excellent SAC profiles can be obtained. SiO₂ ALE has been widely applied to advanced logic devices for the sub-7-nm technology node. In the SiO₂ ALE process, a fluorocarbon polymer is adsorbed by C₄F₈/Ar plasma, followed by the subsequent physical desorption by Ar plasma.

SiN is another important dielectric film in semiconductor devices. However, the number of published papers related to SiN ALE is much smaller than that related to SiO₂ ALE. There are two major methods of SiN ALE. The first one consists of two steps: modified layer generation by H₂ plasma and subsequent removal of the modified layer^{53) 54) 55)}. Although the physical structure and chemical modification of SiN are under investigation, hydrogen is found to be important for improving the etching performance of cyclic process. However, H_x ions generated in plasma penetrate deep into the substrate even at low energy, which may damage the substrate in device manufacturing. The second one is that the hydrofluorocarbon (HFC) polymer is adsorbed by

CHAPTER 1

$\text{CH}_3\text{F}/\text{Ar}$ plasma and the reactive layer is desorbed by Ar plasma^{51) 52) 62)}. So far, most of the papers related to SiN ALE have focused on etching performance and surface reaction mechanism. There are few papers related to the issues in SiN ALE during device manufacturing. Table 1-2 summarizes the typical examples of ALE, as described in this chapter.

Table 1-2 List of ALE examples.

ALE type	Etched film	Etching		Schematic diagram	References
		Adsorption	Desorption		
Digital etching	Si	CF_4/O_2	Ar		44
CF polymer adsorption/desorption	SiO_2	C_4F_8	Ar		45, 46
		C_4F_8 CHF_3	Ar		47
	SiO_2 SiN	C_4F_8 CHF_3	Ar		50
Thermal ALE	Al_2O_3	$\text{Sn}(\text{acac})_2$	熱		59
Modified layer generation/desorption	ITO	H_2	Ar		55

1.5 Objectives of this dissertation

The main objective of this study is to clarify the surface reaction mechanisms of anisotropic ALE for ITO and SiN. As ITO is one of the difficult-to-etch materials used in advanced semiconductor devices, the development of etching technique is crucial. In the case of SiN ALE, minimization of damage in the underlying substrate is also important issue for semiconductor manufacturing. Thus, the relationship between the incident ion energy and generated damage in the substrate was intensively studied. To apply the ALE technique to the

CHAPTER 1

manufacturing process, process stability is also important. Process fluctuation mechanism of SiN ALE, which is mainly caused by the inner wall condition of the mass production tool, was also investigated.

I categorize this dissertation into four main parts. First part in Chapter 2, I introduce equipment, analytical techniques, and flow of experimental methods. Second part, in Chapter 3, 4 and 5, I investigated the conventional plasma etching and ALE of ITO, which is one of the difficult-to-etch materials. The etching mechanism of ITO was clarified and applied its knowledge to ALE. Third part, in Chapter 6 and 7, I focus on the ALE of SiN (conventional dielectric film). The surface reaction mechanism of SiN ALE and the stabilization of ALE fluctuation was clarified. Fourth part, in Chapter 8, I studied the mechanism of damage generation in ALE and verified the reduction of damage. As described above, the high-selective processing and damage generation mechanism in SiN ALE and surface reaction mechanisms of ALE of ITO, which is one of the difficult-to-etch-materials, are clarified.

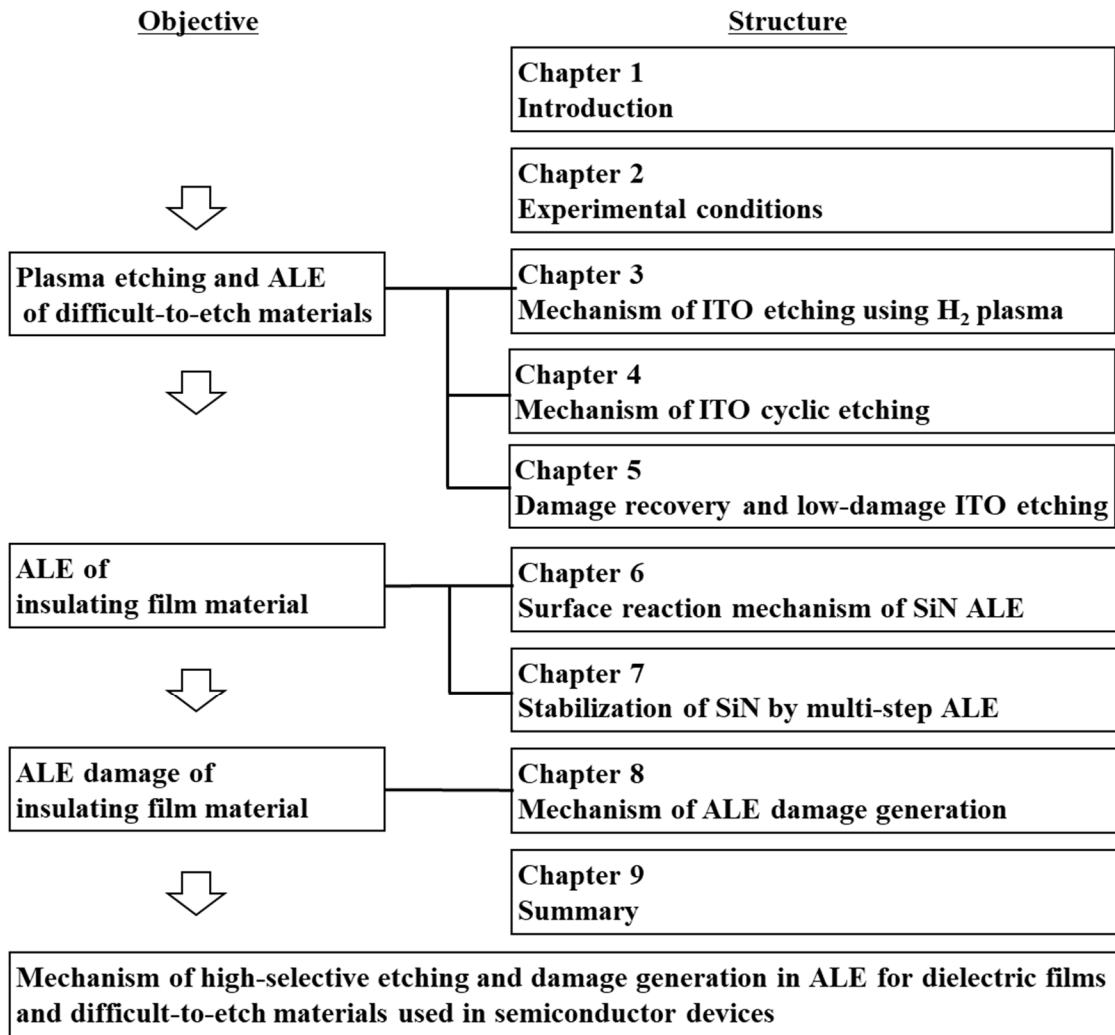


Fig.1-3 Structure of this dissertation.

1.6 References

- 1 *International Roadmap for Devices and Systems (IRDS) 2020 Edition, Executive Summary*.
- 2 T. L. Breen, P. M. Fryer, R. W. Nunes, and M. E. Rothwell: *Langmuir* **18**, 194 (2002).
- 3 C. J. Huang, Y. K. Su, and S. L. Wu: *Materials Chemistry and Physics* **84**, 146 (2004).
- 4 S. Ishibashi, Y. Higuchi, Y. Ota, and K. Nakamura: *Journal of Vacuum Science & Technology A* **8**, 1403 (1990).
- 5 Y. Ueda, J. Abe, H. Murata, Y. Gotoh, and O. Sakai: *Jpn. J. Appl. Phys.* **53**, 03dg03 (2014).
- 6 J. Molloy, P. Maguire, S. J. Lavery, and J. A. McLaughlin: *J. Electrochem. Soc.* **142**, 4285 (1995).
- 7 Y. R. Park, J. H. Ahn, J. S. Kim, B. S. Kwon, N. E. Lee, H. Y. Kang, C. K. Hwangbo, J. Ahn, and H. S. Seo: *J. Vac. Sci. Technol. A* **28**, 761 (2010).
- 8 K.-H. Kwon, A. Efremov, Y.-H. Ham, N. K. Min, H. W. Lee, M. P. Hong, and K. Kim: *J. Vac. Sci. Technol. A* **28**, 11 (2010).
- 9 K.-H. Kwon, A. Efremov, M. Kim, N. K. Min, J. Jeong, and K. Kim: *Jpn. J. Appl. Phys.* **49**, 031103 (2010).
- 10 H. B. Andagana and X. A. Cao: *J. Vac. Sci. Technol. A* **28**, 189 (2010).
- 11 J. F. Z. [<http://www.srim.org>].
- 12 E. Holmström, A. Kuronen, and K. Nordlund: *Physical Review B* **78**, 045202 (2008).
- 13 M. V. Ramana Murty and H. A. Atwater: *Phys. Rev. B* **45**, 1507 (1992).
- 14 M. Mohri, H. Kakinuma, M. Sakamoto, and H. Sawai: *Jpn. J. Appl. Phys.* **29**, L1932 (1990).
- 15 T. Meziani, P. Colpo, V. Lambertini, G. Ceccone, and F. Rossi: *Applied Surface Science* **252**, 3861 (2006).
- 16 M. Takabatake, Y. Wakui, and N. Konishi: *J. Electrochem. Soc.* **142**, 2470 (1995).
- 17 S. A. Vitale and S. Berry: *J. Vac. Sci. Technol. B* **31**, 021210 (2013).
- 18 R. Fang, W. J. Jiang, X. Guo, J. R. Han, and G. D. Shen, in *Proceedings of SPIE; Vol. 7631* (2009), p. 76310S.
- 19 T. Minami, T. Miyata, A. Iwamoto, S. Takata, and H. Nanto: *Jpn. J. Appl. Phys.* **27**, L1753 (1988).
- 20 I. Adesida, D. G. Ballegeer, J. W. Seo, A. Ketterson, H. Chang, and K. Y. Cheng: *J. Vac. Sci. Technol. B* **9**, 3551 (1991).
- 21 K. Nakamura, T. Imura, H. Sugai, M. Ohkubo, and K. Ichihara: *Jpn. J. Appl. Phys.* **33**, 4438 (1994).
- 22 D. Y. Kim, J. H. Ko, M. S. Park, and N.-E. Lee: *Thin Solid Films* **516**, 3512 (2008).
- 23 Y. J. Lee, J. W. Bae, H. R. Han, J. S. Kim, and G. Y. Yeom: *Thin Solid Films* **383**, 281

CHAPTER 1

(2001).

- 24 H. Sakaue, M. Koto, and Y. Horiike: Jpn. J. Appl. Phys. **31**, 2006 (2006).
- 25 L. Y. Tsou: J. Electrochem. Soc. **140**, 2965 (1993).
- 26 Y. Kuo: Jpn. J. Appl. Phys. **36**, L629 (1997).
- 27 S. Major, S. Kumar, M. Bhatnagar, and K. L. Chopra: Appl. Phys. Lett. **49**, 394 (1989).
- 28 H. Li, K. Karahashi, M. Fukasawa, K. Nagahata, T. Tatsumi, and S. Hamaguchi: J. Vac. Sci. Technol. A **33**, 060606 (2015).
- 29 R. J. Saia, R. F. Kwasnick, and C. Y. Wei: J. Electrochem. Soc. **138**, 493 (1991).
- 30 J. W. Lee, B. Pathangey, M. R. Davidson, P. H. Holloway, E. S. Lambers, B. Davydov, T. J. Anderson, and S. J. Pearton: J. Vac. Sci. Technol. A **16**, 2177 (1998).
- 31 M. H. Shin, M. S. Park, S. H. Jung, J. H. Boo, and N. E. Lee: Thin Solid Films **515**, 4950 (2007).
- 32 H. Li, K. Karahashi, M. Fukasawa, K. Nagahata, T. Tatsumi, and S. Hamaguchi: Jpn. J. Appl. Phys. **55**, 021202 (2016).
- 33 T. Sasaki, K. Matsuda, M. Omura, I. Sakai, and H. Hayashi: Jpn. J. Appl. Phys. **54**, 06GB03 (2015).
- 34 T. Kim, Y. Kim, J. K.-C. Chen, and J. P. Chang: J. Vac. Sci. Technol. A **33**, 021308 (2015).
- 35 N. R. Johnson, H. Sun, K. Sharma, and S. M. George: J. Vac. Sci. Technol. A **34**, 050603 (2016).
- 36 N. D. Altieri, J. K.-C. Chen, L. Minardi, and J. P. Chang: J. Vac. Sci. Technol. A **35**, 05C203 (2017).
- 37 I. Adesida, D. G. Balleger, J. W. Seo, A. Ketterson, H. Chang, and K. Y. Cheng: J. Vac. Sci. Technol. B **9**, 3551 (1991).
- 38 R. J. Saia, R. F. Kwasnick, and C. Y. Wei: J. Electrochem. Soc. **138**, 493 (1991).
- 39 T. Kim, J. K.-C. Chen, and J. P. Chang: J. Vac. Sci. Technol. A **32**, 041305 (2014).
- 40 T. Y. Lee, I. H. Lee, and C. W. Chung: Thin Solid Films **547**, 146 (2013).
- 41 J. H. Jeong, T. Endoh, Y. Kim, W. K. Kim, and S. O. Park: J. Appl. Phys. **115**, 17C727 (2014).
- 42 K. J. Kanarik, T. Lill, E. A. Hudson, S. Sriraman, S. Tan, J. Marks, V. Vahedi, and R. A. Gottscho: J. Vac. Sci. Technol. A **33**, 020802 (2015).
- 43 K. J. Kanarik, S. Tan, W. Yang, T. Kim, T. Lill, A. Kabansky, E. A. Hudson, T. Ohba, K. Nojiri, J. Yu, R. Wise, I. L. Berry, Y. Pan, J. Marks, and R. A. Gottscho: J. Vac. Sci. Technol. A **35**, 05C302 (2017).
- 44 K. J. Kanarik, S. Tan, and R. A. Gottscho: J Phys Chem Lett **9**, 4814 (2018).
- 45 Y. Horiike, T. Tanaka, M. Nakano, S. Iseda, H. Sakaue, A. Nagata, H. Shindo, S. Miyazaki, and M. Hirose: J. Vac. Sci. Technol. A **8**, 1844 (1990).

CHAPTER 1

- 46 D. Metzler, R. L. Bruce, S. Engelmann, E. A. Joseph, and G. S. Oehrlein: *J. Vac. Sci. Technol. A* **32**, 020603 (2014).
- 47 D. Metzler, K. Uppireddi, R. L. Bruce, H. Miyazoe, Y. Zhu, W. Price, E. S. Sikorski, C. Li, S. U. Engelmann, E. A. Joseph, and G. S. Oehrlein: *J. Vac. Sci. Technol. A* **34**, 01B102 (2016).
- 48 D. Metzler, C. Li, S. Engelmann, R. L. Bruce, E. A. Joseph, and G. S. Oehrlein: *J. Vac. Sci. Technol. A* **34**, 01B101 (2016).
- 49 K.-Y. Lin, C. Li, S. Engelmann, R. L. Bruce, E. A. Joseph, D. Metzler, and G. S. Oehrlein: *Journal of Vacuum Science & Technology A* **36**, 040601 (2018).
- 50 M. Honda, T. Katsunuma, M. Tabata, A. Tsuji, T. Oishi, T. Hisamatsu, S. Ogawa, and Y. Kihara: *Journal of Physics D: Applied Physics* **50**, 234002 (2017).
- 51 C. Li, D. Metzler, C. S. Lai, E. A. Hudson, and G. S. Oehrlein: *J. Vac. Sci. Technol. A* **34**, 041307 (2016).
- 52 Y. Ishii, K. Okuma, T. Saldana, K. Maeda, N. Negishi, and J. Manos: *Jpn. J. Appl. Phys.* **56**, 06HB07 (2017).
- 53 N. Posseme, V. Ah-Leung, O. Pollet, C. Arvet, and M. Garcia-Barros: *J. Vac. Sci. Technol. A* **34**, 061301 (2016).
- 54 S. D. Sherpa and A. Ranjan: *J. Vac. Sci. Technol. A* **35**, 01A102 (2017).
- 55 K. Nakane, R. H. J. Vervuurt, T. Tsutsumi, N. Kobayashi, and M. Hori: *ACS Appl. Mater. Interfaces* **11**, 37263 (2019).
- 56 A. Hirata, M. Fukasawa, T. Shigetoshi, M. Okamoto, K. Nagahata, H. Li, K. Karahashi, S. Hamaguchi, and T. Tatsumi: *Jpn. J. Appl. Phys.* **56**, 06HD02 (2017).
- 57 A. Hirata, M. Fukasawa, K. Nagahata, H. Li, K. Karahashi, S. Hamaguchi, and T. Tatsumi: *Jpn. J. Appl. Phys.* **57**, 06JB02 (2018).
- 58 T. Sasaki, K. Matsuda, M. Omura, I. Sakai, and H. Hayashi: *Jpn. J. Appl. Phys.* **54**, 06GB03 (2015).
- 59 N. Marchack, J.-I. Innocent-Dolor, M. Hopstaken, and S. Engelmann: *J. Vac. Sci. Technol. A* **38**, 022609 (2020).
- 60 Y. Lee and S. M. George: *S. M. ACS Nano* **9**, 2061 (2015).
- 61 K. Ishikawa, K. Karahashi, T. Ichiki, J. P. Chang, S. M. George, W. M. M. Kessels, H. J. Lee, S. Tinck, J. H. Um, and K. Kinoshita: *Jpn. J. Appl. Phys.* **56**, 06HA02 (2017).
- 62 A. Hirata, M. Fukasawa, K. Kugimiya, K. Nagaoka, K. Karahashi, S. Hamaguchi, and H. Iwamoto: *Jpn. J. Appl. Phys.* **59**, Sjjc01 (2020).

CHAPTER 2

Experimental conditions

2.1 Experimental equipment conditions

A commercially available dual frequency capacitively coupled plasma (CCP) reactor for 300-mm-diameter wafers was used in this study. The CCP reactor is powered by top-bottom frequency generators. Si is employed as the top electrode. The top electrode diameter is about 300 mm. The gap between the two electrodes was fixed at 35 mm. The system can control ion fluxes and ion energies independently. A very high frequency is applied to the top electrode to generate plasma, and ion fluxes can be controlled by changing the powers applied to the top frequency generators. Bottom power can control the kinetic energies of ions, which are exposed to the wafer surface. The frequency of the bottom power generator is in the range of medium frequency. Thus, the high energy peak of ion energy distribution (IED) function is almost equal to the peak-to-peak voltage (V_{pp}) of the bottom electrode. The V_{pp} was kept constant by adjusting the source power, while the bottom power was fixed. We adjusted the plasma density to keep the ion energy and ion flux constant ^{1) 2)}. The electron temperature was assumed to be 5 eV. The incident Ar flux was estimated from the plasma densities, measured using a plasma absorption probe in another experimental chamber with almost the same configurations. The pressure and lower electrode temperature were fixed at 10 mTorr and 80 °C, respectively. Our simulation shows that the high energy peak of IEDF of the bottom electrode is almost the same as V_{pp} since the frequency of the bottom rf power is not very high. The energies of Ar^+ and H_x^+ were distributed over a wide range of medium frequencies, since the ion molecular weights are small. Thus, V_{pp} is a good indicator of the maximum incident ion energy into the wafer.

ICP reactor with a source frequency of 13.56 MHz and a wafer bias frequency of 0.4 MHz was used for the ALE process. A wafer was held by an electrostatic chuck with a back-side helium cooling system. The wafer temperature was fixed at 20 °C. The pressure is 25 mTorr.

2.2 Analysis technology

The I difficult-to-etch material ITO thickness was measured with X-ray fluorescence (XRF) and X-ray reflectivity (XRR), and the ITO etch rate was calculated on the basis of the thickness differences. The atomic percentage of tin in the ITO is only 2 or 3 at. %, which hardly affects the etching characteristics. The chemical bonding in the samples was analyzed by X-ray photoelectron spectroscopy (XPS). XPS measurements were carried out with a QuanteraSXR (ULVAC-PHI) equipped with a monochromatic Al source ($h\nu = 1486.6$ eV). To evaluate the effect of single ions, we used the ion beam etching experiments. The In intensity in the film was measured using XRF, and it converted into ITO film thickness from the change in In intensity before and after etching. We had confirmed that the ITO film thickness was matched with that measured by the cross-sectional SEM and XRR. The details of the mass-selected ion beam system used in this study are presented elsewhere ³⁾. The sputtering yield of ITO is defined as the number of desorbed In atoms per injected ion. The sputtering yield was estimated from the depth of the etched ITO and ion dose. Etched depths of ITO are measured using a surface profiler (Dektak3ST). Ion doses are estimated from the ion beam current and exposure time. A cross-sectional scanning electron microscope (SEM) image was used for the profile analysis.

SiN was deposited on the Si substrate by low pressure chemical vapor deposition. The thicknesses of SiN and the HFC polymer were measured by spectroscopic ellipsometry (SE), XPS, and TEM. The optical constants of the HFC polymer were determined by SE. Fitting was performed using an HFC polymer with a thickness of approximately 6 nm. A three-layer optical model (HFC polymer/ SiN/Si) with fixed optical constants was used for the analysis of the thicknesses. The SiN film contained minimal hydrogen (2.6 at.%), while the elemental compositions of Si and N were 41.9 and 55.5 at.%. Thus, the effect of hydrogen in the SiN film could be minimized. The data were obtained using Rutherford backscattering spectrometry (RBS) and hydrogen forward scattering spectrometry (HFS). The chemical bonding of the SiN surface

was analyzed by XPS.

There are no error bars in the graphs due to insufficient data point. However, all of experiments were performed in the mass production tool that is strictly controlled to keep the sufficient repeatability of etching performances. Thus, it is confirmed that all of our experimental results are repeatable.

2.3 References

- ¹ M. Fukasawa, T. Tatsumi, K. Oshima, K. Nagahata, S. Uchida, S. Takashima, M. Hori, and Y. Kamide: *J. Vac. Sci. Technol. A* **26**, 870 (2008).
- ² K. Kinoshita, H. Utsumi, K. Suemitsu, H. Hada, and T. Sugibayashi: *Jpn. J. Appl. Phys.* **49**, 08jb02 (2010).
- ³ K. Karahashi and S. Hamaguchi: *Journal of Physics D: Applied Physics* **47**, 224008 (2014).

CHAPTER 3

Mechanism of ITO etching using H₂ plasma

3.1 Introduction

Tin-doped indium oxide (or indium tin oxide, ITO) has been widely used as a transparent electrode. Given that typical thin-film electroluminescent devices such as amorphous silicon solar cells and electroluminescent displays have a micropattern of materials, more effective micro/nanoscale processing is required^{1) 2)}. A fabrication technology of ITO has been conventionally carried out by wet etching using a mixture of hydrochloric and nitric acids. The wet etching, however, is used for ITO and IZO patterned films with a large area ($>2\text{ }\mu\text{m}$)^{3) 4)}. The application trend is dry etching of ITO using chemically reactive plasmas to control a small pattern^{5) 6)}. It has been reported that the ITO fine patterns (1.5 μm line=space) can be etched by CH_4/H_2 plasma. Halogen-based species are generally used as source gases for the etching of conventional materials^{7) 8) 9) 10) 11)}. However, the halogen-containing reaction by-products of indium have boiling points of 700–800 °C, which cause difficulties during dry etching¹²⁾. The other issue is the low etch selectivity to the photoresist mask on ITO pattern etching^{13) 14)}. On the other hand, the ITO dry etching can be performed by using hydrogen-containing plasma (methane, hydrogen, etc.), and the etch selectivity to the photoresist mask during ITO dry etching improved using the deposition of $\alpha\text{-C:H}$ layers on the top of the mask by $\text{CH}_4/\text{H}_2/\text{Ar}$ ^{6) 15) 16) 17) 18)}. However, the mechanism of ITO etching is under investigation^{19) 20)}. Herein, we investigated the dry etching mechanism of ITO. Our previous beam study revealed that the etch rate of ZnO, which is one of the well-known transparent conductive oxides, was enhanced by the energetic incidence of hydrocarbon ions²¹⁾. Moreover, other research papers also reported that the etch rates of high-k materials such as LaAlSiO_x of metal–oxide–silicon devices and magnetic tunnel junction materials such as Co, Fe, and Ni of magnetic random access memory devices were enhanced by the addition of hydrogen^{22) 23)}. In this paper, we investigated the effects of the hydrogen-damaged layer on ITO etching caused by H_2/Ar plasma using several surface analysis techniques.

3.2 Experimental conditions

We used an ITO (50 nm)/SiO₂(100 nm)/Si sample in H₂/Ar plasma. The ITO was sputtered from an In₂O₃:SnO₂ (90:10 wt%) target in an argon-oxygen atmosphere using a DC magnetron sputtering system. It was deposited at 2.2mTorr with 800W dc power. The deposition temperature was 25⁰C. After deposition, the samples were postannealed at 350⁰C. CCP system was used in this study. The V_{pp} was kept constant at 960 ± 30V by adjusting the source power, while the bottom power was fixed at 500 W. The flow rate ratio of the H₂/Ar plasma was varied while the total flow rate was kept constant at 400 sccm. The etching time was 30 s. The damaged ITO layer created by the H₂/Ar plasma exposure was measured by transmission electron microscopy (TEM). The penetration depth of H/Ar ions into the ITO was simulated by TRIM simulation ²⁴⁾. The quantitative amount of hydrogen penetrated into the ITO surface was investigated by thermal desorption spectroscopy (TDS). The ITO sample is a 1 cm by 1 cm square chip, which was heated to 60–400 ⁰C to measure the thermal desorption of hydrogen. For the quantitative analysis of hydrogen, the correlation between the amount of hydrogen in the film and the ion currents in the TDS system was used. After known amounts of hydrogen ions were implanted in the SiO₂/Si substrate, the integration of ion currents of desorbed H₂ during heating in the TDS system was measured. As a result, the proportional relationship between the implanted H⁺ doses and the integration of ion currents of H₂ measured by the TDS system was determined. Using this relationship, we can estimate the quantitative amount of hydrogen in the films. We measured the chemical state of In–In and In–O on the surface of ITO. To clarify the effects of hydrogen in ITO etching reactions, the ion beam etching experiments for ITO surfaces using H⁺, He⁺, Ne⁺, and Ar⁺ were performed. The accelerated energy of inert-gas ions, i.e., He⁺, Ne⁺, and Ar⁺, was constant at 1000 eV, while that of H⁺ was 500 eV.

3.3 ITO Etching evaluation

Figure 3-1 shows the etch rates of ITO in H_2/Ar plasma achieved by varying the flow rate ratio. The ITO etch rate increased after the addition of a small amount of hydrogen in region A (Ar-rich), gradually decreased in region B, and decreased markedly in region C (hydrogen-rich). The ITO etch rate was found to strongly depend on the H_2/Ar flow rate ratio.

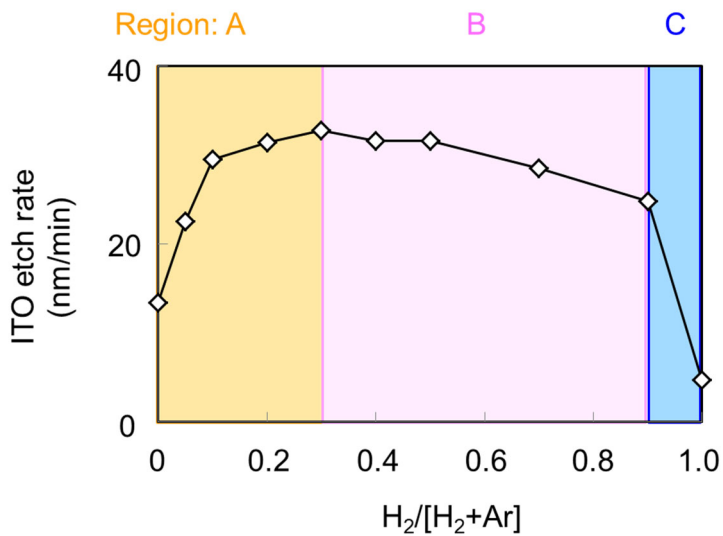


Fig.3-1 Rate of ITO etching by $H_2=Ar$ plasma.

Figure 3-2(a) shows cross-sectional analyses of the ITO after H_2/Ar plasma irradiation obtained by TEM. The ITO sample in region A was $H_2/[H_2+Ar]=0$, that in region B was $H_2/[H_2+Ar]=0.4$, and that in region C was $H_2/[H_2+Ar]=1$. It was confirmed that a thin damaged layer was generated in region A, whereas a deeper damaged layer was observed in regions B and C. The damaged layer in regions B has non-uniform gray/white contrast, because the density of H atoms penetrating deep into the film is lower than that in the pure H_2 plasma (region C). The density of the damaged layer is microscopically disordered, especially under the low-H-dose

condition (region B).

Figure 3-2(b) shows the penetration depths of H/Ar ions into the ITO simulated by TRIM. The film density of ITO was estimated to be 6.9 g/cm^3 . The incident angle of ions was fixed at 90° from the surface. The results show that the damaged layer thickness is relatively consistent with the penetration depth of the dominant ion species. Because H_3^+ is known to be the dominant ion species in pure H_2 plasma^{25) 26)}, the kinetic energy of incident H_3^+ was assumed to be divided equally into every three H atoms on the surface (320 V).

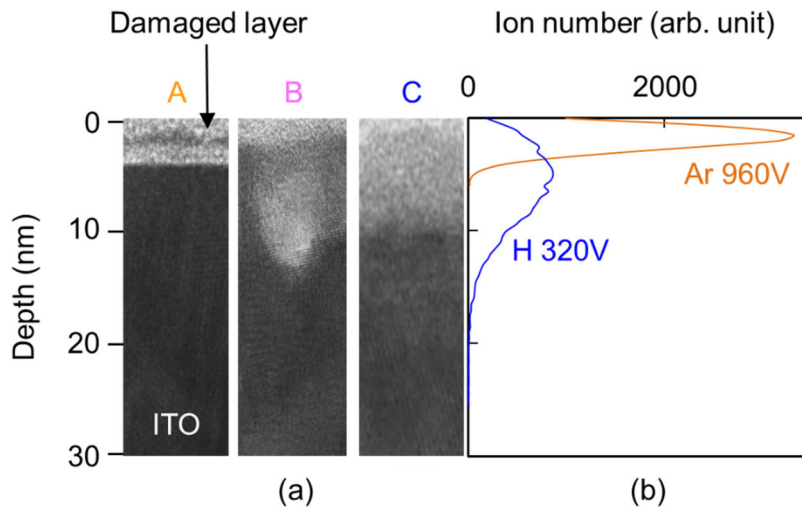


Fig.3-2 (a) H=Ar ion penetration depth in ITO: TEM and (b) TRIM simulation.

3.4 Effects of hydrogen-damaged layer on ITO etching

To investigate the effect of the hydrogen-induced damage in detail, the etch rate of ITO in Ar plasma after exposure to H_2 plasma was analyzed. Figure 3-3 shows the dependence of the ITO etch rate during subsequent constant Ar plasma exposure on the H_2 irradiation time. The H_2 irradiation time was varied from 0 to 15 s. The ITO etch rate increased with H_2 irradiation time.

Figure 3-4 shows ITO etch rate as a function of the amount of H_2 in the ITO measured by TDS. The inset figure shows H_2 ion spectra with different H exposure times. We found that a longer H_2 exposure time caused a larger H_2 ion current. There are two peaks. The peak at low temperature shows weak bonds such as van der Waals' force and the peak at high temperature shows strong hydrogen bonding. In this experiment, we use the two peaks to estimate the amount of hydrogen. We estimated desorbed H_2 using the integral value from 60 to 400 °C. The longer the H_2 irradiation time, the larger the amount of H_2 that existed in the etched ITO. We confirmed that the amount of background H_2 desorption was negligible. The amount of H_2 in the ITO was found to be almost proportional to the etch rate. Thus, we found that the hydrogen injection has a strong impact on the etch rate enhancement.

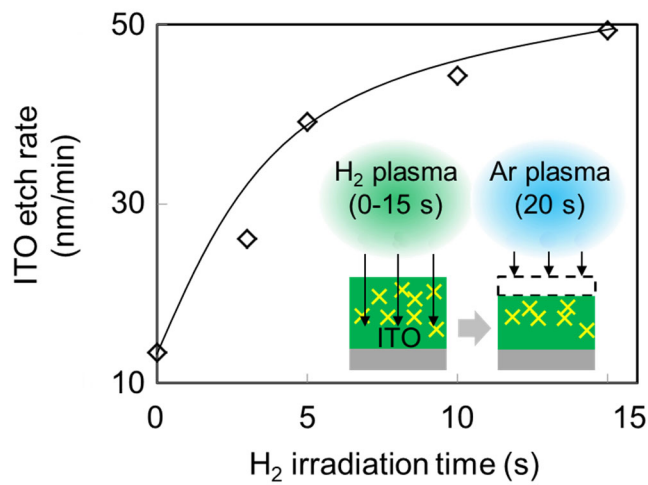


Fig.3-3 Dependence of ITO etch rate on H_2 irradiation time.

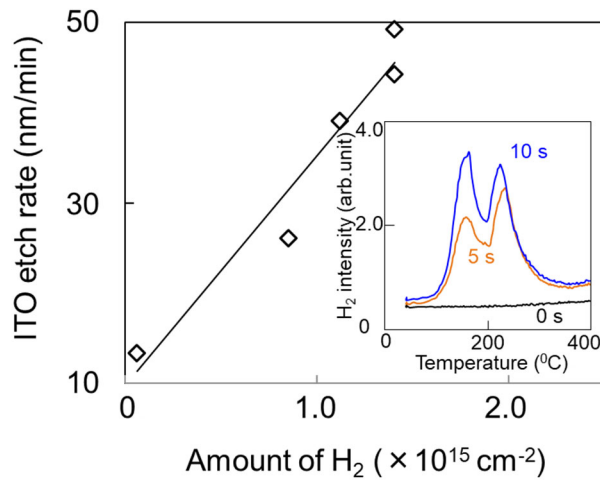


Fig.3-4 Dependence of ITO etch rate on amount of H₂.

In region B, reduction in the partial pressure of Ar caused the ITO etch rate to decrease. Because the Ar flux decreased with increasing H₂ partial pressure, we investigated the Ar flux dependence of the ITO etch rate with constant hydrogen-induced damage. A higher Ar ion flux was found to increase the ITO etch rate (Fig. 3-5). We speculate that the reduction in the Ar flux was the dominant contributor to the gradual decline in the etch rate observed in region B.

In region C (hydrogen-rich), the dominant mass number of incident ion species markedly changed. As the sputtering yield caused by light mass ions is normally much smaller than that by heavy mass ions, the etch rate of ITO decreased markedly in the hydrogen-rich gas chemistry.

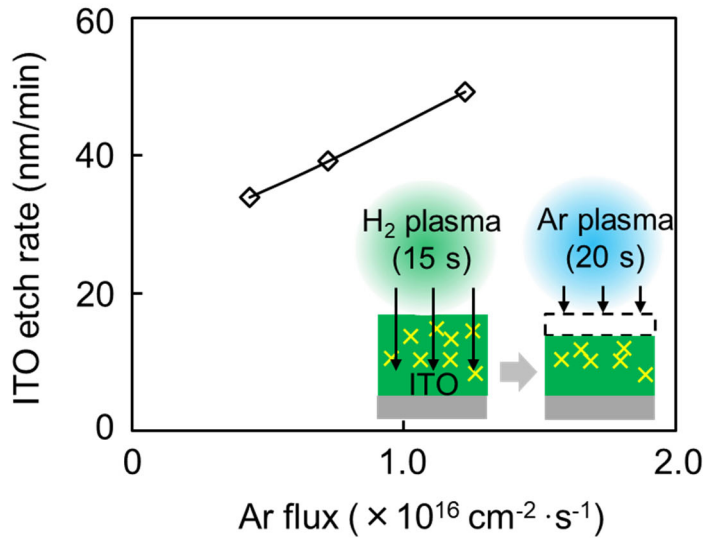


Fig.3-5 Dependence of ITO etch rate on Ar flux.

3.5 Elementary surface reaction of ITO etching using beam experiments

In the case of conventional dry etching, many kinds of species such as ions, radicals, and photons are irradiated on the surface simultaneously. Thus, the surface reactions during dry etching are very complicated. To simplify the elemental reactions between injected H^+ and ITO surfaces, we employed a mass-selected ion beam system [Fig. 3-6(a)]. After H^+ irradiation to the ITO surface, the sputtering yield of Ne^+ was analyzed [Fig. 3-6(b)]. The ion doses of H^+ and Ne^+ were $1 \times 10^{17} \text{ (ions/cm}^2\text{)}$. The enhancement in etch rate caused by H ions was similarly confirmed. The result clearly shows that the hydrogen ion plays a dominant role in etch rate enhancement of ITO etching.

To clearly explain the reason for the etch rate reduction in region C, we also investigated the dependence of the ITO sputter yield on mass number using beam experiments [Fig. 3-6(a)]. The ITO sputter yield was found to be strongly dependent on the incident mass number of the

CHAPTER 3

inert-gas ions (Fig. 3-7)²⁵⁾. In the hydrogen plasma, the dominant ion species are reported to be H_3^+ , H_2^+ , and H^+ ^{27) 28)}. Because the mass numbers of H_3^+ , H_2^+ , and H^+ are very small, the etch rate markedly decreased in region C (Fig.3-1).

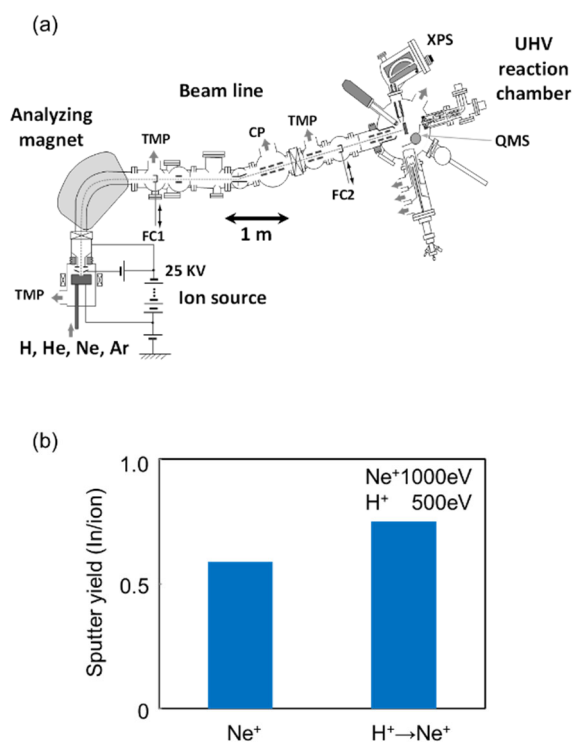


Fig.3-6 Dependence of ITO etch rate on Ar flux.

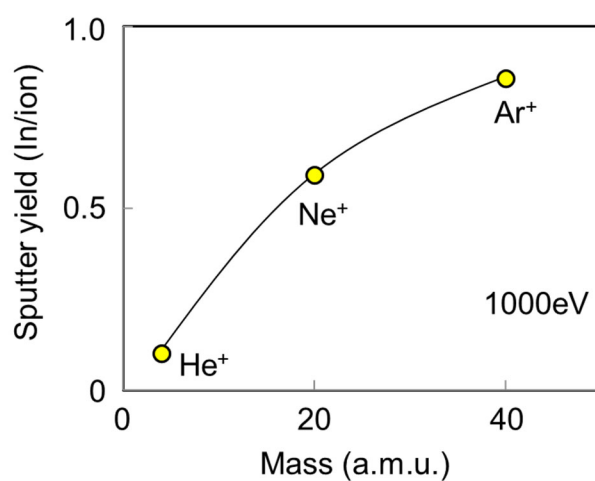


Fig.3-9 Proposed reaction mechanism of ITO etching by H_2/Ar plasma.

3.6 Reaction mechanism of ITO etching

The hydrogen ion injection into the ITO can cause physical damage, chemical bonding scission, and chemical composition variation. To investigate the etch rate enhancement mechanisms, the chemical bonding on the ITO surface was analyzed by XPS before and after H_2/Ar plasma exposure [Fig. 3-8(a)]. The ITO sample was $H_2/[H_2+Ar]=0.5$, and the H_2/Ar plasma exposure time was 30 s. High-resolution In ($3d_{5/2}$) electron emission spectra were deconvoluted into the chemical contributions of metallic In (443.11 eV), In_2O_3 (444.32 eV), and $In(OH)_3$ (444.85 eV) using a least-squares fitting technique including Gaussian peaks and a linear background. XPS results revealed that the ITO was reduced by hydrogen injection, which generated an In-rich layer on the surface. The reduction of ITO by hydrogen could generate the volatile OH_x radicals as reaction by-products. Thus, we analyzed the OH radical with Si or ITO substrate by optical emission spectroscopy (OES). The ratio of OH emission intensity (307 nm) to that of Ar (750.5 nm) is shown in Fig. 3-8(b). With the ITO substrate, the marked increase in the emission intensity of OH was observed. We confirmed that the In-rich layer after H_2/Ar plasma exposure was generated by the reduction of the ITO surface.

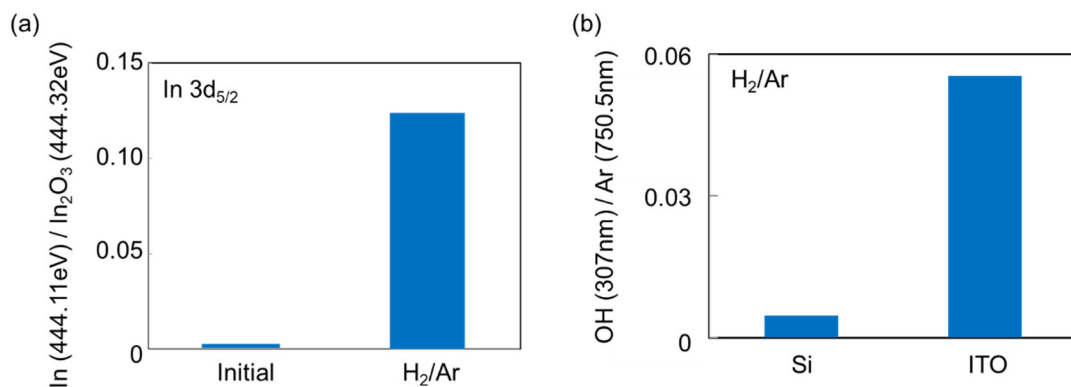


Fig.3-8 (a) XPS area ratio of In–In/In–O before and after H_2/Ar plasma exposure and

(b) OES ratio of OH/Ar with Si or ITO substrate.

We also analyzed the surface metal composition by cross-sectional TEM equipped with an energy dispersive X-ray spectrum (EDS) (not shown here). We also confirmed that the metallic In-rich layer and agglomerated In were generated on the ITO surface during H_2/Ar plasma etching. Figure 3-9 shows the proposed reaction mechanism of ITO etching in H_2/Ar plasma. The ITO was reduced by incident hydrogen species in the H_2/Ar plasma, thereby forming an In-rich layer. Because indium is reported to have a higher sputtering yield (3.1 atom/ion) than ITO (0.9 atom/ion)²⁶⁾, the etch rate was increased in the H_2/Ar plasma. These sputtering yields were measured for bombardment with Ar ions at normal incidence (90°). The energy is 1 keV. In the beam study²⁵⁾, the surface reduction of ITO takes place especially with the low-energy incidence of CH_x^+ ions (< 1000 eV). In this etching experiment, the H incident energy is roughly 300 eV, since the dominant ion species in the H_2/Ar plasma is H_3^+ . The low-energy incidence of H ions (~ 300 eV) could cause the effective surface reduction of the ITO surface. The incident H ion also causes physical damage in the ITO films. Further analysis is required to clarify the contribution of physical damage to the ITO etch rate enhancement.

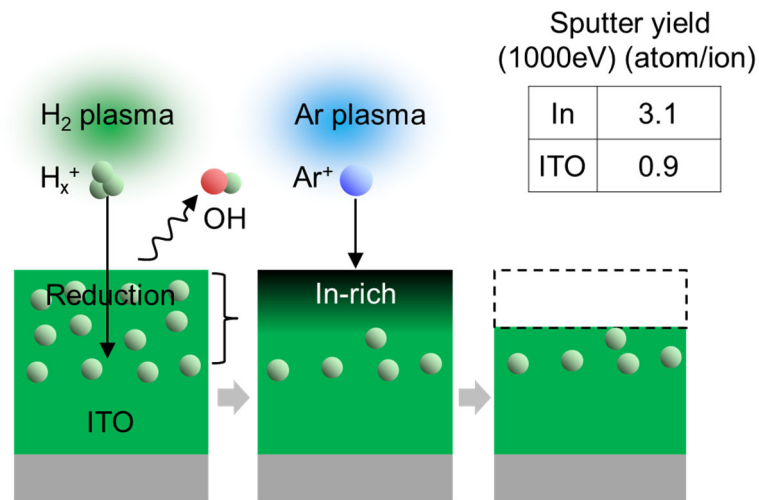


Fig.3-9 Proposed reaction mechanism of ITO etching by H_2/Ar plasma.

3.7 Conclusions

The etch rate of ITO and the effects of a hydrogen-damaged layer caused by H₂/Ar plasma were investigated using several surface analysis techniques. The ITO etch rate in H₂/Ar plasma increased to about three times that with Ar plasma. ITO was reduced by incident hydrogen species in the H₂/Ar plasma, and an In-rich layer was formed on the surface. The In-rich layer had a higher sputtering yield, resulting in an increase in the etch rate in the H₂/Ar plasma. ITO etching is determined by the balance between the formation of an In-rich damaged layer by H ion irradiation and sputtering by relatively heavy inert gas ions.

3.8 References

- ¹ S. Ishibashi, Y. Higuchi, Y. Ota, and K. Nakamura: *Journal of Vacuum Science & Technology A* **8**, 1403 (1990).
- ² Y. Ueda, J. Abe, H. Murata, Y. Gotoh, and O. Sakai: *Jpn. J. Appl. Phys.* **53**, 03dg03 (2014).
- ³ T. L. Breen, P. M. Fryer, R. W. Nunes, and M. E. Rothwell: *Langmuir* **18**, 194 (2002).
- ⁴ C. J. Huang, Y. K. Su, and S. L. Wu: *Materials Chemistry and Physics* **84**, 146 (2004).
- ⁵ M. Mohri, H. Kakinuma, M. Sakamoto, and H. Sawai: *Jpn. J. Appl. Phys.* **29**, L1932 (1990).
- ⁶ T. Meziani, P. Colpo, V. Lambertini, G. Ceccone, and F. Rossi: *Applied Surface Science* **252**, 3861 (2006).
- ⁷ J. Molloy, P. Maguire, S. J. Lavery, and J. A. McLaughlin: *J. Electrochem. Soc.* **142**, 4285 (1995).
- ⁸ Y. R. Park, J. H. Ahn, J. S. Kim, B. S. Kwon, N. E. Lee, H. Y. Kang, C. K. Hwangbo, J. Ahn, and H. S. Seo: *J. Vac. Sci. Technol. A* **28**, 761 (2010).
- ⁹ K.-H. Kwon, A. Efremov, Y.-H. Ham, N. K. Min, H. W. Lee, M. P. Hong, and K. Kim: *J. Vac. Sci. Technol. A* **28**, 11 (2010).
- ¹⁰ K.-H. Kwon, A. Efremov, M. Kim, N. K. Min, J. Jeong, and K. Kim: *Jpn. J. Appl. Phys.* **49**, 031103 (2010).
- ¹¹ H. B. Andagana and X. A. Cao: *J. Vac. Sci. Technol. A* **28**, 189 (2010).
- ¹² S. A. Vitale and S. Berry: *J. Vac. Sci. Technol. B* **31**, 021210 (2013).
- ¹³ M. Takabatake, Y. Wakui, and N. Konishi: *J. Electrochem. Soc.* **142**, 2470 (1995).

CHAPTER 3

- ¹⁴ R. Fang, W. J. Jiang, X. Guo, J. R. Han, and G. D. Shen, in *Proceedings of SPIE; Vol. 7631* (2009), p. 76310S.
- ¹⁵ I. Adesida, D. G. Ballegeer, J. W. Seo, A. Ketterson, H. Chang, and K. Y. Cheng: *J. Vac. Sci. Technol. B* **9**, 3551 (1991).
- ¹⁶ R. J. Saia, R. F. Kwasnick, and C. Y. Wei: *J. Electrochem. Soc.* **138**, 493 (1991).
- ¹⁷ J. W. Lee, B. Pathangey, M. R. Davidson, P. H. Holloway, E. S. Lambers, B. Davydov, T. J. Anderson, and S. J. Pearton: *J. Vac. Sci. Technol. A* **16**, 2177 (1998).
- ¹⁸ Y. J. Lee, J. W. Bae, H. R. Han, J. S. Kim, and G. Y. Yeom: *Thin Solid Films* **383**, 281 (2001).
- ¹⁹ M. H. Shin, M. S. Park, S. H. Jung, J. H. Boo, and N. E. Lee: *Thin Solid Films* **515**, 4950 (2007).
- ²⁰ D. Y. Kim, J. H. Ko, M. S. Park, and N.-E. Lee: *Thin Solid Films* **516**, 3512 (2008).
- ²¹ H. Li, K. Karahashi, M. Fukasawa, K. Nagahata, T. Tatsumi, and S. Hamaguchi: *Jpn. J. Appl. Phys.* **55**, 021202 (2016).
- ²² T. Kim, J. K.-C. Chen, and J. P. Chang: *J. Vac. Sci. Technol. A* **32**, 041305 (2014).
- ²³ T. Sasaki, K. Matsuda, M. Omura, I. Sakai, and H. Hayashi: *Jpn. J. Appl. Phys.* **54**, 06GB03 (2015).
- ²⁴ J. F. Z. [<http://www.srim.org>].
- ²⁵ H. Li, K. Karahashi, M. Fukasawa, K. Nagahata, T. Tatsumi, and S. Hamaguchi: *J. Vac. Sci. Technol. A* **33**, 060606 (2015).
- ²⁶ M. P. Seah: *Nucl. Instrum. Methods Phys. Res., Sect. B* **229**, 348 (2005).
- ²⁷ M. Fukasawa, T. Tatsumi, K. Oshima, K. Nagahata, S. Uchida, S. Takashima, M. Hori, and Y. Kamide: *J. Vac. Sci. Technol. A* **26**, 870 (2008).
- ²⁸ L. Tong: *Jpn. J. Appl. Phys.* **54**, 06GA01 (2015).

CHAPTER 4

Mechanism of ITO cyclic etching

4.1 Introduction

ITO has been widely used for transparent electrodes. Thus, we investigated the etching mechanism of ITO. We previously proposed an ITO etching method using H_2/Ar plasma, wherein the balance is maintained between the formation of an In-rich layer modified by H ion irradiation and sputtering with relatively heavy inert gas ions ^{1) 2)}. In beam experiments, we also found that the ITO sputter yield is highly dependent on the incident mass number of inert gas ions ^{3) 4)}. The problems inherent in this ITO etching method, however, are its low etch rate and low selectivity against hard-mask materials ^{5) 6)}. To solve these problems, herein we investigated the effect of the hydrogen-induced modified layer for cyclic, multistep thin-layer etching. One of the advantages of cyclic etching is the possibility of adjusting the ion energy in each step; thus, highly selective etching can be expected ⁷⁾. When we use the differences in precursor incubation time among different materials effectively, highly selective etching is also expected. The suppression of the deposition of reaction byproducts and their accumulation on the surface or chamber wall is also possible using the cyclic process ^{8) 9)}. By quickly alternating the adsorption and etching steps, there is a possibility to realize a more stable process than the conventional CW plasma process. By carefully choosing the appropriate gas chemistry in the etching step, the deposition of reaction byproducts on the chamber wall can be refreshed every cycle without accumulating deposits. Thus, we carried out cyclic etching to improve the performance of ITO etching.

Recently, hydrogen plasma has been employed for difficult-to-etch materials ^{10) 11) 12) 13) 14) 15) 16) 17) 18) 19)}. Hydrogen effectively enhances the etch rates of magnetic materials in a magnetoresistive random access memory (MRAM) stack ^{10) 20) 21)}. In addition, the self-limited etching of silicon nitride, which is a commonly used dielectric material in conventional semiconductor devices, has also been demonstrated using hydrogen plasma ²²⁾. The process consists of two sequential steps—surface modification in hydrogen plasma followed by the

removal of modified layers in fluorinated plasma. Although the structural and chemical modifications of silicon nitride by hydrogen plasma are under investigation, hydrogen has been found to play an important role in improving the etching performance of the cyclic process.

ITO is one of the difficult-to-etch materials, since the boiling points of indium halides are very high ($> 700\text{ }^{\circ}\text{C}$)²³⁾. The ITO patterning of microscale and larger features has been carried out by wet etching using hydrochloric acid or aqua regia^{24) 25)}. For the patterning of nanoscale features, we usually use dry etching with chemically reactive plasmas^{26) 27) 28)}. For application to small-dimension device fabrication, we need highly selective etching of ITO/mask materials. In this study, we investigated the cyclic etching of ITO using hydrogen plasma followed by Ar plasma and developed a method to improve the etch rate selectivity for ITO over mask materials.

4.2 Experimental conditions

ITO (50 nm) was deposited by sputtering on a SiO_2/Si substrate. ITO was sputtered from an $\text{In}_2\text{O}_3\text{--SnO}_2$ (90 wt–10 wt %) oxide target in Ar/O_2 ambient using a DC magnetron sputtering system. Postdeposition annealing was performed at a high temperature. The upper peak-to-peak voltage (V_{pp}) was 800 V with H_2 plasma exposure. The roughly estimated V_{dc} was about 410 eV. Our simulation shows that the high energy peak of ion energy distribution function (IEDF) is about 500 eV at the Si top electrode (not shown). The maximum the ion energy, incident to the Si top electrode, is close to V_{dc} . As the frequency of the top electrode was high, the energy dispersion of IEDF was narrow ($< \pm 100\text{ eV}$). A Si wafer was electrostatically chucked on the stage of the bottom electrode. The peak-to-peak voltage (V_{pp}) of the bottom electrode was varied from 630 to 960 V. The flow rate of H_2 or Ar plasma was kept constant at 400 sccm. One etching cycle consisted of two steps: First, a hydrogen-plasma-induced modified surface was generated to activate the ITO surface, and then an Ar plasma was used to selectively etch the modified layer.

ITO modified layer reduced by H_2 plasma exposure was analyzed by transmission electron microscopy (TEM). The penetration depth of a H ion into the ITO layer was simulated by TRIM simulations²⁸⁾, and the etched ITO profile was analyzed by scanning electron microscopy (SEM). We measured the Si concentration on the surface of ITO by using XPS. For the analysis of etched profiles, we used a SiO_2 (70 nm)/ITO (50 nm)/ SiO_2 /Si sample, and an upper SiO_2 layer (trench pattern) was employed as the hard-mask. Conventional TEOS (tetraethylorthosilicate)-based chemical vapor deposition processes have been utilized to deposit the hard mask SiO_2 . The substrate temperature was kept at 400°C. After etching the upper SiO_2 mask with conventional fluorocarbon gas chemistry, the photoresist was removed via an ashing process.

4.3 Effect of hydrogen-induced modification

To investigate the effect of hydrogen-induced modification, the etch rate of ITO in Ar plasma after exposure to H_2 plasma was analyzed (Fig. 4-1). Figure 4-2 shows the dependence of ITO etch rate during the subsequent continuous Ar plasma exposure on H_2 plasma irradiation time. The ITO etch rate in pure Ar plasma was 17 nm/min, whereas the maximum etch rate of cyclic etching (1 cycle) was 51 nm/min. We found that the ITO etch rate using cyclic etching increased to about three times that using only Ar plasma. Although the mechanism of etch rate enhancement is described in detail elsewhere¹⁾, the reduction of ITO by hydrogen injection must be a key factor for the etch rate increase. Recently, a beam study has indicated that the etching enhancement is also related to the forming of a structurally modified layer, where the grain size of structures is changed^{2) 29) 30)}. Further analysis is required to clarify the effect of chemical and/or physical modification of the ITO surface on the etch rate increase.

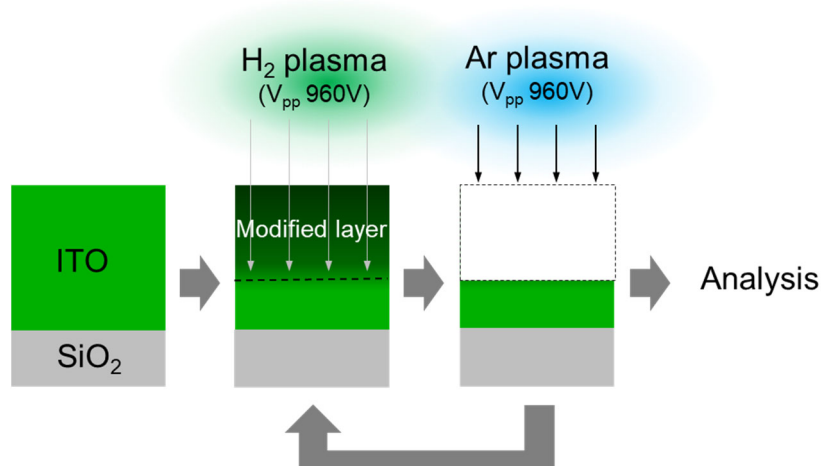


Fig.4-1 Experiment on ITO cyclic etching with H₂ and Ar plasmas.

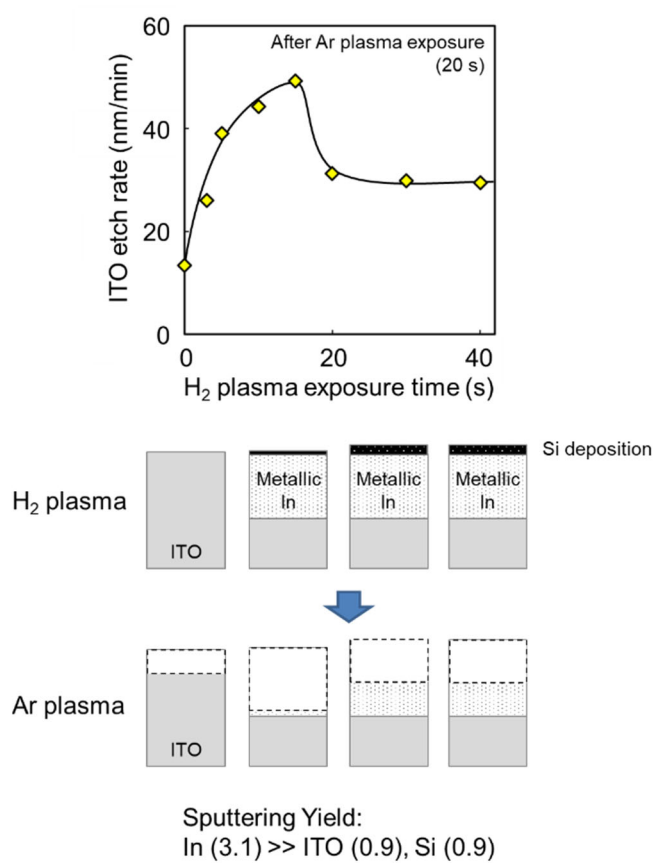


Fig.4-2 Dependence of ITO etch rate on H₂ plasma exposure time.

CHAPTER 4

When the H₂ plasma irradiation time was longer than 20 s, the ITO etch rate decreased and became constant at about 30 nm/min. The reason for the decrease in ITO etch rate is assumed to be the following: (a) Si was generated from the upper electrode and/or other chamber parts ³¹⁾, or (b) ITO surface densification/modification occurred after a long H₂ plasma exposure (>20s). Specifically, excessive H₂ plasma exposure suppressed ITO etching owing to the generation of a protective surface layer. To determine the root cause of etch rate decrease, the ITO surface was analyzed by XPS. Figure 4-3 shows the Si concentration of the ITO surface without and with H₂ plasma exposure. Si is detected on the ITO surface after a long H₂ plasma exposure (40 s). The ITO surface was also analyzed by XRR to investigate ITO surface densification (not shown here). The ITO surface density after a long H₂ plasma exposure (40 s) was almost the same as that before the H₂ plasma exposure. These results clearly show that the reason for the ITO etch rate decrease is the deposition of Si generated from the chamber parts.

Figure 4-3 also shows that the ITO etch rate during H₂ plasma exposure for 20 to 40 s is almost constant. When Si is deposited from the chamber wall continuously, the ITO etch rate decreases as a function of H₂ plasma exposure time. We speculated that the reason why the ITO etch rate is constant in this exposure time is as follows: During H₂ plasma exposure, Si desorbs owing to the generation of SiH_x from the chamber parts. The generated SiH_x reacts with oxygen in the ITO surface and generates OH_x. As a result, Si is deposited on the ITO surface. Once the ITO surface is covered with Si (no oxygen), OH_x cannot be generated and excessive Si deposition is suppressed. Thus, the ITO etch rate becomes constant after 20 s of H₂ plasma exposure. The Ar sputtering yield of Si at an energy of 1000 eV is about 0.9 atoms/ion. As the sputtering yield of Si is three times lower than that of metallic In (3.1 atoms/ion), for ITO etching during H₂ plasma exposure for 20 to 40 s becomes much slower than that for 15 s.

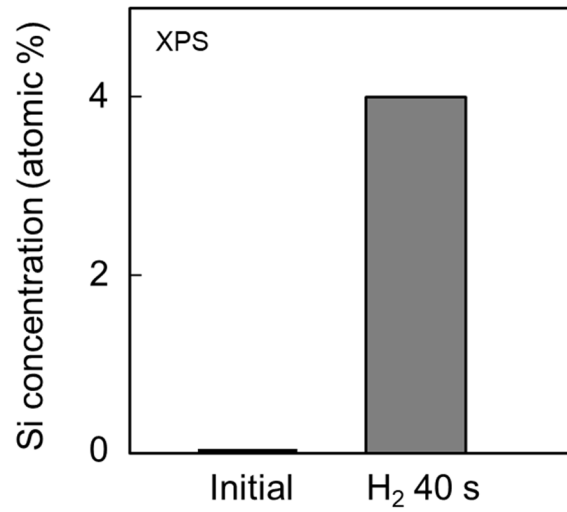


Fig.4-3 Si concentration of the ITO surface without and with H₂ plasma exposure measured by XPS.

4.4 Selective etching of H-modified ITO

To investigate the effects of Ar sputtering in detail, the etch rate of ITO was analyzed by varying the Ar plasma exposure time with constant hydrogen-induced modification. The H₂ plasma exposure time was fixed at 10 s, since a sufficient etch rate increase was expected. Figure 4-4 shows the extent of ITO etching as a function of Ar plasma exposure time at two different V_{pp} values. At a high V_{pp} (960 V), the amount of etched ITO increased with increasing Ar plasma exposure time. During the initial stage of Ar sputtering, the extent of ITO etching was increased markedly by hydrogen-induced ITO modification. After the complete removal of the modified layer surface, the sputtering of the underlying nonmodified ITO becomes dominant. In the case of a low V_{pp} , the extent of ITO etching saturated at 10 nm, which is close to the theoretical hydrogen penetration depth, as shown in Fig. 4-5. We confirmed that the amount of etched ITO can be self-limited by adjusting V_{pp} .

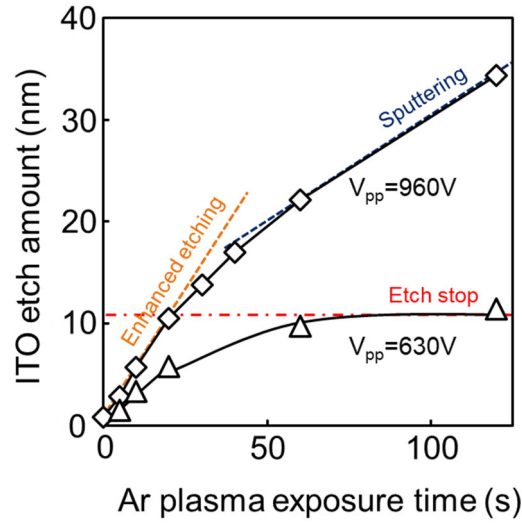


Fig.4-4 Amount of etched ITO as a function of Ar plasma exposure time at different V_{pp} values (H_2 plasma exposure time: 10 s).

Figure 4-5(a) shows a cross-sectional TEM image of ITO after H_2 plasma irradiation, where the modified layer thickness was about 10 nm. Figure 4-5(b) shows the simulated H ion penetration depth into ITO. The etch rate enhancement mechanism is described in detail elsewhere¹⁾. We found that ITO was reduced by hydrogen injection, which generated an In-rich layer (hydrogen-induced damage) on the surface. The modified layer (white area) in the TEM image is the metallic In layer generated by hydrogen injection. Because this In-rich layer had a higher sputtering yield, the hydrogen-damaged layer increased the ITO etch rate. Therefore, these results show that the modified layer thickness was consistent with the theoretical penetration depth of hydrogen. The reason for the selection of H_3^+ ions for simulation is that H_3^+ is the major ion species in H_2 plasma. We confirmed by quadrupole mass spectrometry (QMS) that H_3^+ is the dominant ion species in H_2 plasma in the CCP reactor with a similar configuration³²⁾, and the collision cross section for generating H_3^+ is larger than those in other major reactions³³⁾.

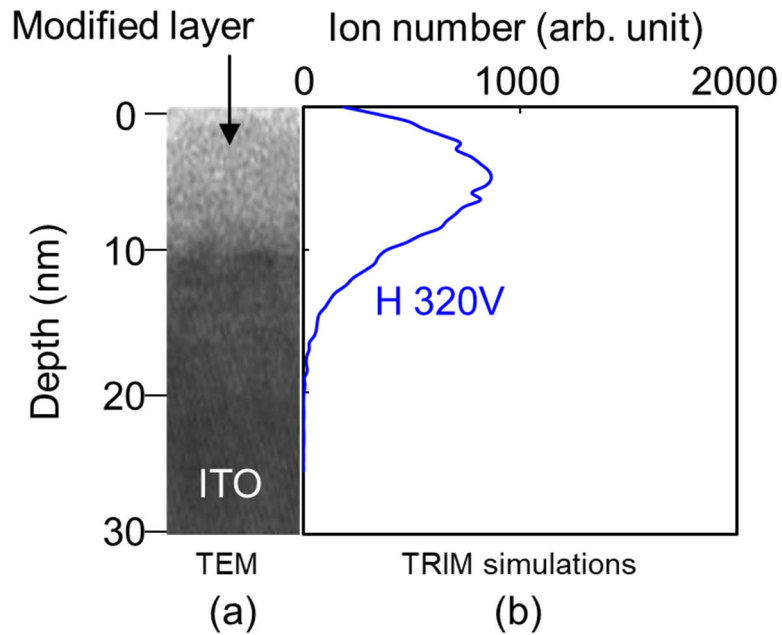


Fig.4-5 H ion penetration depth in ITO: (a) TEM and (b) TRIM simulation.

4.5 Highly selective cyclic etching over mask materials

The selectivity for the etching of ITO over that for the mask material is also indispensable for device fabrication. By precisely controlling the surface adsorption of a protective film on different materials, highly selective etching of ITO can be achieved. Carbon-based and Si-based films are the candidate protective films. Carbon-based films can be deposited using CH_4 -containing plasma. When we use CH_4 plasma for ITO etching, the C-based film can be selectively deposited on SiO_2 (mask material)²⁾. The Si-based film can be deposited using Si-based gas, e.g., SiH_4 , or Si from the chamber components. In this study, we intentionally controlled the amount of Si generated from the upper electrode³¹⁾, and demonstrate the highly selective cyclic etching.

Figure 4-6 shows the dependence of the amounts of etched ITO and SiO₂ on Ar exposure time. The H₂ plasma exposure time was 10 s. The etch rate selectivity for ITO over SiO₂ was infinitely high for shorter Ar exposure times (< 15 s), because Si is selectively deposited on SiO₂ during H₂ plasma exposure. In the case of ITO, the etch rate was increased in the range from 0 to 30 s of Ar plasma exposure. This increase was caused by the metallic In layer (with hydrogen-induced damage), which has a threefold higher sputtering yield than ITO. Both the surface reduction layer formation and selective surface adsorption of Si on SiO₂ resulted in the highly selective etching of ITO over SiO₂.

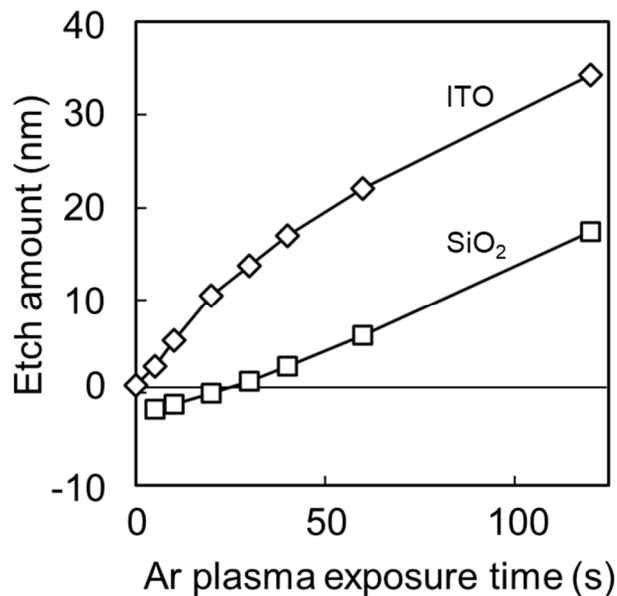


Fig.4-6 Dependence of etched ITO amount on Ar plasma exposure time (H₂ plasma exposure time: 10 s).

Figure 4-7 shows the schematics of Si adsorption on the ITO and SiO₂ surfaces. In the case of SiO₂, Si was deposited on the surface and the SiO₂ etch rate was decreased. On the hydrogen-modified ITO surface, the amount of adsorbed Si is expected to be much less than that on the SiO₂ surface. The reason for the selective adsorption of Si on SiO₂ is speculated to be the

difference between the amounts of oxygen in the ITO and SiO_2 surfaces. The amount of oxygen is smaller in ITO. Thus, volatile OH_x is difficult to generate through the reaction of SiH_x from the top electrode and oxygen from ITO. Because only a negligible amount of Si is deposited on the ITO surface, it hardly has any effect on ITO etching. On the other hand, a larger amount of oxygen exists in SiO_2 . H in SiH_x is removed by its reaction with oxygen in SiO_2 , which results in the generation of volatile OH_x . Therefore, Si is deposited on SiO_2 selectivity.

The result indicates that the selective surface adsorption can realize the highly selective etching of ITO over SiO_2 . For the selective surface adsorption of other materials, a database of time-dependent and ion-energy-dependent surface adsorption coefficient is strongly required for many precursors and other materials.

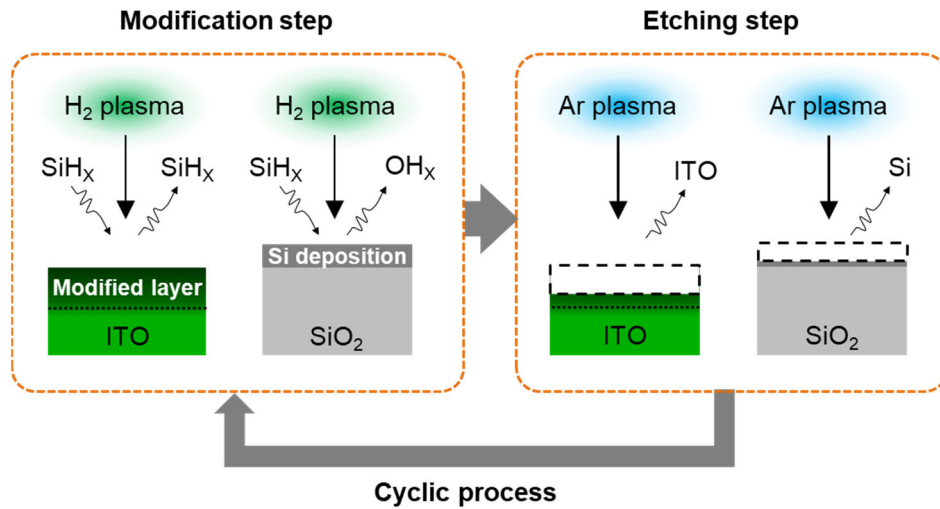


Fig.4-7 Proposed model of Si adsorption differences between ITO and SiO_2 surfaces.

Figure 4-8 shows the cycle number dependence of etched amount (ITO vs SiO_2). The amount of etched ITO was constant at a rate of 3 nm/cycle, while that of SiO_2 was almost zero.

We thus confirmed the sufficient stability of ITO cyclic etching. The amount of etched SiO_2 was a negative value, which means that Si was deposited on the SiO_2 surface, resulting in the infinite selectivity for ITO over SiO_2 . In the first cycle, there is a large amount of oxygen in SiO_2 and Si is deposited on the SiO_2 surface. After the second cycle, there is no oxygen on the surface with Si deposition. As no Si was deposited on the Si of SiO_2 surface in this incident ion energy range, the deposition thickness saturated.

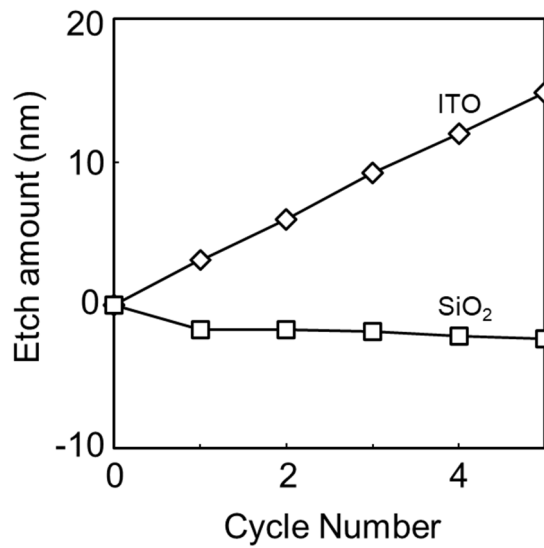


Fig.4-8 Cyclic number dependence of etched amount (ITO vs SiO_2)

(H_2 : 5 s, 960V= Ar : 5 s, 960 V).

4.6 Etched ITO profile

We analyzed the etched ITO profile with the hard-mask SiO_2 (thickness, 70 nm; etch space, 160 nm) by SEM. Figure 4-9(a) shows the ITO profile after H_2/Ar plasma etching, where the ITO space was 190 nm and the hard-mask SiO_2 thickness was 59 nm. This case exhibits the problems of an expanding space and a low selectivity for ITO over SiO_2 . Figure 4-9(b) shows the ITO profile after cyclic H_2 and Ar etching, where the ITO space was 164 nm and the hard-mask

SiO₂ thickness was 70 nm. Space width was measured at the top of ITO. The hard-mask SiO₂ thickness after cyclic etching is almost same as that of the initial sample. We confirmed the highly selective etching for ITO over SiO₂ with the cyclic etching process using the hard-mask to control the Si deposition, resulting in superior profile controllability. One of the major etching concerns of difficult-to-etch materials is residues since the reaction by-products are easily redeposited on the wafer surface. However, the amount of residues on the side wall is negligible, as shown in the SEM image in Fig. 4-9. When the aspect ratio of trench/hole patterns becomes much higher, the side wall residues might be an issue for this process. Thus, further study of residue reduction as well as the post-etching cleaning process (wet/dry) will be required for devices in the near future.

The H₂ and Ar plasma exposure times were both 5 s (Fig. 4-9). When we use a longer H₂ exposure time, Si was released from the chamber parts and deposited on the ITO and SiO₂ surfaces. This causes the fluctuations in ITO etch rate uniformity and repeatability. Thus, the surface reaction control of the chamber wall is indispensable to realizing the cyclic process or atomic/molecular level processes. To obtain highly selectivity for ITO over mask materials, a database of surface adsorption of a precursor on the materials will also be important for the precise control of cyclic, multistep thin-layer etching.

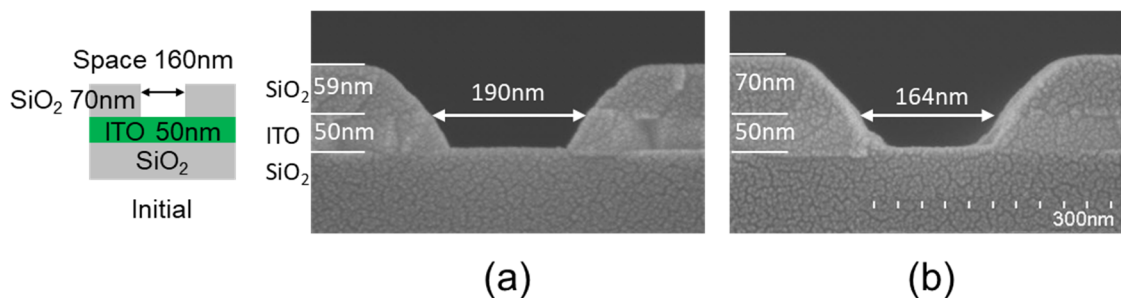


Fig.4-9 Cross-sectional images of etched ITO profile: (a) after H₂/Ar plasma etching and (b) after cyclic etching.

4.7 Conclusions

We investigated the effect of hydrogen-induced modification on ITO etch rate increase and demonstrated the cyclic thin-layer etching of ITO. Hydrogen plasma generates a modified layer on the ITO surface, which has a high etching rate in Ar plasma. The thickness of the modified layer was about 10 nm (V_{pp} 960 V). Only the hydrogen-induced modified layer of ITO can be etched by precisely controlling ion energy; the rate of etching the underlying non modified ITO is almost zero. Thus, the self-limiting etching of ITO was demonstrated. Cyclic etching was investigated using hydrogen plasma, followed by Ar plasma for highly selective etching of ITO/SiO₂. Silicon, which is generated from the top electrode, was deposited on the SiO₂ surface selectively during the cyclic process; the amount of deposited Si on the modified ITO surface was negligible. Therefore, highly selective etching of ITO over SiO₂ (mask material) can be achieved by the selective surface adsorption of a protective film. And it was suggested that cyclic etching by selective surface adsorption of Si can precisely control the etch rates of ITO and SiO₂, resulting in an almost infinite selectivity for ITO over SiO₂ and in improved profile controllability.

4.8 References

- ¹ A. Hirata, M. Fukasawa, T. Shigetoshi, M. Okamoto, K. Nagahata, H. Li, K. Karahashi, S. Hamaguchi, and T. Tatsumi: Jpn. J. Appl. Phys. **56**, 06HD02 (2017).
- ² H. Li, K. Karahashi, M. Fukasawa, K. Nagahata, T. Tatsumi, and S. Hamaguchi: Jpn. J. Appl. Phys. **55**, 021202 (2016).
- ³ K. Karahashi and S. Hamaguchi: Journal of Physics D: Applied Physics **47**, 224008 (2014).
- ⁴ H. Li, K. Karahashi, M. Fukasawa, K. Nagahata, T. Tatsumi, and S. Hamaguchi: J. Vac. Sci. Technol. A **33**, 060606 (2015).
- ⁵ M. Takabatake, Y. Wakui, and N. Konishi: J. Electrochem. Soc. **142**, 2470 (1995).
- ⁶ R. Fang, W. J. Jiang, X. Guo, J. R. Han, and G. D. Shen, in *Proceedings of SPIE; Vol. 7631* (2009), p. 76310S.

CHAPTER 4

- 7 K. Ishikawa, K. Karahashi, T. Ichiki, J. P. Chang, S. M. George, W. M. M. Kessels, H. J. Lee, S. Tinck, J. H. Um, and K. Kinoshita: *Jpn. J. Appl. Phys.* **56**, 06HA02 (2017).
- 8 N. Miyoshi, H. Kobayashi, K. Shinoda, M. Kurihara, T. Watanabe, Y. Kouzuma, K. Yokogawa, S. Sakai, and M. Izawa: *Jpn. J. Appl. Phys.* **56**, 06HB01 (2017).
- 9 Y. Ishii, K. Okuma, T. Saldana, K. Maeda, N. Negishi, and J. Manos: *Jpn. J. Appl. Phys.* **56**, 06HB07 (2017).
- 10 T. Kim, J. K.-C. Chen, and J. P. Chang: *J. Vac. Sci. Technol. A* **32**, 041305 (2014).
- 11 T. Kim, Y. Kim, J. K.-C. Chen, and J. P. Chang: *J. Vac. Sci. Technol. A* **33**, 021308 (2015).
- 12 T. Sasaki, K. Matsuda, M. Omura, I. Sakai, and H. Hayashi: *Jpn. J. Appl. Phys.* **54**, 06GB03 (2015).
- 13 N. R. Johnson, H. Sun, K. Sharma, and S. M. George: *J. Vac. Sci. Technol. A* **34**, 050603 (2016).
- 14 N. D. Altieri, J. K.-C. Chen, L. Minardi, and J. P. Chang: *J. Vac. Sci. Technol. A* **35**, 05C203 (2017).
- 15 T. Meziani, P. Colpo, V. Lambertini, G. Ceccone, and F. Rossi: *Applied Surface Science* **252**, 3861 (2006).
- 16 I. Adesida, D. G. Balleger, J. W. Seo, A. Ketterson, H. Chang, and K. Y. Cheng: *J. Vac. Sci. Technol. B* **9**, 3551 (1991).
- 17 R. J. Saia, R. F. Kwasnick, and C. Y. Wei: *J. Electrochem. Soc.* **138**, 493 (1991).
- 18 J. W. Lee, B. Pathangey, M. R. Davidson, P. H. Holloway, E. S. Lambers, B. Davydov, T. J. Anderson, and S. J. Pearton: *J. Vac. Sci. Technol. A* **16**, 2177 (1998).
- 19 Y. J. Lee, J. W. Bae, H. R. Han, J. S. Kim, and G. Y. Yeom: *Thin Solid Films* **383**, 281 (2001).
- 20 T. Y. Lee, I. H. Lee, and C. W. Chung: *Thin Solid Films* **547**, 146 (2013).
- 21 J. H. Jeong, T. Endoh, Y. Kim, W. K. Kim, and S. O. Park: *J. Appl. Phys.* **115**, 17C727 (2014).
- 22 S. D. Sherpa and A. Ranjan: *J. Vac. Sci. Technol. A* **35**, 01A102 (2017).
- 23 S. A. Vitale and S. Berry: *J. Vac. Sci. Technol. B* **31**, 021210 (2013).
- 24 T. L. Breen, P. M. Fryer, R. W. Nunes, and M. E. Rothwell: *Langmuir* **18**, 194 (2002).
- 25 C. J. Huang, Y. K. Su, and S. L. Wu: *Materials Chemistry and Physics* **84**, 146 (2004).
- 26 M. Mohri, H. Kakinuma, M. Sakamoto, and H. Sawai: *Jpn. J. Appl. Phys.* **29**, L1932 (1990).
- 27 H. B. Andagana and X. A. Cao: *J. Vac. Sci. Technol. A* **28**, 189 (2010).
- 28 J. F. Z. [<http://www.srim.org>].
- 29 H. Li, K. Karahashi, P. Friederich, K. Fink, M. Fukasawa, A. Hirata, K. Nagahata, T. Tatsumi, W. Wenzel, and S. Hamaguchi: *Journal of Vacuum Science & Technology A*:

CHAPTER 4

- Vacuum, Surfaces, and Films **35**, 05c303 (2017).
- ³⁰ H. Li, K. Karahashi, P. Friederich, K. Fink, M. Fukasawa, A. Hirata, K. Nagahata, T. Tatsumi, W. Wenzel, and S. Hamaguchi: Japanese Journal of Applied Physics **57**, 06jc05 (2018).
- ³¹ Y. Zhang, K. Narishige, T. Katsunuma, M. Honda, and K. Yatsuda: Proc. SPIE **8328**, 83280N (2012).
- ³² M. Fukasawa, T. Tatsumi, K. Oshima, K. Nagahata, S. Uchida, S. Takashima, M. Hori, and Y. Kamide: J. Vac. Sci. Technol. A **26**, 870 (2008).
- ³³ T. Tabata and T. Shirai: Atomic Data and Nuclear Data Tables **76**, 1 (2000).

CHAPTER 5

Damage recovery and low-damage ITO etching

5.1 Introduction

The most widely used transparent conductive oxide for optoelectronic devices is tin-doped indium oxide (ITO). Since high-definition micro-OLED (organic light-emitting diode) display needs to maximize the pixel area, the interpixel area must be minimized. The required space width is less than several hundred nanometers. Thus, the fine ITO patterning is strongly required for small display devices (ie, camera viewfinder, head-mounted display). Highly bendable transparent electrodes for a flexible electronic device are also reported to require the ITO mesh patterning, whose line widths are several microns ¹⁾. In future display devices, microfabrication will become increasingly important. As electronic device sizes continue to be scaled down, it is necessary to have a way of achieving anisotropic etching of ITO. Thus, dry etching of ITO is set to become indispensable for micro- and nanopatterning, replacing conventional wet etching. Hydrogen containing plasmas have been reported to etch ITO film. Different gas mixtures were used to etch the ITO layers including H₂ ²⁾, CH₄/H₂ ^{3) 4) 5)}, CH₄/H₂/Ar ⁶⁾, CH₄/Ar ⁷⁾, CH₃OH ⁸⁾, HBr ⁹⁾, and HCl/CH₄ ¹⁰⁾. Surface reaction with hydrogen and/or CH_x species were also studied in detail ^{11) 12)}. However, the mechanism of etching by hydrogen-containing plasma still needs to be understood. We have previously proposed ITO etching using H₂/Ar plasma ^{13) 14)}. For highly selective etching over a dielectric hard mask, CH₄/H₂/Ar plasma was also proposed by some researchers ^{6) 15) 16) 17)}. Incident hydrogen from H₂ or CH₄-based plasmas reduces the ITO surface, resulting in a metallic-In surface. As the sputtering yield of In is much higher than that of ITO, a high etch rate can be achieved. During H₂/Ar plasma etching both the surface reduction and sputtering of metallic-In occurs simultaneously on the ITO surface. Reduction means the metallic-ITO generation. As the complete removal of reduced ITO is difficult, the metallic-In (damaged) layer remained after the etching process. As the residual metallic-In causes degradation of device performances (eg, because of surface leakage), low-damage etching or damage recovery processes are urgently required. To solve these issues, we

investigated the potential of both damage recovery and low-damage etching process that uses simultaneous injection of hydrogen and oxygen.

5.2 Experimental conditions

A SiO₂ (70-100 nm)/ITO (50 nm)/SiO₂/Si sample with a line and space photoresist pattern was used for the experiments. A 50 nm thick layer of ITO was deposited by a sputtering process on a SiO₂/Si substrate, namely a wafer with a diameter of 200 mm. With the overlaying SiO₂ acting as a hard mask, the underlying ITO was etched by CH₄/H₂/Ar, H₂/CO, and H₂/CO/Ar plasmas. For the ITO surface damage and recovery analysis, blanket ITO (50 nm)/SiO₂/Si sample was also used. We used H₂, O₂, and H₂/CO plasmas for the damage generation and recovery investigation. First, the H₂ plasma caused damage to the ITO surface. Subsequently, a recovery process was performed using either O₂ or H₂/CO plasma. The V_{pp} was fixed at 960 V. The pressure and temperature were fixed at 10 mTorr and 80°C, respectively. The etch rate of ITO was measured after application of the H₂, O₂, and H₂/CO plasmas. The process time was 30 s. ITO modified layer was studied via transmission electron microscopy (TEM) and energy dispersive X-Ray (EDX) analysis. The secondary ion mass spectrometry (SIMS) depth profile of the ITO wafers was analyzed using 1 keV Cs⁺ primary ions to detect any modifications to the ITO. The variation of the hydrogen concentration in the SIMS measurement was calibrated using the absolute value measured by elastic recoil detection analysis. The sheet resistance was measured using the four-point probe technique at 49 different locations on each film and an average of the measured values was compared.

5.3 Origin of the ITO roughness after CH₄/H₂/Ar plasma etching

Figure 5-1 shows the SEM image of the ITO profile etched by using CH₄/H₂/Ar plasma with the hard SiO₂ mask; it can be seen that the plasma caused the sidewalls of the ITO features to be rough. We propose that H_x⁺ or CH_x⁺ in the CH₄/H₂/Ar plasma may be the cause of the ITO sidewall roughness. We focused on the effect of hydrogen on modifying the ITO. To investigate the details of the plasma-induced roughness, we analyzed the surface after H₂/Ar plasma exposure (partial etching) via TEM. Halfsphere shaped surface features were observed in Figure 5-2(a). We analyzed the chemical composition of the feature shown in Figure 5-2(a) using EDX (Figure 5-3). We found that the ITO surface was reduced by the H₂/Ar plasma and a metallic-In surface was generated. And the half-sphereshaped surface feature shown in Figure 5-2(a) is thus an agglomeration of In. The In-aggregated part became thick and the nonaggregated part became thin, as shown in Figure 5-2(b). We thus speculate that the ITO sidewall roughness in Figure 5-1 was caused by the agglomeration of metallic-In in ITO. As metallic-In causes fluctuations in the ITO's resistivity, the suppression of such damages (caused by reduction) of ITO is very important.

The blanket ITO film was reduced to a significant depth by the hydrogen plasma. However, the incident angle of the hydrogen on the blanket film and the sidewall of the ITO pattern was completely different. Thus, we need to understand the dependence of the reduction on the angle of the hydrogen incident on the ITO surface. Damage formation on Si surfaces by energetic hydrogen ions has been examined for different angles of incidence with the use of a multibeam system by Ito et al¹⁸⁾. They reported that the depth of a defect layer formed by H⁺ ion irradiation has little dependence on the angle of incidence. As hydrogen atoms are much lighter than Si atoms, energetic hydrogen atoms experience large angle scattering when they collide with substrate Si atoms. We assumed that the scattering of hydrogen also occurred in the case of the ITO sidewalls because the mass numbers of the elements in ITO are much higher than for hydrogen. As the hydrogen ions accelerated in the sheath region have a small angle distribution,

they collided with the ITO sidewall. Regardless of their angles of incidence, hydrogen atoms propagate in nearly all directions in the substrate, which makes the thickness of the reduced-ITO layer less dependent on the hydrogen incident angle. Thus, we conclude that the ITO sidewall was reduced by hydrogen ion injection.

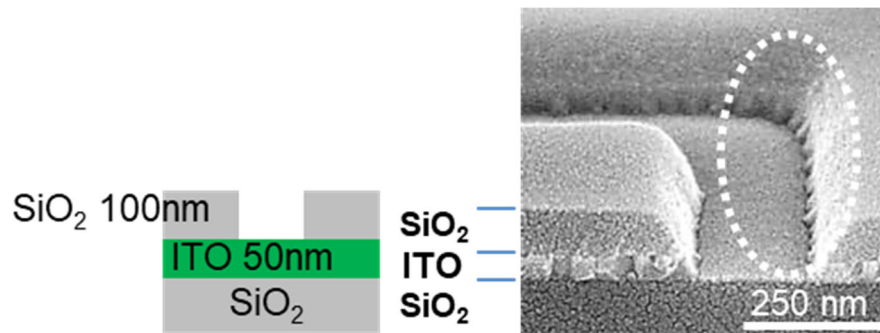


Fig. 5-1 SEM image of ITO etched profile after $\text{CH}_4/\text{H}_2/\text{Ar}$ plasma etching.

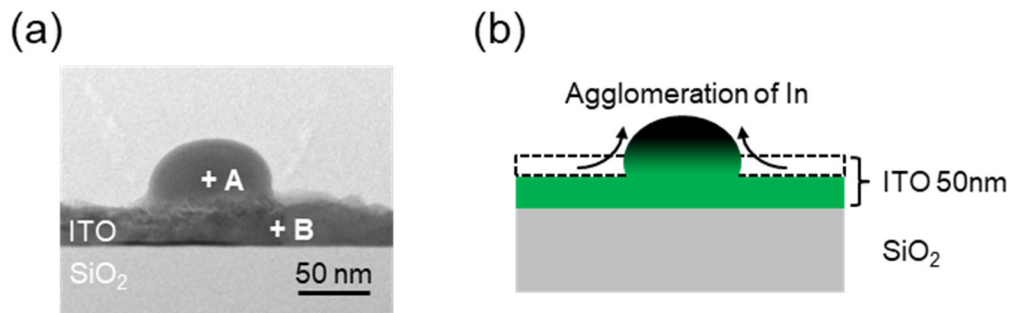


Fig. 5-2 (a)TEM image of ITO film after H_2 plasma etching, and (b)Schematic model.

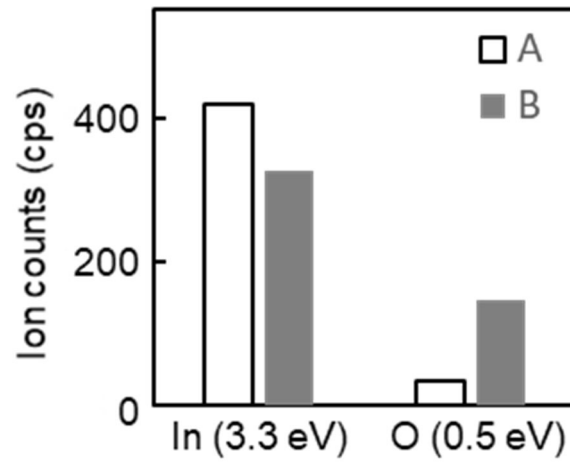


Fig. 5-3 EDX point analysis at points A and B of Figure 5-2(a).

5.4 Analysis of ITO damages

We defined the ITO damage as a reduction of the ITO. As H_x^+ in H_2/Ar plasma can penetrate deep into the ITO, we analyzed the depth profiles of H (Figure 5-4). As the exposure time increased, the hydrogen penetration depth increased. The dominant ion species in H_2/Ar plasma is known to be H_3^+ and the penetration depth of H_3^+ is less than 20 nm, as estimated by the SRIM simulations^{19) 13) 14)}. The V_{pp} of the bottom electrode during H_2/Ar plasma exposure was about 960 V. The IED is well-known to be affected by the RF modulation of the sheath voltage and sheath thickness. Our simulation clarified that the high energy peak of H_3^+ in IED is almost the same as the V_{pp} . Thus, the H_3^+ ion was exposed to the substrate at about 960 eV. The measured depth of the hydrogen and oxygen penetration was slightly greater than in the simulation. We speculate that a knock-on effect of various species during the SIMS analysis may be the cause of the deeper penetration of hydrogen and oxygen compared with what was expected based on the simulations. Figure 5-5 shows the oxygen depth profiles of the same samples. We found that the depth of the reduced ITO was almost the same as the H_x^+ penetration depth.

Penetrated hydrogen reacted with the oxygen in the ITO and generated volatile OH_x as a reaction by-product. Thus, O was removed from the bulk of ITO.

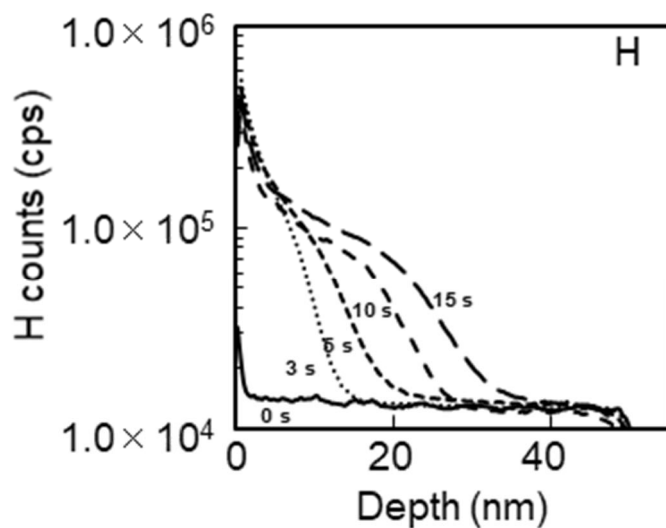


Fig. 5-4 H mass spectrometry SIMS results for an ITO after H_2 plasma etching

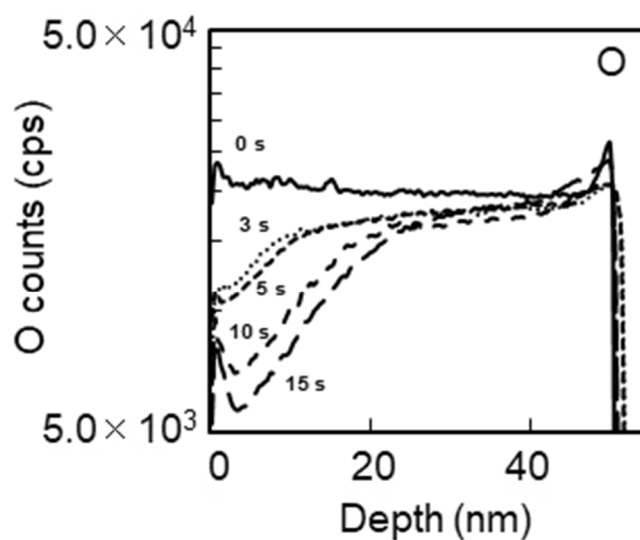


Fig. 5-5 O mass spectrometry SIMS results for an ITO after H_2 plasma etching

5.5 Recovery of reduced ITO

We investigated the possibility of using plasma to aid the recovery of the reduced ITO by using O-containing plasma as O_2 plasma has been shown to recover reduced ITO surfaces. However, when we used this method, excessive oxidation of the ITO surface was observed. Because the penetration depths of oxygen species from the plasma are less than 10 nm, the recovery of any bulk modifications would be difficult. Thus, a damage recovery process that can recover bulk ITO is urgently required. Ito et al studied enhanced oxygen diffusion in Si substrates²⁰⁾. It was found that oxidation of a Si surface exposed to oxygen radicals is significantly enhanced only if the surface is simultaneously subjected to both an oxygen radical supply and energetic hydrogen ion bombardment. A possible mechanism of the enhanced oxygen diffusion assisted by hydrogen ion injections is momentum transfer from incident H^+ ions to O atoms incorporated in the Si substrate. Each impact of a fast hydrogen ion or atom against an oxygen atom may transfer only a small amount of the momentum of the hydrogen species to the oxygen atom, but a series of such collisions may transport the oxygen atom a long distance into the Si layer. If Ar^+ was used instead of H^+ , the momentum transfer from incident Ar^+ ions to O atoms is also expected. However, the penetration depth of Ar^+ (<10 nm), accelerated by almost the same incident energy, is much shallower than that of H^+ . As a result, the penetration depth of the oxygen atom becomes shallow (<10 nm). The recovery of bulk ITO (>10nm) is difficult in the case of O_2/Ar plasma. Only excess surface oxidation is expected. He/O_2 plasma is possible to recover bulk ITO damages since the penetration depths of He^+ is much deeper than that of Ar^+ . This means that the light mass ions (H_x^+ , He^+) are indispensable to realize damage recovery of bulk ITO. In H_2/CO plasma, H_x , C_x , CH_x , O_x , OH_x , CO_x , H_xCO , H_xCOH species were reported to be generated²¹⁾. In these incident species, light mass ions are only H_x^+ . The penetration depths of heavier ions, whose mass number is more than 12 (carbon), become shallower than 10 nm. Thus, only the H_x^+ ions are possible to recover bulk damages of ITO.

Momentum transfer from the H^+ ions to the atoms in the ITO substrate is also expected to occur. Thus, we simultaneously used hydrogen and oxygen for the ITO damage recovery plasma treatment. Figure 5-6 shows the depth profile of oxygen in untreated ITO (initial) and that after H_2/CO plasma exposure. The untreated ITO had larger oxygen counts in the depth of 1 to 2 nm from the surface, due to atmospheric oxidation. We could not directly use H_2/O_2 plasma owing to safety risks in the mass-produced equipment. We found that the bulk reduction of ITO (>10 nm) was almost completely recovered by the simultaneous injection of both hydrogen and oxygen, without excess oxidation occurring at the ITO surface (<10 nm). We observed the slightly reduced ITO on the outermost surface in the depth within 0 to 5 nm. The incorporated hydrogen generated OH_x and removed the outermost surface oxygen as reaction by-products. We assumed that the carbon in CO had little impact on damages because C and O easily react to form highly volatile CO_2 . If the carbon is incorporated into the ITO, the resistivity could be varied. However, the resistivity is almost the same as the untreated ITO (initial) after H_2/CO plasma exposure, as shown in Figure 5-7. This means that the effect of carbon incorporation is a negligible level. The thin, reduced outermost surface layer was eliminated by wet treatment, resulting in the almost complete recovery of the reduced ITO back to ITO. For device applications, the ITO's resistivity is a good indicator of damage. Thus, we compared the resistivity before and after the H_2/CO plasma recovery process (Figure 5-7). Initially, we found that the resistivity increased after O_2 or H_2 plasma exposure. The O_2 plasma caused excess oxidation, resulting in a resistivity increase. After H_2 plasma exposure, the oxide was removed from the ITO film via the generation of OH_x . We propose that oxygen vacancies caused the resistivity increase. After that H_2 plasma exposure, we then investigated the H_2/CO plasma recovery process. We found that the H_2/CO plasma was able to recover the reduced ITO surfaces. We propose that the momentum transfer from incident H^+ ions to O atoms incorporated in the ITO caused enhanced diffusion of O into the bulk regions of the ITO. We also studied the simultaneous injection of oxygen and hydrogen by using only H_2/CO plasma. When using only H_2/CO plasma, the final resistivity was close to that of the initial sample.

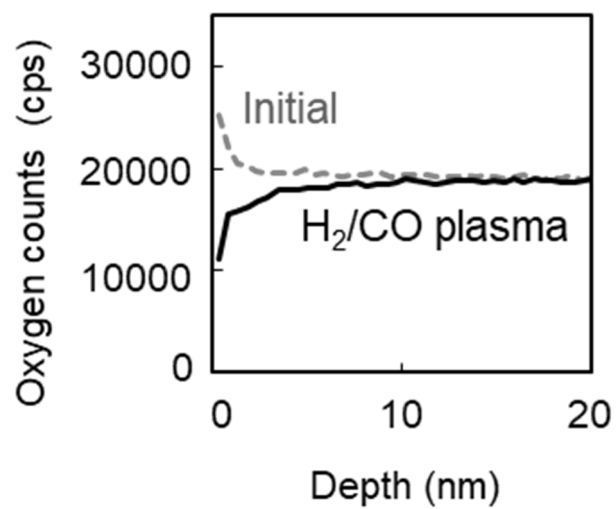


Fig. 5-6 Depth profiles of oxygen with and without H₂/CO plasma exposure by SIMS.

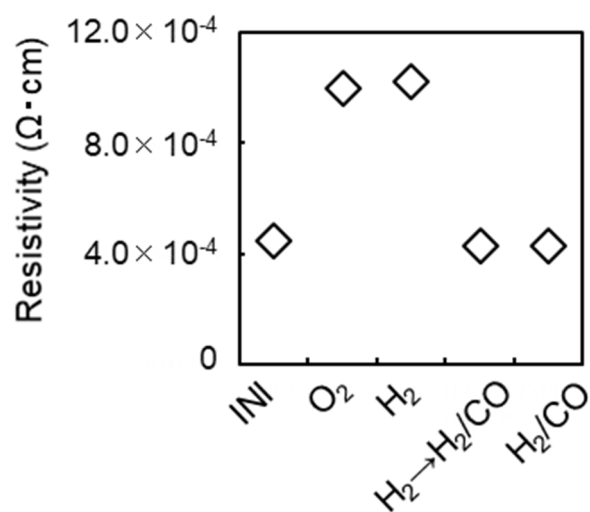


Fig. 5-7 Resistivity of ITO after O₂, H₂, and H₂/CO plasma.

5.6 Possibility of ITO etching with H₂/CO plasma

The process sequence of the damage recovery experiment was initially an H₂/Ar or CH₄/H₂/Ar etching step, followed by the recovery process using H₂/CO plasma. From the view of mass production, it is important to minimize the number of process steps. Thus, we investigated the possibility of etching with H₂/CO plasma, thus creating a low damage one-step etching process. Figure 5-8 shows the ITO etch rate after applying O₂, H₂, and H₂/CO plasma. The etch rate of ITO in the H₂ plasma was 7.8 nm/min, while in the H₂/CO plasma it was about 15.2 nm/min. The etch rate of the ITO was thus increased by the mixture of hydrogen and oxygen plasma.

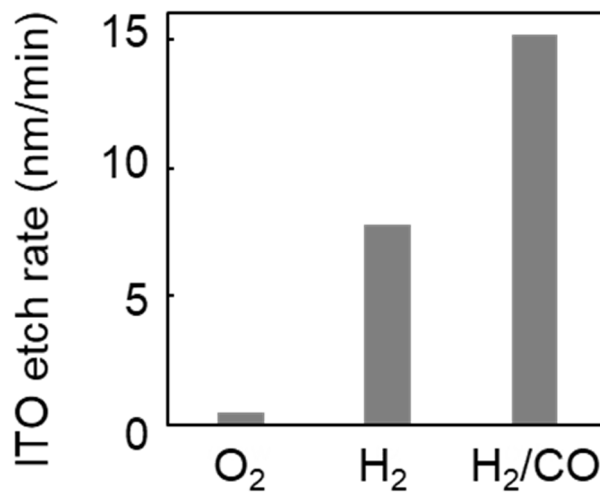


Fig. 5-8 ITO etch rate after application of O₂, H₂, and H₂/CO plasma.

In the case of bulk ITO, the film quality was almost entirely maintained owing to the enhanced diffusion of oxygen. However, the surface of the ITO was reduced by the generation of volatile OH_x. As indium is reported to have a higher Ar sputtering yield (3.1 atoms/ion) than ITO (0.9 atoms/ion)²⁾, we propose that the etch rate was increased by the sputtering kinetics at the

reduced ITO. The ITO sputter rates strongly depend on the mass number of incident ions¹²⁾. Basically, the heavier the mass number, the higher the sputter rate of ITO. In the CO-based plasma, CO^+ and CO_2^+ ions are well-known to be generated. The masses of CO^+ and CO_2^+ are 28 and 44. The sufficient physical sputter reaction is expected in the CO-based plasma since the mass number of dominant ion species are relatively close to that of Ar^+ ($m/e = 40$). Thus, the CO^+ and CO_2^+ could transfer momentum energy to the surface for sputtering reaction, instead of conventional Ar^+ . Another possibility is that an increase in the number of grain boundaries occurred after hydrogen injection. To investigate only the physical effect, we exposed the ITO surface to He^+ instead of hydrogen. Figure 5-9 shows top view TEM images of pristine ITO and ITO after He^+ exposure. The He ion injection generated a polycrystalline ITO surface, which means that the number of grain boundaries increased. Because the chemical bonding energies of the grain boundaries are speculated to be lower than that in the bulk of ITO, the sputtering yield of the polycrystalline ITO was enhanced. In the case of ZnO, which is one of the transparent conductive oxides, we also confirmed that the number of grain boundary was increased by He^+ injection by our beam experiment²²⁾. When the ZnO sample was exposed to a He^+ beam before the exposure to Ne^+ , the physical sputtering yield of ZnO by Ne^+ increases significantly after it is exposed to energetic He^+ ions. In the case of ITO, we speculate that it is also possible to increase the sputtering yield by Ar plasma after He plasma exposure. Although the dominant contribution of etch rate enhancement is caused by metallic-ITO generation by the reduction of ITO, the grain boundary increase could have some influence on the ITO etch rate enhancement. We concluded that the increase of the ITO sputter rate was caused by both generations of metallic-ITO via the reduction of ITO and an increase in the number of grain boundaries (Figure 5-10).

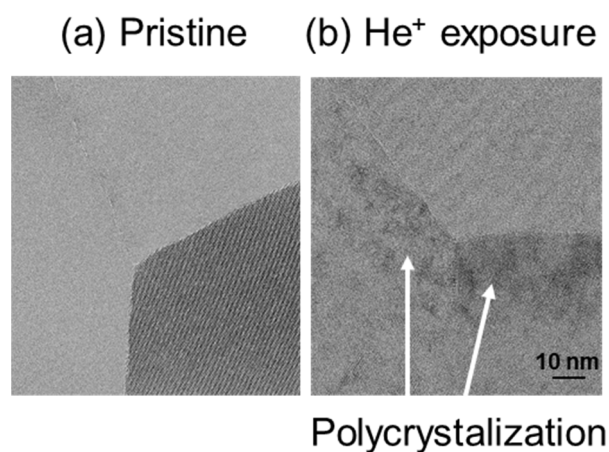


Fig. 5-9 Top view TEM image of (a) pristine ITO and (b) ITO after He⁺ exposure

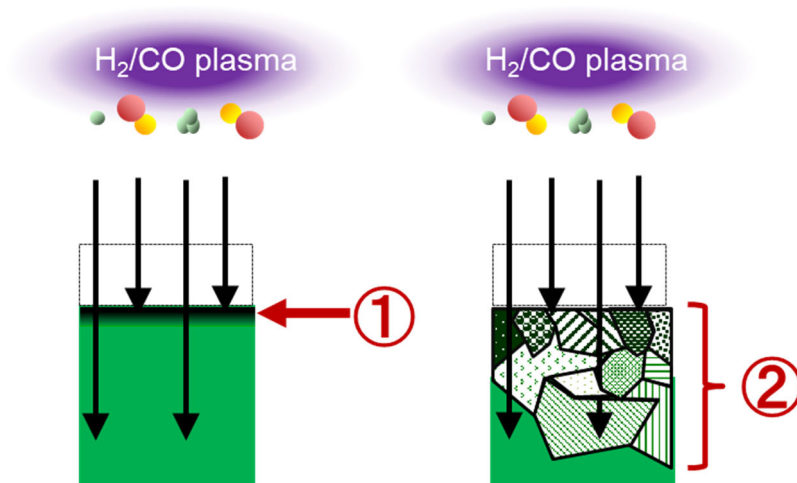


Fig. 5-10 Proposed model of ITO etching after H₂/CO plasma exposure.

Patterned samples were also etched by using the H₂/CO plasma. The cross-sectional SEM image in Figure 11A clearly shows that the ITO is etched by the H₂/CO plasma. However, some residue remained on the underlying SiO₂. To increase the effect of the physical sputtering, we also tested H₂/CO/Ar plasma as a low damage ITO etching process. The ITO was etched by

the $\text{H}_2/\text{CO}/\text{Ar}$ plasma without any residue remaining and without any sidewall roughness (Figure 11B). The addition of Ar eliminates the residues on the underlayer, due to the increase of physical sputtering effect. Since the plasma density was increased by the addition of Ar, the number of H_x^+ ions could be increased due to the dissociation degree enhancement. However, the sufficient amount of oxygen was also generated in the $\text{H}_2/\text{CO}/\text{Ar}$ plasma, ITO damage due to H injection is speculated to be recovered. A further quantitative study of H and O amount in the plasma is strongly required in the near future. Reduction and excess oxidation of ITO surfaces after etching is an issue for device manufacturing. However, simultaneous injection of hydrogen and oxygen can minimize the damage. Thus, mixed hydrogen and oxygen gas chemistry is a potential candidate for achieving low damage ITO etching as well as for achieving a damage recovery process after etching with hydrogen-containing plasma (H_2/Ar or $\text{CH}_4/\text{H}_2/\text{Ar}$).

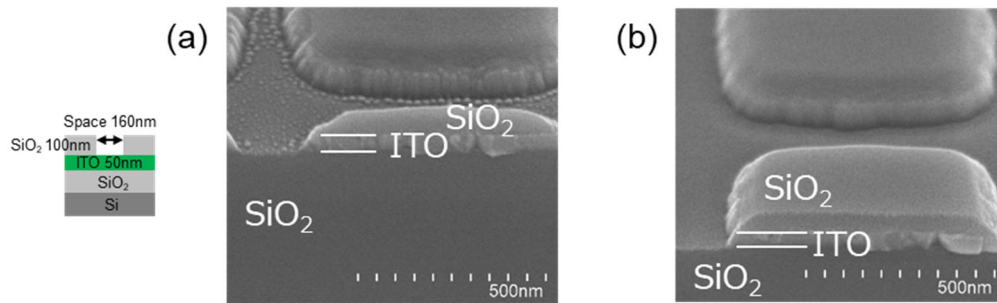


Fig. 5-11 Cross-sectional SEM image after (a) H_2/CO and (b) $\text{H}_2/\text{CO}/\text{Ar}$ plasma etching of ITO.

5.7 Conclusions

H_2 plasma required for ITO etching reduced the ITO surface and damaged it in the form of generating metallic-In. To investigate the damage recovery, in Chapter 5, potential of O_2 plasma

and the potential of using H_2/CO plasma as a low-damage etching technique was studied. Damage recovery for device fabrication was possible using H_2/CO plasma, O_2 plasma caused excess oxidation of the ITO surface. When using H_2/CO plasma, the final resistivity was close to that of the initial sample. Simultaneous injection of hydrogen and oxygen recovered the reduced ITO to its initial state. The etch rate of the ITO was thus increased by the mixture of hydrogen and oxygen plasma compared with O_2 single gas and H_2 single gas. The He ion injection generated a polycrystalline ITO surface, the number of grain boundaries increased. We concluded that the increase of the ITO sputter rate was caused by both generations of metallic-ITO via the reduction of ITO and an increase in the number of grain boundaries. Patterned samples were etched by the $\text{H}_2/\text{CO}/\text{Ar}$ plasma without any residue remaining and without any sidewall roughness. The addition of Ar eliminates the residues on the underlayer, due to the increase of physical sputtering effect. With hydrogen and oxygen-mixed plasma, we were able to achieve low-damage etching by controlling the balance between surface reduction and oxidation.

5.8 References

- ¹ K. Sakamoto, H. Kuwae, N. Kobayashi, A. Nobori, S. Shoji, and J. Mizuno: Sci Rep **8**, 2825 (2018).
- ² T. Minami, T. Miyata, A. Iwamoto, S. Takata, and H. Nanto: Jpn. J. Appl. Phys. **27**, L1753 (1988).
- ³ M. Mohri, H. Kakinuma, M. Sakamoto, and H. Sawai: Jpn. J. Appl. Phys. **29**, L1932 (1990).
- ⁴ I. Adesida, D. G. Ballegeer, J. W. Seo, A. Ketterson, H. Chang, and K. Y. Cheng: J. Vac. Sci. Technol. B **9**, 3551 (1991).
- ⁵ K. Nakamura, T. Imura, H. Sugai, M. Ohkubo, and K. Ichihara: Jpn. J. Appl. Phys. **33**, 4438 (1994).
- ⁶ D. Y. Kim, J. H. Ko, M. S. Park, and N.-E. Lee: Thin Solid Films **516**, 3512 (2008).
- ⁷ Y. J. Lee, J. W. Bae, H. R. Han, J. S. Kim, and G. Y. Yeom: Thin Solid Films **383**, 281 (2001).

CHAPTER 5

- 8 H. Sakaue, M. Koto, and Y. Horiike: Jpn. J. Appl. Phys. **31**, 2006 (1992).
- 9 L. Y. Tsou: J. Electrochem. Soc. **140**, 2965 (1993).
- 10 Y. Kuo: Jpn. J. Appl. Phys. **36**, L629 (1997).
- 11 S. Major, S. Kumar, M. Bhatnagar, and K. L. Chopra: Appl. Phys. Lett. **49**, 394 (1986).
- 12 H. Li, K. Karahashi, M. Fukasawa, K. Nagahata, T. Tatsumi, and S. Hamaguchi: J. Vac. Sci. Technol. A **33**, 060606 (2015).
- 13 A. Hirata, M. Fukasawa, T. Shigetoshi, M. Okamoto, K. Nagahata, H. Li, K. Karahashi, S. Hamaguchi, and T. Tatsumi: Jpn. J. Appl. Phys. **56**, 06HD02 (2017).
- 14 A. Hirata, M. Fukasawa, K. Nagahata, H. Li, K. Karahashi, S. Hamaguchi, and T. Tatsumi: Jpn. J. Appl. Phys. **57**, 06JB02 (2018).
- 15 T. Meziani, P. Colpo, V. Lambertini, G. Ceccone, and F. Rossi: Applied Surface Science **252**, 3861 (2006).
- 16 R. J. Saia, R. F. Kwasnick, and C. Y. Wei: J. Electrochem. Soc. **138**, 493 (1991).
- 17 J. W. Lee, B. Pathangey, M. R. Davidson, P. H. Holloway, E. S. Lambers, B. Davydov, T. J. Anderson, and S. J. Pearton: J. Vac. Sci. Technol. A **16**, 2177 (1998).
- 18 T. Ito, K. Karahashi, K. Mizotani, M. Isobe, S.-Y. Kang, M. Honda, and S. Hamaguchi: Jpn. J. Appl. Phys. **51**, 08HB01 (2012).
- 19 J. F. Z. [<http://www.srim.org>].
- 20 T. Ito, K. Karahashi, M. Fukasawa, T. Tatsumi, and S. Hamaguchi: Japanese Journal of Applied Physics **50**, 08kd02 (2011).
- 21 Y. Muranaka, H. Yamashita, K. Sato, and H. Miyadera: J. Appl. Phys. **67**, 6247 (1990).
- 22 K. Karahashi, T. Ito, H. Li, M. Isobe, K. Mizotani, S. Shigeno, M. Fukasawa, A. Hirata, T. Tatsumi, and S. Hamaguchi: Effects of light ion beam irradiation in plasma etching processes. Long Beach, CA, 2018.

CHAPTER 6

Surface reaction mechanism of SiN ALE

6.1 Introduction

The size of semiconductor devices is continuously being scaled down, and there is a demand for the precise control of the etched profiles and a minimization of damage during dry etching. ALE is a promising technology that is able to overcome these issues. We focus on ALE for dielectric films, which consists of two sequential steps: the surface adsorption of a polymer and desorption steps. SiN is widely used in device structures, such as in the sidewall of transistor gates and the liner-layer at the contact bottom. However, the number of published papers related to SiN ALE is much lower than that related to SiO₂ ALE. Thus, we investigated the SiN ALE in detail. There are two main proposed methods of SiN ALE. The first consists of two steps: modified layer generation by H₂ plasma and then removal of the modified layer ^{1) 2) 3)}. However, H_x⁺ ions penetrate deep into the surface even at a low energy. Thus, the H_x⁺ ions may cause damage to the underlying layer in device fabrication. The other is a method in which a hydrofluorocarbon (HFC) polymer is adsorbed by CH₃F/Ar plasma and the reactive layer is desorbed by Ar plasma ^{4) 5) 6)}. We focus on the latter method since less damage is expected.

To date, most of the reports on SiN ALE have focused on the mechanism, and few reports have been published that discuss the issues encountered in device fabrication. However, when ALE is used for device manufacturing, process stability and suppression of fluctuation, which depend on the chamber conditions, are extremely important ^{7) 8)}. Therefore, we investigate SiN ALE stability with process optimization of the surface adsorption and desorption steps, and we clarify the rate fluctuation mechanism.

6.2 Experimental conditions

CCP reactor was used in this study. SiN (50 nm) was deposited on the Si substrate by low pressure chemical vapor deposition. One etching cycle consisted of two steps. CH₃F/Ar plasma was applied to deposit the HFC polymer as the adsorption step. The bias power was 0W. The gas flow rates of CH₃F and Ar were 40 and 460 SCCM, respectively. Then, Ar plasma was used in the desorption step. The V_{pp} of the bottom electrode was 330 V in the desorption. The high energy peak of simulated ion energy distribution function for the Ar desorption step was nearly equal to the V_{pp} . By repeating this sequence, SiN ALE was achieved (Fig. 6-1). The conditions for each experiment are shown in Tables 6-1.

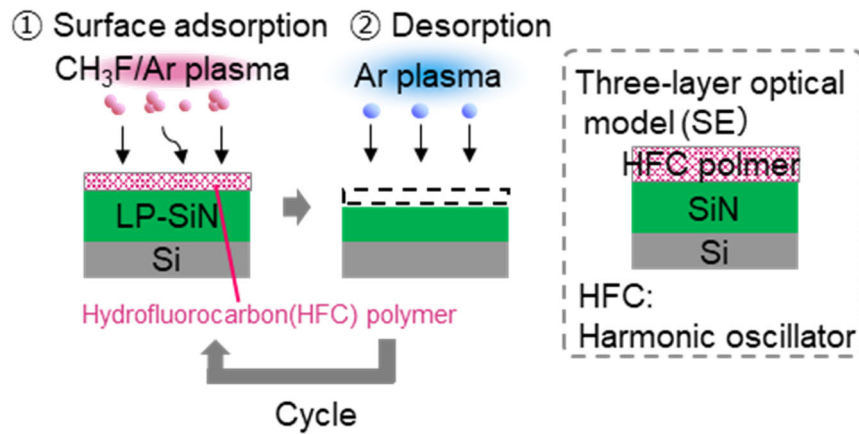


Fig. 6-1 Schematic of SiN ALE sequence and optical model for spectroscopic ellipsometry.

CHAPTER 6

Table 6-1 Experiment.

<i>Experiment</i>	Adsorption				Transition	Desorption				O ₂ ashing				Cycle number
	Pressure (mTorr)	Gas flow rate (sccm)	Ion energy (eV)	Time (s)	Time (s)	Pressure (mTorr)	Gas flow rate (sccm)	Ion energy (eV)	Time (s)	Pressure (mTorr)	Gas flow rate (sccm)	Ion energy (eV)	Time (s)	
(a) Adsorption	40	CH ₃ F/Ar = 40/460	~ 25	4, 8, 12										1
(b) Adsorption	40	CH ₃ F/Ar = 15/485	~ 25	4, 8, 12										1
(c) ALE	40	CH ₃ F/Ar = 15/485	~ 25	4	20	40	Ar = 500	330	10					1,2,3, 5,10
(d) ALE w/ O ₂ desorption	40	CH ₃ F/Ar = 15/485	~ 25	4	20	40	O ₂ /Ar = 50/450	300	60					1,5,8,10
(e) ALE w/ O ₂ ashing	40	CH ₃ F/Ar = 15/485	~ 25	4	20	40	Ar = 500	330	60	40	O ₂ =500	300	10	1,5,8,10
(f) ALE (Plasma-wall interaction)	40	CH ₃ F/Ar = 15/485	~ 25	4	20	40	Ar = 500	330	60					5
(g) ALE (Gas transition study)	40	CH ₃ F/Ar = 15/485	~ 25	4	1, 20	40	Ar = 500	330	60					5

To study the interaction between the plasma and the wall surfaces, which affects the ALE stability, the chamber wall conditions were intentionally varied ^{7) 8)}. As a pretreatment, cleaning was performed with O₂ plasma for 300 s. After that, irradiation with C₄F₈/Ar plasma was performed for 0, 90, and 180 s to deposit the polymer on the chamber wall. Thereafter, SiN ALE was performed to evaluate the etching rate uniformity. As the chamber wall condition will cause a C/F density fluctuation in the plasma, the effect of the plasma–wall interactions can be analyzed. The transition time between each step is also important to evaluate the C/F density fluctuation in the adsorption and desorption steps. To study the effect of residual gas in the previous step, ALE was performed by changing the gas transition time between the adsorption and desorption steps. After O₂ plasma cleaning as a pretreatment, we set the CH₃F/Ar gas flow for 20 s as the gas flow stabilization step. CH₃F/Ar plasma were irradiated for 4 s as the adsorption step. Then, as the gas transition step, Ar gas was flowed for 20 or 1 s. In the following desorption step, Ar plasma was irradiated for 60 s, and finally O₂ flash was performed to evaluate the etching rate uniformity.

6.3 Accuracy evaluation of film thickness measurements

The film thickness was evaluated using SE; however, there was an issue with the measurement accuracy because the film thicknesses were extremely thin. Therefore, the accuracy of the film thickness measurement was evaluated by XPS and TEM. In XPS, the HFC polymer thickness (d_{HFC}) was calculated from the Si (2p) peak area ratio of the SiN. The decrease in Si (2p) intensity, absorbed by the upper HFC polymer, was compared with that of the initial SiN⁹⁾¹⁰⁾. The formula for the HFC polymer thickness is as follows:

$$d_{HFC} = -\lambda_{Si(2p)} \ln \left(\frac{I_{Si(2p)}}{I_{Si(2p)}^{ref}} \right) \quad (1)$$

Here, $\lambda_{Si(2p)}$ is the mean free path of the Si (2p) photoelectrons in the HFC polymer layer. $\lambda_{Si(2p)}$ was set as 2.5 nm in this study. The Si (2p) peak areas of the HFC polymer/SiN sample and initial sample are $I_{Si(2p)}$ and reference of $I_{Si(2p)}$, respectively. Matsui et al. reported an assumed escape depth [$\lambda_{Si(2p)}$] of 3 nm¹⁰⁾. The difference was proposed to result from the composition variations of the HFC polymer. The densification by sputtering in Ar plasma desorption might be the origin of the escape depth decrease in this experiment. After the Ar plasma desorption step, many C–C bonds were generated in the HFC polymer, compared with CH₃F/Ar plasma. Figure 6-2(a) shows the HFC polymer thickness measured by SE and XPS. Figure 6-2(b) shows the thicknesses measured by TEM. These figures confirmed that there was a correlation between the HFC polymer film thickness measured by SE, XPS, and TEM. Therefore, the film thickness of the HFC polymer can be measured with high accuracy by SE.

Under the HFC polymer, the modified-SiN layer was generated as shown in Fig. 6-2(b). This layer was assumed to comprise of mainly Si and N since SE results show that the optical constant of this layer is similar to that of SiN films. This layer could also contain some mixture

of C, F, and H. The thickness of the modified-SiN layer is assumed to be defined by the Ar penetration depth and dose in the desorption step. Further study is required to understand the modified layer generation during ALE because the modified layer generation is important to understand the ALE surface reactions.

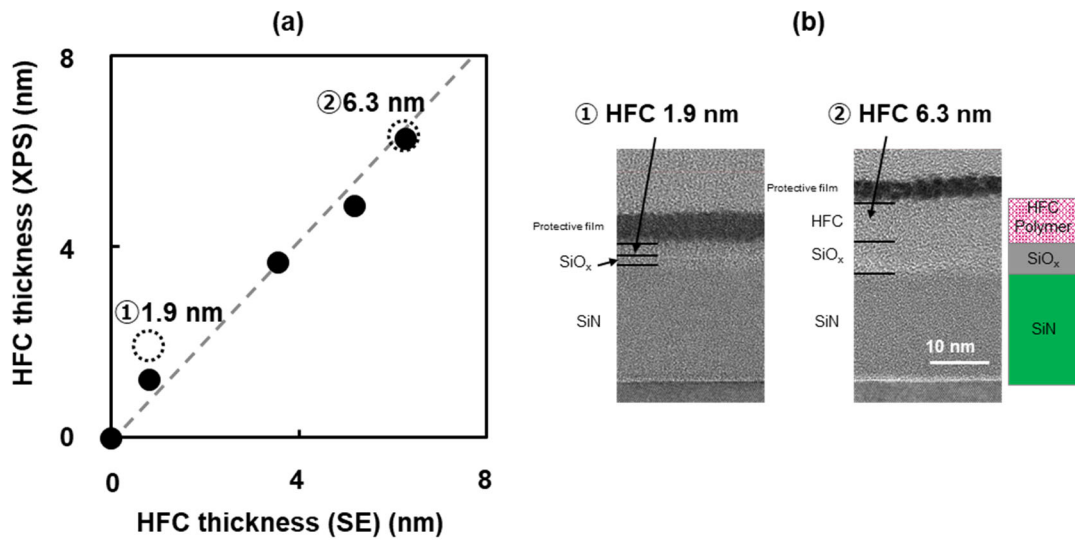


Fig. 6-2 (a) HFC polymer thicknesses after the adsorption step, measured by XPS vs SE. Dotted circles denote the thicknesses measured by TEM and (b) TEM images [experimental condition; Table 6-1 (a)].

6.4 SiN ALE etch stop

We studied the optimization of the adsorption step. An HFC film with a thickness of 2 nm was used in a previous study⁵⁾. Thus, the target of the HFC thickness was set to be 2 nm. Figure 6-3 shows the HFC thicknesses as a function of the process time. The HFC thickness increased linearly with the process time. A 2.6-nm-thick HFC polymer, deposited on SiN, was used as the adsorption step. The desorption time by Ar plasma was set to 10 s. By using this ALE sequence, we studied the cycle number dependence of SiN ALE. The cycle number was changed

from 0 to 10. Figure 6-4 shows the cycle number dependence of the film thickness change of HFC and SiN. The etched amount for one cycle was 0.58 nm. Etching proceeded up to two cycles; however, we observed an etch stop of SiN after ten cycles of ALE, owing to the deposition (>6 nm) of a protective film on the surface. To study the etch-stop phenomena in detail, certain changes to the conditions were also studied (not shown here). In the case of thin HFC adsorption (1.2 nm), an etch stop was also observed regardless of conditions. When the desorption times were changed from 10 to 60 s, we also observed an etch stop. It was concluded that the etch stop is an important issue for stable SiN ALE.

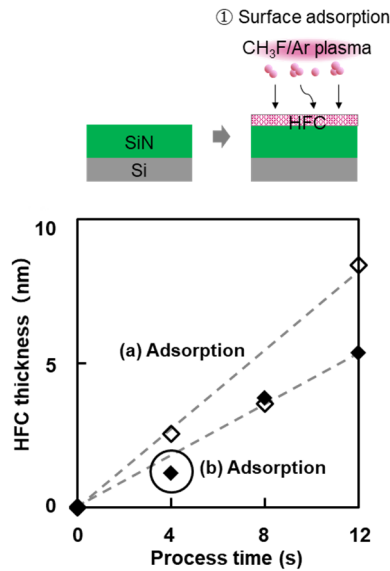


Fig. 6-3 HFC thicknesses as a function of adsorption process time
[experimental condition; Tables 6-1 (a) and (b)].

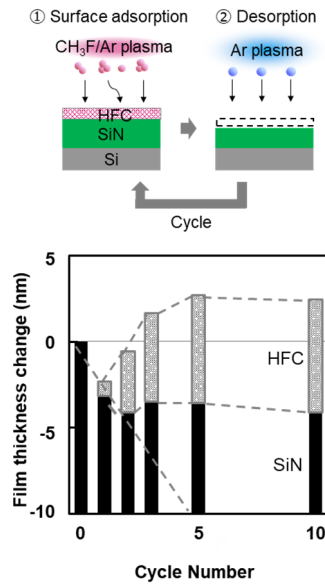


Fig. 6-4 Cycle number dependence of surface location of HFC and SiN

[experimental condition; Tables 6-1 (c)].

6.5 Analysis of etch-stop mechanism

To investigate the etch-stop mechanism, the chemical bonding on the SiN surface after one and ten cycles was analyzed by XPS. Figure 6-5 shows the C (1s) peak which is decomposed into each chemical bond. The binding energies of C–C, C–N, and C–F were 284.8, 286.3, and 287.4 eV, respectively. Figure 6-5(c) shows the cycle number dependence of the peak area ratio of each bond to the total C (1s) XPS spectra. The ratio of C–C bonds increased with the cycle number of ALE. The bond strength of the C–C bond is 6.4 eV.

It is known that carbon atoms in amorphous carbon films (a-C) hybridize their outermost s and p orbitals of carbon into sp^3 and sp^2 hybrids. Thus, we investigated the sp^3 and sp^2 hybrids by C (1s) spectrum. The binding energy of sp^3 in a-C is 285.2 eV, and the binding energy of sp^2 is 284.4 eV.^{24,25} The binding energy of sp^3 and sp^2 was added to Fig. 6-5(a), and we found that it forms an sp^3 hybrid orbital (similar to diamondlike carbon). Therefore, the HFC polymer, which

has many C–C bonds, is difficult to sputter, which results in the etch stop of SiN ALE. In Fig. 6-2(b), the modified SiN layer was generated under the HFC polymer. During air exposure, the oxygen containing layer is also possible to generate under the HFC polymer. Thus, we investigated the C–O and Si–O related peaks in the C (1s) and O (1s) XPS spectra. However, it was found that the oxidation of modified layer under the HFC polymer is of nondetectable level. Thus, we concluded that the modified layer under the HFC polymer is the modified SiN layer as shown in Fig. 6-2(b).

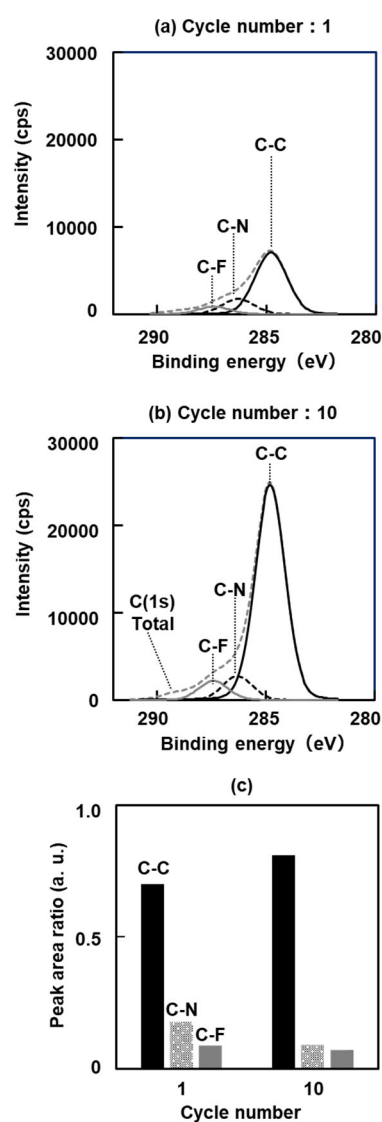


Fig. 6-5 (a) XPS spectra of C(1s) on adsorbed HFC layers after one-cycle ALE, (b) ten-cycle ALE process, and (c) decomposed C–C, C–N, and C–F bond area ratio as a function of cycle number.

Figure 6-6 shows a schematic of the etch-stop model after adsorption, and after one cycle and ten cycles of ALE. In the adsorption step, the HFC polymer was deposited on SiN. After one cycle of ALE, it was difficult to remove the carbon completely. Strong C–C bonds remained at the surface. After ten cycles, a thick layer of carbon polymer was deposited on the residual carbon. When ions from the plasma pass through the polymer during etching, approximately 200 eV of kinetic energy of the incident ion is reported to be lost in a polymer with a thickness of 1 nm¹¹⁾. At 330 eV, which is maximum ion energy of our experimental condition, etching progresses when the polymer thickness is less than 1.5 nm, and etching stops when the film thickness exceeds 1.5 nm from the published results. As shown in Fig. 6-4, etching progresses through the HFC polymer with a thickness of 0.81 nm at cycle 1. It is expected that etching will proceed when there is energy above 162 eV, in the case that the polymer film thickness is 0.81 nm. However, the ALE ceased after cycle 2 since the polymer thickness of 3.55 nm is much thicker than the threshold thickness of 1.5 nm. Thus, these results are almost consistent with the previous data, published by Tatsumi et al. The detailed study of energy loss rate differences in the polymer is a topic of future research, as our study is a rough estimate.

Thus, a thick carbon layer causes an etch stop, and suppression of C deposition is required for stable SiN ALE. Although we focused on the effect of the C–C bond in the HFC polymer, there are other possibilities that can cause the etch stop of SiN ALE. Another possible reason is that Si–C bonds are formed on the surface^{12) 13) 14)}. As the binding energy of Si–C in the C (1s) photoemission (283.0 eV) is close to the peak position of a strong C–C (284.8 eV) bond, it was difficult to deconvolute the effect of Si–C. As Si–C is generated in the interface between HFC polymer and underlying SiN, the signal of Si–C seems to be under the detectable-level since the upper HFC polymer suppressed the photoelectron from the interface. Further study will be performed related to the Si–C bond by using other techniques.

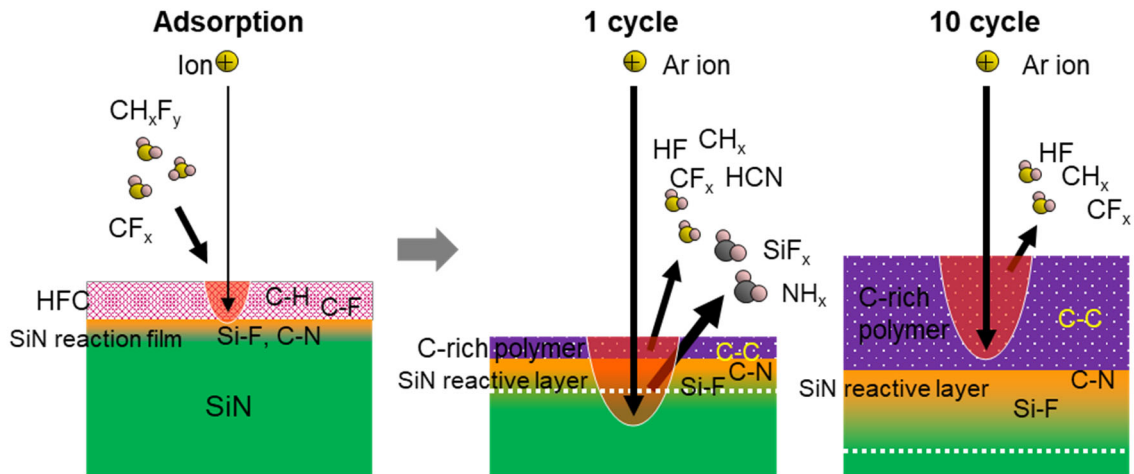


Fig. 6-6 Schematic models after the adsorption step, one-cycle ALE, and ten-cycle ALE.

6.6 Proposed sequence for stable ALE

For the suppression of excess carbon, physical removal by ion or chemical processes is two possible methods to realize stable ALE. In the case of physical removal using ions, however, longer Ar exposure caused sputtering of the underlayer. Therefore, we focused on the chemical removal. Desorption by O_2/Ar plasma and three-step ALE with O_2 ashing processes were investigated. Although the desorption by O_2 plasma has been reported for SiO_2 ALE,³⁰ SiN ALE with an O_2 -based process has not been reported (to the best of our knowledge).

To investigate the effect of oxygen, the desorption step with O_2/Ar plasma was examined. The desorption time was 60 s and 0–10 cycles of ALE were performed. Figure 6-7 shows the etched amount per cycle (EPC) as a function of cycle number in the case of a desorption step by O_2/Ar plasma. The EPC was 0.89 nm/cycle. SiN ALE proceeded continuously by the O_2/Ar plasma desorption step. The HFC polymer deposition was suppressed by O_2 addition. Next, we examined a three-step ALE with O_2 ashing. The desorption and ashing times were 60 and 10 s, and 0–10 cycles of ALE were performed. Figure 6-8 shows the EPC as a function of cycle number

CHAPTER 6

in the case of the three step ALE with O₂ ashing. The EPC was 1.52nm/cycle. Therefore, the O₂ ashing step effectively removed the HFC polymer.

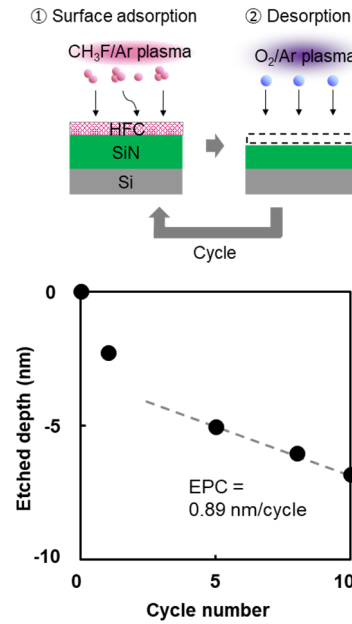


Fig. 6-7 Etched depths as a function of cycle number in the case of a desorption step by O₂/Ar plasma [experimental condition; Tables 6-1 (d)].

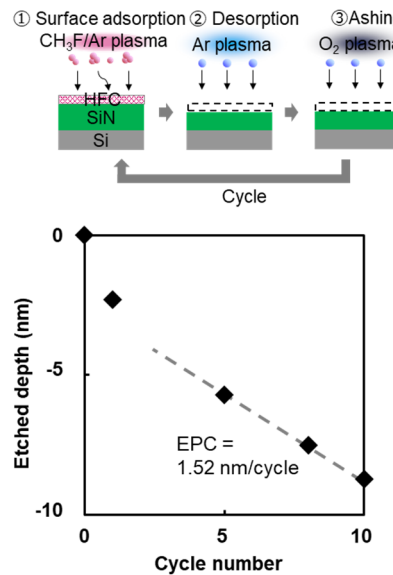


Fig. 6-8 Etched depths as a function of cycle number in the case of three-step ALE with subsequent O₂ ashing [experimental condition; Tables 6-1 (e)].

The EPC of the three-step ALE was much higher than that of O_2/Ar desorption. We discuss the amount of fluorine during ALE because the EPC of SiN is strongly related to the amount of fluorine on the SiN surface. The high EPC of the three-step ALE was caused by the presence of abundant fluorine atoms in the HFC during Ar desorption, compared with O_2/Ar desorption. In the case of the three-step ALE with O_2 ashing, the HFC film remained in the desorption step. This caused the high EPC of SiN ALE. In the case of O_2/Ar desorption, the HFC was removed simultaneously during the desorption step. This caused the low EPC. As the three-step ALE is appropriate for device manufacturing, we used three-step ALE in the subsequent investigations. We also confirmed that EPC of first and second cycles was higher than that for the other cycles. Impurities from the plasma, which were implanted in the SiN surface during ALE cycles, modified the SiN surface to cause the decrease of the SiN EPC with additional cycles.

6.7 SiN ALE fluctuation

A key parameter of SiN ALE is the amount of fluorine, which dominantly contributes to SiN etching. In addition, the amount of carbon affects the EPC fluctuation in ALE. Excess carbon causes the etch stop and less carbon may cause the low EPC. As the amounts of fluorine and carbon are important, the effect of density fluctuations by C/F species was studied.

As the plasma–wall interactions were reported to cause the C/F density fluctuation^{9) 15)}, the chamber wall condition was intentionally changed. We performed the O_2 cleaning and polymer deposition with C_4F_8/Ar plasma. The deposition time was 0, 90, or 180 s. Then, we performed the SiN ALE for five cycles using the same conditions (Fig. 6-9). Figure 6-10 shows the etched depth uniformity differences with and without chamber wall polymer deposition. The etched depth at the wafer edge increased drastically. We proposed that the desorbed species from the wall surface affected the etch rate fluctuation. Because CF_2 , measured by appearance mass

spectroscopy, is reported to be desorbed from the deposited polymer with Ar ion injection,³¹ desorbed CF_2 enhance the EPC at the wafer edge during Ar desorption. When we investigated the optical emission spectra of CF_2 ($\lambda = 262.5 \text{ nm}$) during the Ar desorption step (not shown here), a clear increase of the CF_2 radical was detected with the chamber wall deposited conditions. In the case of O_2 cleaning, however, the CF_2 desorption from the chamber wall was suppressed. We concluded that the chamber wall condition is important for stable ALE processes. Under the condition that there was no deposition on the reactor wall, the etched depth uniformity across the wafer was poor. However, it can be improved by optimizing the Ar desorption process.

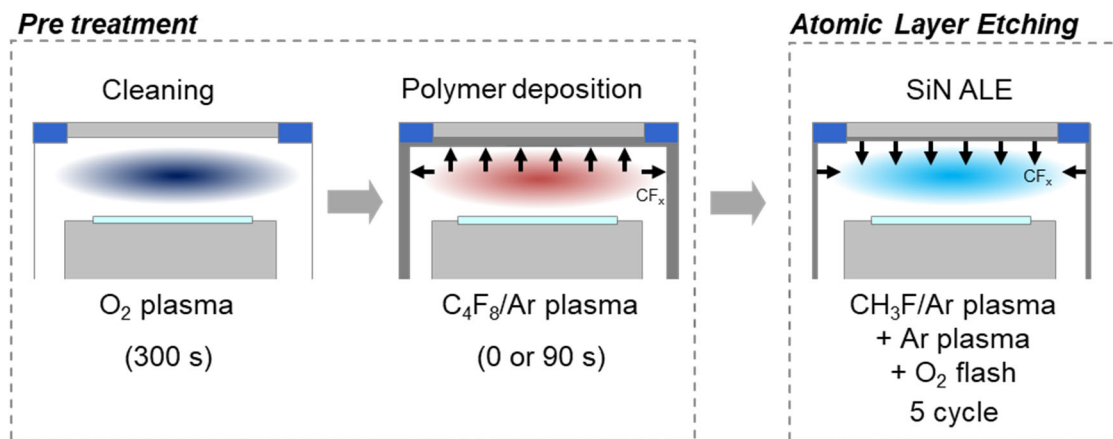


Fig. 6-9 Schematic of the experiment to investigate the plasma-wall interactions.

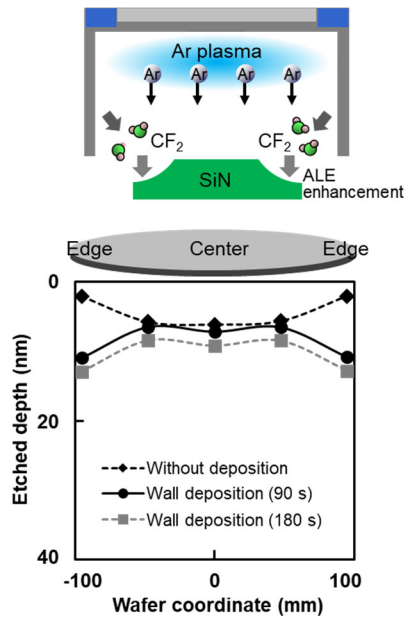


Fig. 6-10 Etched depth uniformity differences with and without polymer deposition on the chamber wall [experimental condition; Tables 6-1 (f)].

Next, we studied the effect of residual gases from the previous step. A mixture of residual gas from the previous step might cause C/F density fluctuation. We changed the gas transition time before the Ar desorption step from 20 to 1 s (Fig. 6-11). Figure 6-12 shows the etched depth uniformity differences at gas transition times of 1 and 20 s as a function of wafer coordinate. There was almost no difference in etched depth after ALE (adsorption and desorption) with gas transition times of 20 and 1 s. We found that residual gases have almost no impact on ALE because the gas residence time under the experimental condition was 63 ms, which is much shorter than the gas transition time (1 s). Therefore, the transition time has a negligible effect on the etched depth fluctuation.

We proposed the fluctuation model of SiN ALE caused by the plasma–wall interaction. CF₂ desorption from the chamber wall caused the ALE enhancement. Therefore, we need to clean

the chamber before ALE. We found that control of fluorine and carbon amounts is critical for stable SiN ALE.

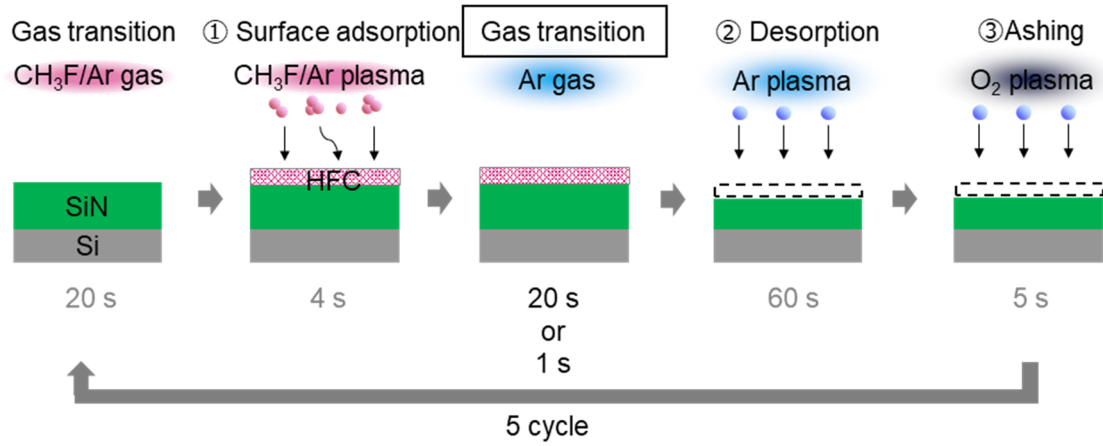


Fig. 6-11 Schematic illustration of experiments for gas transition time dependence.

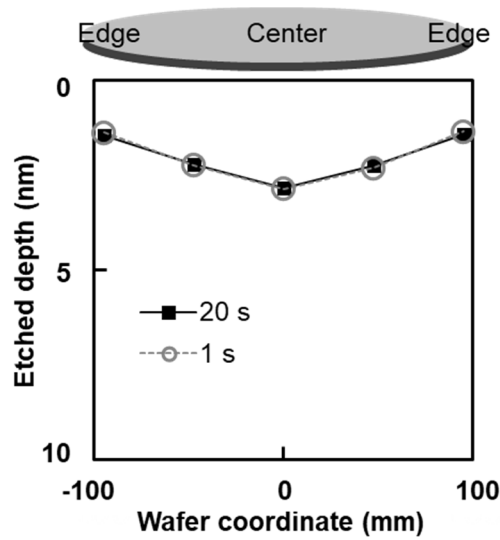


Fig. 6-12 Etched depth uniformities as a function of wafer coordinate with different gas transition time (20 vs. 1 s) [experimental condition; Tables6-1 (g)].

6.8 Conclusions

ALE has been studied extensively for surface reactions, and thus, little has been reported about the fluctuation of ALE performances in device fabrication. In this study, we investigated SiN ALE with process optimization of the adsorption and desorption steps, and we focus on the cycle number dependence of EPC fluctuation of ALE. We also studied the ALE performance variation caused by the chamber wall conditions. Excess polymer deposition, which originates from residual carbon after desorption step, causes the etch stop of SiN ALE. The reason of residual carbon is that the HFC polymer, which has many C–C bonds, is difficult to sputter. Thus, a thick carbon layer causes an etch stop, and suppression of C deposition is required for stable SiN ALE. Addition of O₂ to the desorption step or a three-step O₂ ashing process can suppress C deposition and realize stable ALE. The high EPC of the three-step ALE was caused by the presence of abundant fluorine atoms in the HFC during Ar desorption, compared with O₂/Ar desorption. Hence, the three-step ALE is appropriate for device manufacturing. CF_x desorption from the chamber wall causes etch enhancement of ALE. The desorbed CF₂ enhance the EPC at the wafer edge during Ar desorption. We found that control of fluorine and carbon amounts is critical for stable SiN ALE. To realize stable SiN ALE, it is necessary to keep the same surface conditions in every cycle. It is also important to control the influence of desorbed species from the chamber components. As the etching selectivity to other materials is critical for semiconductor device manufacturing, further study related to the selectivity to mask and/or underlying materials is strongly required in the near future.

6.9 References

- ¹ N. Posseme, V. Ah-Leung, O. Pollet, C. Arvet, and M. Garcia-Barros: *J. Vac. Sci. Technol. A* **34**, 061301 (2016).
- ² S. D. Sherpa and A. Ranjan: *J. Vac. Sci. Technol. A* **35**, 01A102 (2017).
- ³ K. Nakane, R. H. J. Vervuurt, T. Tsutsumi, N. Kobayashi, and M. Hori: *ACS Applied Materials & Interfaces* **11**, 37263 (2019).
- ⁴ C. Li, D. Metzler, C. S. Lai, E. A. Hudson, and G. S. Oehrlein: *J. Vac. Sci. Technol. A* **34**, 041307 (2016).
- ⁵ Y. Ishii, K. Okuma, T. Saldana, K. Maeda, N. Negishi, and J. Manos: *Jpn. J. Appl. Phys.* **56**, 06HB07 (2017).
- ⁶ A. Hirata, M. Fukasawa, K. Kugimiya, K. Nagaoka, K. Karahashi, S. Hamaguchi, and H. Iwamoto: *Jpn. J. Appl. Phys.* **59**, Sjjc01 (2020).
- ⁷ M. Schaepkens, R. C. M. Bosch, T. E. F. M. Standaert, G. S. Oehrlein, and J. M. Cook: *J. Vac. Sci. Technol. A* **16**, 2099 (1998).
- ⁸ M. Fukasawa, A. Kawashima, N. Kuboi, H. Takagi, Y. Tanaka, H. Sakayori, K. Oshima, K. Nagahata, and T. Tatsumi: *Jpn. J. Appl. Phys.* **48**, 08HC01 (2009).
- ⁹ T. E. F. M. Standaert, M. Schaepkens, N. R. Rueger, P. G. M. Sebel, G. S. Oehrlein, and J. M. Cook: *J. Vac. Sci. Technol. A* **16**, 239 (1998).
- ¹⁰ M. Matsui, F. Uchida, M. Kojima, T. Tokunaga, F. Yano, and M. Hasegawa: *J. Vac. Sci. Technol. A* **20**, 117 (2002).
- ¹¹ T. Tatsumi, M. Matsui, M. Okigawa, and M. Sekine: *J. Vac. Sci. Technol. B* **18**, 1897 (2000).
- ¹² G. J. C. Jr. and G. S. Oehrlein: *Applied Physics Letters* **47**, 604 (1985).
- ¹³ R. Blanc, F. Leverd, T. David, and O. Joubert: *Journal of Vacuum Science & Technology B* **31**, 051801 (2013).
- ¹⁴ R. Blanc, C. Jenny, S. Lagrasta, F. Leverd, and O. Joubert: *Journal of Vacuum Science & Technology B* **32**, 021806 (2014).
- ¹⁵ M. Fukasawa, A. Kawashima, N. Kuboi, H. Takagi, Y. Tanaka, H. Sakayori, K. Oshima, K. Nagahata, and T. Tatsumi: *Japanese Journal of Applied Physics* **48**, 08HC011 (2009).

CHAPTER 7

Stabilization of SiN by multi-step ALE

7.1 Introduction

As the size of semiconductor devices approaches the atomic/molecular level an improvement of the precision of dry etching technologies becomes increasingly indispensable. ALE enables atomic-precision control of the surface reaction etching with low damage to underlying layers in device fabrication ¹⁾. Basically, ALE consists of an adsorption and a desorption step. By combining the different approaches to the adsorption and desorption steps, various methods of ALE can be investigated. In typical Si ALE, Cl_2 is generally used in the adsorption step ²⁾. Cl_2 is adsorbed on a Si substrate and irradiated with Ar plasma as the desorption step to form SiCl_4 , which is a volatile reaction by-product, and etching is performed ³⁾. A FC polymer or HFC polymer are used for SiO_2 or SiN ALE ^{4,5)}. As SiN etching with a CW plasma generally involves a CH_3F plasma ^{6,7)}, which can obtain a high selectivity over Si and SiO_2 , the HFC polymer from the CH_3F plasma is also used for the adsorption step in SiN ALE. Recently, ALE has been applied to etch the difficult-to-etch materials. The difficult-to-etch materials are those where the reaction of their by-products with halogen-based plasma is non-volatile. In particular, it has been reported that the surface modification with hydrogen plasma is effective to etch such difficult-to-etch materials ^{8,9)}. Because these three kinds of ALE generally use ions in the desorption step, an anisotropic profile can be realized. However, ion injection into the substrate causes serious damage, which in turn degrades the device performance.

To overcome the damage generation issue, thermal ALE has been actively studied recently as a damage-less ALE with isotropic processing ¹⁰⁾. Thermal ALE is also a prospective candidate for the etching of difficult-to-etch materials. A metal complex is generated on the surface, which is desorbed by the thermal process.

In this study, we focus on SiN ALE ¹¹⁻¹⁵⁾ with CH_3F plasma adsorption and Ar plasma desorption. It has been reported that SiN ALE using a CCP system stops the etching reaction,

owing to the excess deposition of polymer on the SiN surface, which has enabled the conclusion that the process stability of ALE is important¹⁶⁾. However, the plasma source dependence of the etch-stop mechanisms are unknown. We investigate the effect of the surface condition on the stability of the EPC in SiN ALE by using an ICP system.

7.2 Experimental conditions

An ICP reactor with a source frequency of 13.56 MHz and a wafer bias frequency of 0.4 MHz was used for the ALE process. As an etching sample, SiN (20 nm) was deposited on the Si substrate. First, a CH₃F/Ar plasma was applied to deposit the HFC polymer on SiN as the adsorption step. The bias power was set at 0 W, which meant that the incident ion energy to the wafer was approximately equal to the plasma potential (~15 eV). Then, an Ar plasma was used for the desorption step. The V_{pp} of the bottom electrode (0.4 MHz) was 140 eV in the Ar desorption step. The total gas flow rate was 500 sccm. This was the etching cycle composed of two steps (Fig. 7-1(a)). We also used a three-step ALE process, where an O₂ flash step without bias power was applied after the Ar desorption step (Fig. 7-1(b)).

To accurately simulate the atomic-level surface reactions, we used a classical molecular dynamics (MD) simulation with modified Stillinger–Weber (SW)-type interatomic potential functions¹⁷⁾. The details of the MD simulation have been reported elsewhere^{18,19)}. All the incident species including ions were treated as charge-neutral atoms in our MD simulation. In the actual ALE process, the charge of the incident ions is known to be neutralized through an Auger emission process after injection of substrates^{20,21)}. Thus, we proposed that the effect of charges on the ions was negligible. The substrate used in the simulation of this study was stoichiometric Si₃N₄. The cross-section of the initial SiN substrate was a rectangle of 4.035 nm × 2.33 nm and the depth of the substrate was 2.25 nm. Periodic boundary conditions were used in the horizontal directions so

that the system represented an infinitely wide surface layer.

For the modification step in the ALE sequence, CH₃F hydrofluorocarbon molecules were introduced in the system to chemically modify the Si₃N₄ surface. The incident energy was fixed at 0.5 eV. As the desorption step, Ar was employed to physically remove the surface reacted layer with an incident energy of 50 eV. The Ar dosage was $5.32 \times 10^{16} \text{ cm}^{-2}$. The conditions for each experiment are shown in Tables 7-1.

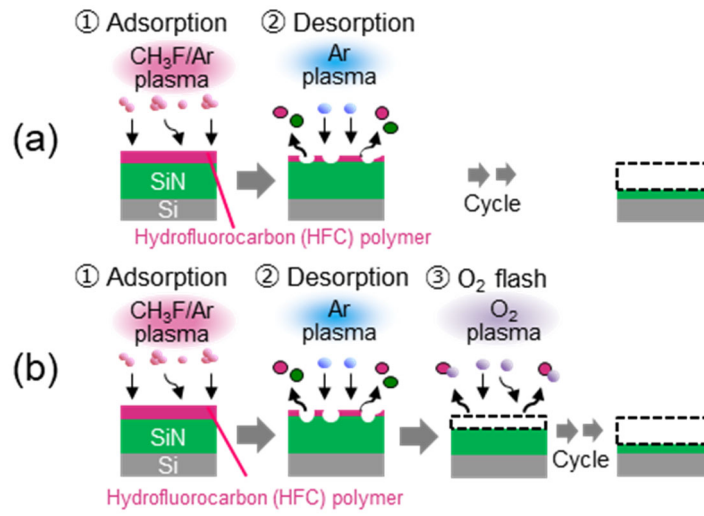


Fig. 7-1 Schematic of (a) Experiment of SiN ALE, and (b) experiment of 3-step SiN ALE.

Table 7-1 Experiment.

Experiment	Etch type	Adsorption					Desorption					O ₂ etch					Desorption					Cycles		
		Pressure (mTorr)	Gas flow rate (sccm)	Ion energy (eV)	Time (s)	Time (s)	Pressure (mTorr)	Gas flow rate (sccm)	Ion energy (eV)	Time (s)	Time (s)	Pressure (mTorr)	Gas flow rate (sccm)	Ion energy (eV)	Time (s)	Time (s)	Pressure (mTorr)	Gas flow rate (sccm)	Ion energy (eV)	Time (s)	Time (s)			
(a) ALE	SiN	25	CHF ₃ /Ar = 10/400	- 15	9	20	25	Ar = 500	140	30											1, 2, 3, 5			
(b) 1 step ALE	SiN	25	CHF ₃ /Ar = 10/400	- 15	9	20	25	Ar = 500	140	30	25	O ₂ =50	- 15	30							1, 2, 3, 5			
(c) 3 step ALE	SiO ₂	25	CHF ₃ /Ar = 10/400	- 15	9	20	25	Ar = 500	140	30	25	O ₂ =50	- 15	30							1, 2, 3, 5			
(d) ALE	SiO ₂	25													CHF ₃ /Ar = 0/400	- 15	6	20	25	Ar = 500	140	15, 30, 40, 120	1	
(e) ALE	SiO ₂	25													CHF ₃ /Ar = 0/400	- 15	6	20	25	Ar = 500	140	120	1, 5	
(f) Multi-step ALE	SiN	25	CHF ₃ /Ar = 10/400	- 15	9	20	25	Ar = 500	140	30	25	O ₂ =50	- 15	30	20	CHF ₃ /Ar = 0/400	- 15	6	20	25	Ar = 500	140	120	5, 5

7.3 Mechanism of SiN etch-stop

Figure 7-2 shows the EPC fluctuation in conventional ALE (Fig. 7-1(a)). The etch-stop of SiN arose from the excess deposition of HFC polymer on SiN ¹⁶⁾. This phenomenon was also confirmed in the CCP experiments of Chapter 6 and is a common issue for SiN ALE. The major difference between CCP and ICP is the dissociation degree of CH₃F molecules. The high-density ICP intensively dissociates the CH₃F molecules, which yields a large number of F atoms. Thus, adsorption of a less-carbon containing polymer is expected in the case with the ICP source. However, the etch-stop of SiN ALE occurs even in the case with ICP. Thus, we conclude that the etch-stop of SiN ALE with CH₃F-based plasma adsorption is almost unavoidable so needs to be suppressed.

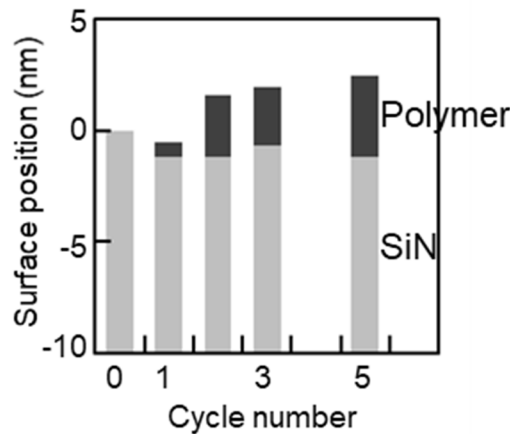


Fig. 7-2 Cycle number dependence of surface location of HFC and SiN [experimental conditions: Table 7-1 (a)].

To investigate the details of SiN surface modification, MD simulation was performed (Fig. 7-3). After deposition of the HFC polymer (2 nm) by CH₂F molecules (0.5 eV), Ar with a kinetic energy of 50 eV ($\sim 10^{16} \text{ cm}^{-2}$) was exposed to the surface. It was confirmed that CH₂F was the major ion/radical species in CH₃F plasma, as measured by a quadrupole mass spectrometer.

From the MD calculation, it was found that many Si-C bonds were formed on the SiN surface after the desorption step. It has been reported that the Si-C bonds are generated on the SiN surface during conventional CW etching ²²⁾, as well as on the Si surface ²³⁻²⁵⁾. Thus, our result from the MD simulation is qualitatively consistent with that from experimental results with a CW plasma.

The main bonds, estimated by MD simulation, were Si-C, C-N, Si-Si, Si-F, C-C (4.63, 7.77, 3.21, 5.93, 6.41 eV). The bond dissociation energies of these bonds are higher than those of other chemical bonds. Especially, Si-C and C-N bonds at the polymer/SiN interface are important for carbon residues. The combining capacity of an atom is defined as the valence. Silicon has a valence of 4 and nitrogen has a valence of 3. As the valence of silicon is higher than that of nitrogen, carbon bonded to Si is more difficult to be desorbed. Thus, we assumed that many Si-C bonds remained on the surface, which was confirmed by MD simulation as well as the reported experiments. Thus, it was proposed that the remaining Si-C bonds (4.63 eV) are a trigger for carbon accumulation. As carbon remains after one cycle of ALE, a thick carbon layer is deposited in the following adsorption step with the CH₃F/Ar plasma. We concluded that this is the root cause of the etch-stop in SiN ALE.

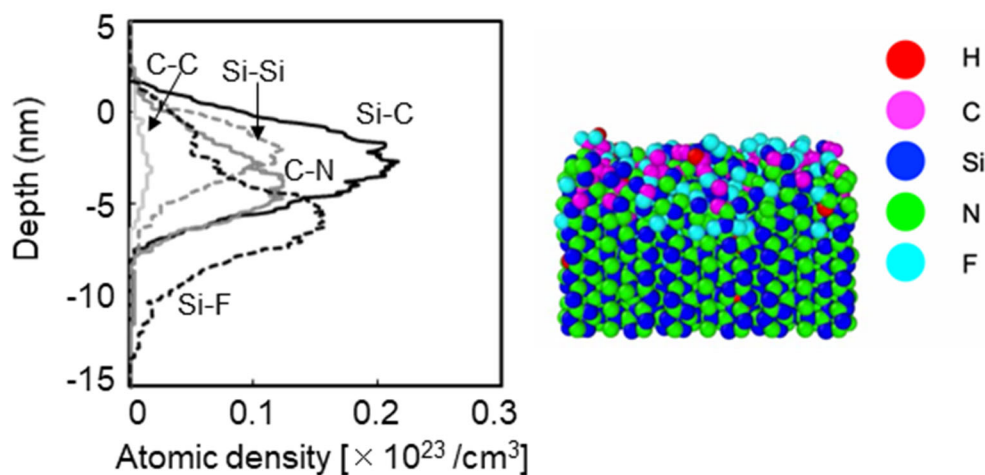


Fig. 7-3 Atomic density of each bond on the SiN surface by MD simulation.

7.4 Suppression of etch-stop and the issue of surface oxidation

To remove the accumulated carbon on the SiN, an O₂ flash step was introduced after Ar desorption (Fig. 7-1(b)). Figure 7-4 shows the total SiN etched amount as a function of cycle number, where the etch-stop was seen to be suppressed with the O₂ flash step, though the EPC was decreased after one cycle of ALE. Because O₂ plasma typically induces surface oxidation of SiN, surface bonding was analyzed by XPS (initial vs. post-ALE).

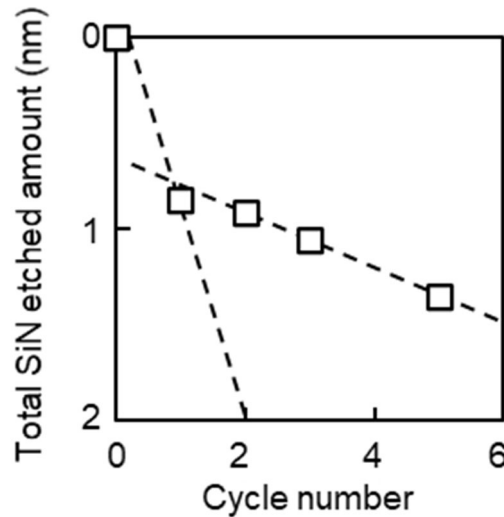


Fig. 7-4 Cycle number dependence of total SiN etched amount [experimental conditions: Table 7-1 (b)].

Figure 7-5 shows the XPS spectra of Si (2p) after three cycles of ALE. The binding energies of Si₃N₄ and SiO₂ are 101.5 and 103.5 eV, respectively. The binding energy of SiO_xN_y is in the range from 102.0 to 103.0 eV. From the XPS peak deconvolution, we found that the SiO_xN_y bond was below the detection limit. As the detected bonding was only from SiO₂ and Si₃N₄, we concluded that SiO₂ with a negligible amount of H, C, F, Si, and N was generated on the surface by O₂ flashing. Because the SiO₂ film thickness was thin, a Si₃N₄-related peak of the underlying SiN was detected. The thickness of the SiO₂ on SiN after each cycle was measured by SE (Fig. 7-

6). The XPS peak area ratio of oxygen as a function of ALE is also shown in Fig. 6. SiO_2 had an almost constant film thickness, which caused a constant EPC decrease in the ALE process. A SiO_2 film with a thickness of 0.75–0.9 nm was found to be generated. It has also been reported that SiO_2 is formed between the SiN surface and the CF polymer when irradiated with a $\text{C}_4\text{F}_8/\text{Ar}/\text{O}_2$ plasma in CW etching²⁶⁾. Thus, we concluded that the EPC decrease after one cycle was caused by the surface oxidation of SiN. Therefore, a stable ALE process requires the removal of SiO_2 after each cycle.

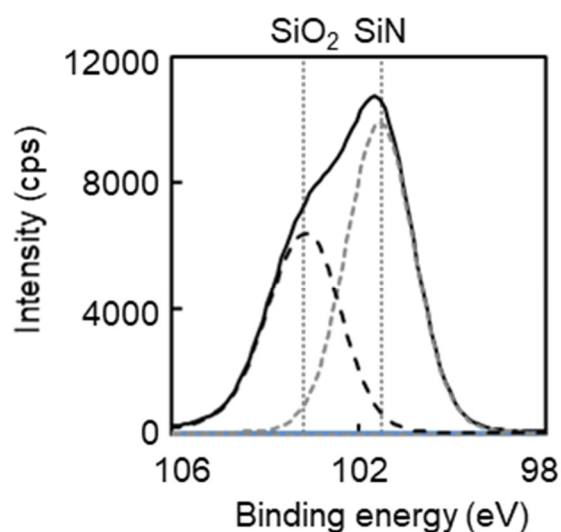


Fig. 7-5 XPS spectra of Si(2p) electron emission on SiN after 3-step ALE [experimental conditions: Table 7-1 (c)].

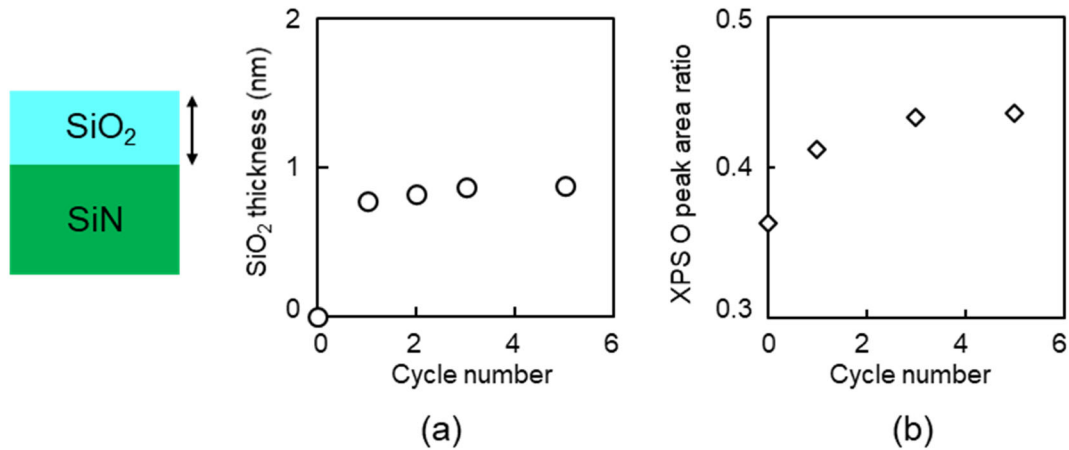


Fig. 7-6 (a) Cycle number dependence of SiO₂ thickness by SE, and (b) cycle number dependence of O (1s) peak area ratio by XPS [experimental conditions: Table 7-1 (c)].

7.5 Plasma-enhanced multi-step atomic layer etching

The SiN surface must become pristine after each cycle. Thus, we developed a multi-step ALE for achieving a stable EPC. The multi-step ALE concept herein is shown in Fig. 7-7, wherein the surface SiO₂ is removed by SiO₂ ALE after the three-step SiN ALE. One etching cycle of SiO₂ ALE comprised two steps^{4,27}; first the C₄F₈/Ar plasma was used to deposit an FC polymer as the adsorption step and an Ar plasma was subsequently used as the desorption step. To analyze the SiO₂ ALE performance, a sample of SiO₂ with a thickness of 100 nm was used. The thickness of SiO₂ was measured by SE with a thermal SiO₂ optical model. Figure 7-8 shows the SiO₂ EPC (one cycle) as a function of Ar desorption time, where a quasi-self-limited behavior of SiO₂ ALE was realized. We used 120 s for the Ar desorption time (EPC of 2.3 nm).

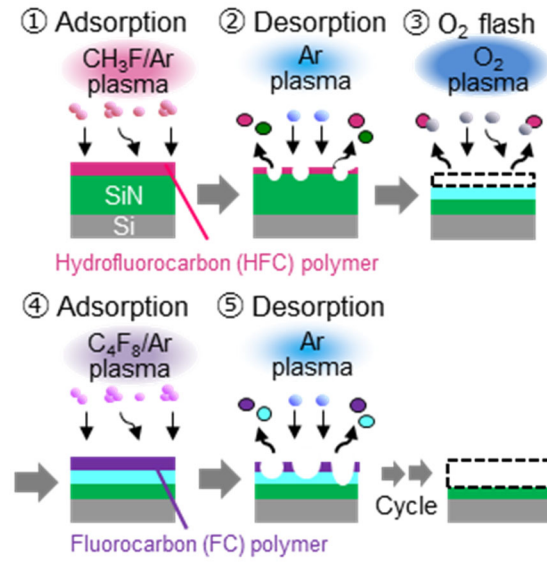


Fig. 7-7 Schematic of experiment of multi-step ALE.

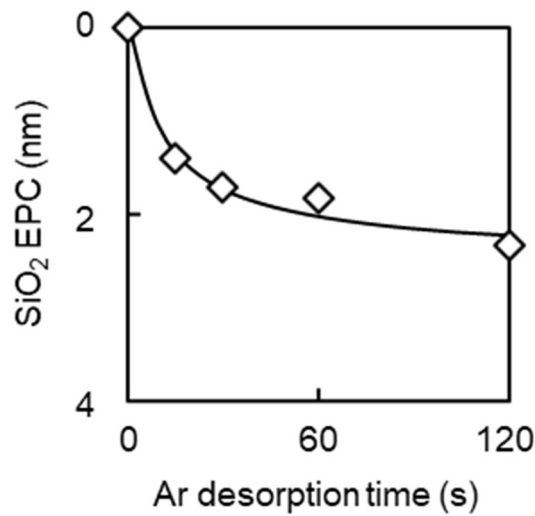


Fig. 7-8 SiO_2 EPC as a function of Ar plasma exposure time [experimental conditions: Table 7-1 (d)].

The total SiO_2 etched amount as a function of cycle number is shown in Fig. 7-9, which demonstrates the realization of a SiO_2 ALE process. Further, no carbon accumulation was observed in the case where the Ar desorption time of the SiO_2 ALE was sufficiently long.

Specifically, oxygen in the SiO_2 generated volatile CO_x as a reaction by-product, which resulted in the removal of residual carbon on the surface. By combining the three-step SiN ALE with a subsequent SiO_2 ALE to remove residual SiO_2 , plasma-enhanced conversion (multi-step) ALE was realized (Fig. 7-10), wherein the EPC fluctuation was suppressed by the precise control of the surface conditions (EPC of 2.6 nm). It was found that the surface became pristine SiN after multi-step ALE, because SiO_2 was completely etched in the additional SiO_2 ALE.

As the etch selectivity of SiN over SiO_2 is very important for device fabrication, we also measured the SiO_2 EPC in multi-step ALE. The EPC selectivity of SiN over SiO_2 was approximately 0.78. The reason why the selectivity was below 1 was because the oxidation thickness of the SiN surface was relatively thin. The total etch amount of multi-step SiN ALE can be defined as the sum of the EPC of SiN and the surface oxidation thickness. The surface oxidation thickness can be controlled by the incident ion energy of oxygen in the O_2 flash step. By controlling the SiO_2 thickness, EPC selectivity can be controlled precisely. Because ALE is extremely sensitive to the surface conditions, an understanding and precise control of the plasma-surface interactions are crucial.

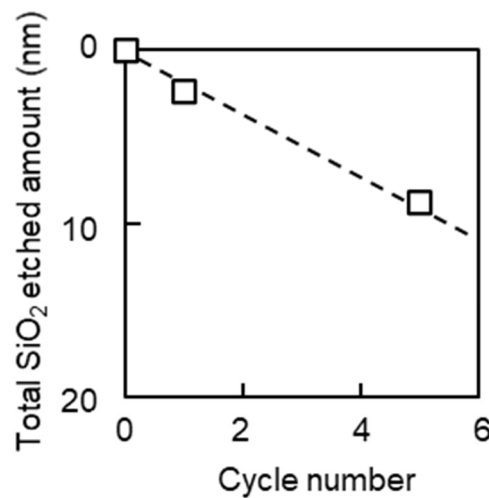


Fig. 7-9 Cycle number dependence of total SiO_2 etched amount [experimental conditions: Table 7-1 (e)].

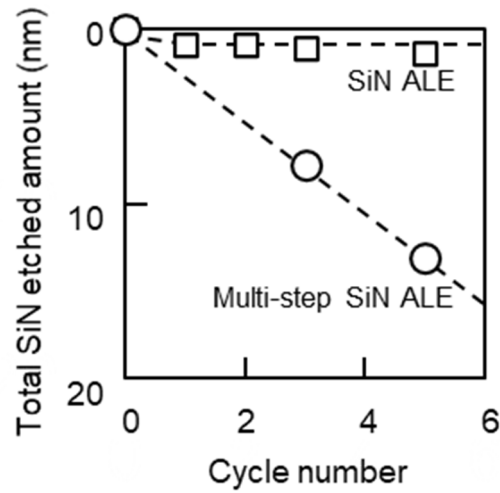


Fig. 7-10 Cycle number dependence of total SiN etched amount after multi-step ALE [experimental conditions: Table 7-1 (f)].

7.6 Conclusions

We investigate the effect of the surface conditions on the stability of the EPC in SiN ALE by using an ICP system. And we investigated the etch-stop mechanism in SiN ALE and examined multi-step ALE for stabilization. Etch-stop of SiN ALE is caused by polymer deposition. MD simulation shows that Si-C bonds remain on the SiN surface after the ALE process. The remaining Si-C bonds are a trigger for carbon accumulation, which is generated during the ALE cycles. The etch-stop is suppressed with an O₂ flash step. However, the EPC decreases after one cycle of ALE, which is caused by the surface oxidation of SiN. For a stable ALE process, the surface SiO₂ is removed by SiO₂ ALE. By optimizing the SiO₂ ALE sequence, a quasi-self-limited behavior of SiO₂ ALE is realized. By combining the three-step SiN ALE with a subsequent SiO₂ ALE to remove residual SiO₂, multi-step ALE is realized. The EPC of SiN is approximately equal to that of SiO₂. Non-selective ALE is developed for next-generation devices. To stabilize the ALE process, because ALE is extremely sensitive to the surface conditions, understanding and precise

control of the plasma–surface interactions are critical.

7.7 References

- ¹ A. Hirata, M. Fukasawa, K. Kugimiya, K. Nagaoka, K. Karahashi, S. Hamaguchi, and H. Iwamoto: *Jpn. J. Appl. Phys.* **59**, Sjjc01 (2020).
- ² Y. Horiike, T. Tanaka, M. Nakano, S. Iseda, H. Sakaue, A. Nagata, H. Shindo, S. Miyazaki, and M. Hirose: *J. Vac. Sci. Technol. A* **8**, 1844 (1990).
- ³ H. J. L. C. J. Mogab: *J. Vac. Sci. Technol. A* **17**, 721 (1980).
- ⁴ D. Metzler, R. L. Bruce, S. Engelmann, E. A. Joseph, and G. S. Oehrlein: *J. Vac. Sci. Technol. A* **32**, 020603 (2014).
- ⁵ M. Honda, T. Katsunuma, M. Tabata, A. Tsuji, T. Oishi, T. Hisamatsu, S. Ogawa, and Y. Kihara: *Journal of Physics D: Applied Physics* **50**, 234002 (2017).
- ⁶ S. Samukawa: *Jpn. J. Appl. Phys.* **32**, 6080 (1993).
- ⁷ M. Matsui, M. Morimoto, and N. Ikeda: *Jpn. J. Appl. Phys.* **54** (2015).
- ⁸ A. Hirata, M. Fukasawa, T. Shigetoshi, M. Okamoto, K. Nagahata, H. Li, K. Karahashi, S. Hamaguchi, and T. Tatsumi: *Jpn. J. Appl. Phys.* **56**, 06HD02 (2017).
- ⁹ A. Hirata, M. Fukasawa, K. Nagahata, H. Li, K. Karahashi, S. Hamaguchi, and T. Tatsumi: *Jpn. J. Appl. Phys.* **57**, 06JB02 (2018).
- ¹⁰ Y. Lee and S. M. George: *S. M. ACS Nano* **9**, 2061 (2015).
- ¹¹ C. Li, D. Metzler, C. S. Lai, E. A. Hudson, and G. S. Oehrlein: *Journal of Vacuum Science & Technology A* **34**, 041307 (2016).
- ¹² Y. Ishii, K. Okuma, T. Saldana, K. Maeda, N. Negishi, and J. Manos: *Jpn. J. Appl. Phys.* **56**, 06HB07 (2017).
- ¹³ S. D. Sherpa and A. Ranjan: *Journal of Vacuum Science & Technology A* **35**, 01A102 (2017).
- ¹⁴ S. D. Sherpa, P. L. G. Ventzek, and A. Ranjan: *Journal of Vacuum Science & Technology A* **35**, 05C310 (2017).
- ¹⁵ K. Nakane, R. H. J. Vervuurt, T. Tsutsumi, N. Kobayashi, and M. Hori: *ACS Applied Materials & Interfaces* **11**, 37263 (2019).
- ¹⁶ A. Hirata, M. Fukasawa, K. Kugimiya, K. Nagaoka, K. Karahashi, S. Hamaguchi, and H. Iwamoto: *Journal of Vacuum Science & Technology A* **38**, 062601 (2020).
- ¹⁷ F. H. Stillinger and T. A. Weber: *Phys Rev B Condens Matter* **31**, 5262 (1985).
- ¹⁸ H. Ohta and S. Hamaguchi: *The Journal of Chemical Physics* **115**, 6679 (2001).

CHAPTER 7

- ¹⁹ K. Miyake, T. Ito, M. Isobe, K. Karahashi, M. Fukasawa, K. Nagahata, T. Tatsumi, and S. Hamaguchi: Japanese Journal of Applied Physics **53**, 03dd02 (2014).
- ²⁰ H. D. Hagstrum: Phys. Rev. **96**, 336 (1954).
- ²¹ D. W. Hess: Journal of Vacuum Science & Technology A: Vacuum, Surfaces, and Films **8**, 1677 (1990).
- ²² T. E. F. M. Standaert, C. Hedlund, E. A. Joseph, G. S. Oehrlein, and T. J. Dalton: Journal of Vacuum Science & Technology A **22**, 53 (2004).
- ²³ G. J. C. Jr. and G. S. Oehrlein: Applied Physics Letters **47**, 604 (1985).
- ²⁴ R. Blanc, F. Leverd, T. David, and O. Joubert: Journal of Vacuum Science & Technology B **31**, 051801 (2013).
- ²⁵ R. Blanc, C. Jenny, S. Lagrasta, F. Leverd, and O. Joubert: Journal of Vacuum Science & Technology B **32**, 021806 (2014).
- ²⁶ M. Matsui, T. Tatsumi, and M. Sekine: J. Vac. Sci. Technol. A **19**, 2089 (2001).
- ²⁷ D. Metzler, C. Li, S. Engelmann, R. L. Bruce, E. A. Joseph, and G. S. Oehrlei: J. Vac. Sci. Technol. A **34**, 01B101 (2016).

CHAPTER 8

Mechanism of ALE damage generation

8.1 Introduction

One of the advantages of ALE is reported to be low-damage etching. Ishii et al. reported that nondetectable RIE-induced damage in the underlying Si surface after SiN ALE, analyzed by TEM, occurs because low ion energy bombardment during the desorption process can be used in the ALE process¹⁾. However, it is impossible to eliminate the plasma-induced damage completely from occurring because the kinetic energy from the ion injection is necessary for anisotropic ALE. Because the detection sensitivity of TEM is relatively low, damage actually remains on the underlying Si surface.

Suppression of the underlying Si substrate damage caused by energetic ion bombardment is one of the most critical issues in advanced devices. The threshold energy for atomic displacement is defined as ΔE_d . In the case of Si, the ΔE_d indicates the energy required for a certain Si atom to move to a stable position between adjacent lattices. The ΔE_d also varies depending on the crystalline orientation, and the smallest displacement energy of a Si crystal (bulk) is reported to be E_d eV and the average displacement energy is 24.0 eV²⁾. It has also been reported that defects near the outermost surface are generated at lower energy (~ 10 eV)³⁾. When we use an ion energy higher than the E_d , the generation of damage in the Si substrate is unavoidable. The floating potential (V_F) of a conventional plasma source, which is generally used in semiconductor manufacturing, is in the range of 10–30 eV. When the ion energies accelerated by the V_F and bias power become larger than the damage generation threshold, ideal damage-less processing is almost impossible. Thus, plasma-induced damage reduction during ALE is investigated.

We have previously investigated ALE of SiN with process optimization of the surface adsorption step and desorption step, and we achieved stable ALE by controlling the precise surface condition⁴⁾. SiN was employed as a spacer material and a contact etch-stop layer. During over

etching of the underlying Si after SiN ALE, plasma-induced damage was induced on the Si substrate. Damage remaining on the Si substrate caused contact resistance fluctuations⁵⁾. As the remaining Si damage degrades the electrical performance, precise control of the incident ion energy is indispensable to minimize damage generation. In this study, we investigate the underlying Si damage in ALE of SiN and clarify the mechanism of damage generation, which result in the low damage etching in ALE.

8.2 Experimental conditions

ICP system was used in this study. The total gas flow rate was 500 sccm. One etching cycle consisted of three steps. CH₃F/Ar plasma was applied to deposit the HFC polymer without bias power in the adsorption step. Then, Ar plasma was used in the desorption step. The V_{pp} of bottom electrode was approximately 140 V. Finally, O₂ plasma was exposed to suppress etch stop owing to polymer deposition⁴⁾. By repeating these steps, we processed the SiN ALE (Fig. 8-1). The HFC polymer was deposited with a thickness of 1.2 nm on SiN, then the reacted layer was desorbed by Ar plasma for 30 s. To remove the residual surface polymer on Si, subsequent O₂ plasma without bias power was applied (O₂ flash process, 10 s)⁴⁾. After O₂ plasma exposure, SiO_x was generated on SiN surface. SiO_x caused etching rate decrease. Further study is required to understand the effect of surface oxidation.

On-wafer monitoring of the ion energy distribution functions (IEDFs) was carried out to analyze the incident ion energies in detail. We used experimental ICP equipment. IEDFs were directly measured by using a gridded retarding field energy analyzer. The details of the system have been provided elsewhere^{6) 7) 8)}. The accuracy of the measured ion energy was confirmed by comparison with the threshold energy of SiO₂ sputtering in Ar plasma. The threshold energy of SiO₂ sputtering in our system was approximately 50 eV. We confirmed that this value was almost

the same as the published data ⁹⁾. The damage thickness of the underlying Si was measured by SE. In the SE analysis, data were fitted using a three-layer model (SiO₂/dislocated Si/substrate) ^{10) 11)}. Dislocated Si was modeled as a mixture of SiO₂ and poly-Si. The penetration depth of an Ar⁺ ion into the Si was simulated by SRIM simulation ^{12) 13)}.

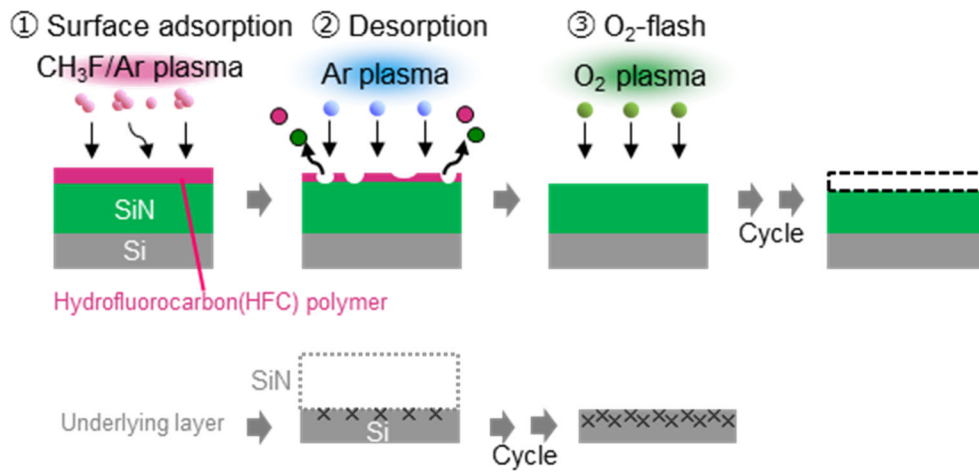


Fig. 8-1 Schematic of experiment of SiN ALE.

8.3 Si damage analysis in SiN ALE over etch

To investigate the low damage etching of underlying Si, we studied the one cycle ALE of SiN. Figure 8-2 shows the eEPC of SiN as a function of Ar plasma desorption time. The result shows the quasi-self-limiting behavior. The EPC of SiN increased for shorter desorption times (<30 s), because the SiN reacted with the HFC polymer and etching progressed. After 30 s, the etched amount became consistent with the physical sputtering of SiN. With adsorption, a quasi-self-limited ALE process was realized. We measured the damage thickness of the underlying Si in the first cycle of ALE. This ALE process had an adsorption step (9 s, <15 eV), desorption step

(30 s, 140 V), and O₂ flash step (10 s, <15 eV). The plasma potential of our system was less than 15 eV, and the process time was approximately 10 seconds in the adsorption step and O₂ flash step. Thus, dominant damage was generated in the desorption step.

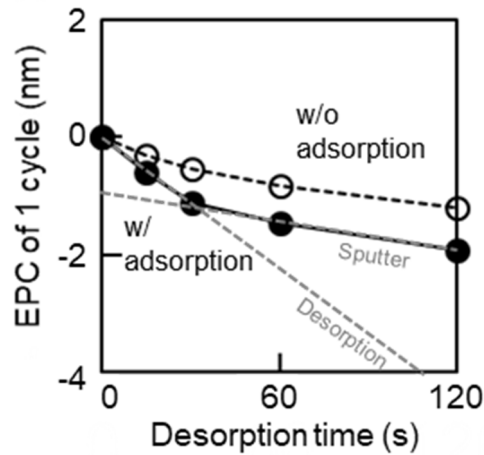


Fig. 8-2 SiN thickness versus desorption time.

Figure 8-3 shows the Si damage thicknesses of untreated Si and the first cycle with relatively long Ar desorption (120 s). The dislocated Si was oxidized by air exposure, which resulted in surface SiO₂ formation. The total damage thickness ($T_{\text{dam_total}}$) was approximately 5 nm. We confirmed that deep damage was generated, even in the case of ALE by using the quasi-self-limiting region. To suppress the damage generation, the use of a lower ion energy and protection film, and control of desorption time, are strongly required.

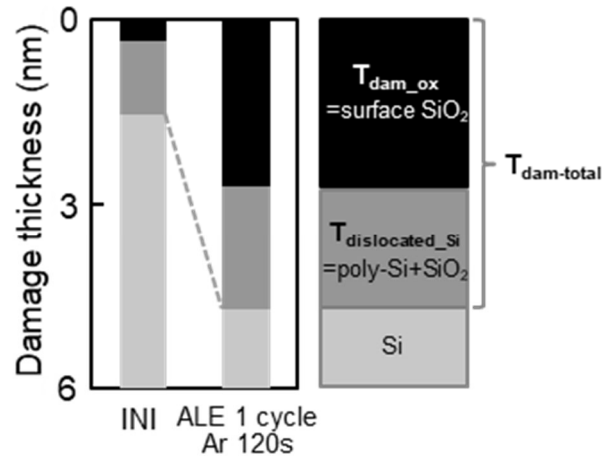


Fig. 8-3 Si damage thickness after ALE.

8.4 Damage analysis in low ion energy

As the damage thickness depends on the ion energy, we investigated the damage generation in the ion energy range below 100 eV. A high bias frequency of 13 MHz was used to minimize the energy split of the two peaks of the IEDF. Figure 8-4 shows the IEDF of Ar plasma (bias power of 30 W and 50 W). The ion energy could be controlled below 50 eV. The IED had a bimodal profile. However, it became a monotonic IED when the bias power was decreased. The plasma potential of the ICP system was in the range from 10 to 15 eV. This was the minimum value of the ion energy in our mass production equipment.

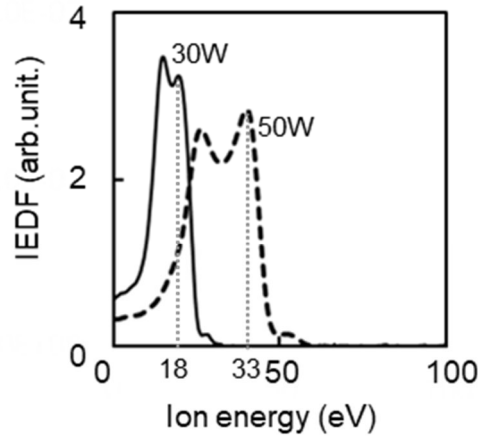


Fig. 8-4 IEDFs of Ar ions (input bias power of 30 W and 50 W).

The threshold energy (V_{th}) for etching has been investigated in the case of chlorine and fluorine from the beam experiment ^{14) 15)}. The absolute values of V_{th} were 4 eV for fluorine and 16 eV for chlorine. In contrast, defects near the outermost surface were generated at an energy of the same order (~ 10 eV). This meant that the damage generation energy was almost the same as that of the etching threshold. Thus, we found that a damage-less process is difficult with the current equipment. Therefore, understanding of the IED profile is extremely important, in the case of low ion energy ALE.

Figure 8-5 (a) shows the dependence of the damage thickness on the Ar plasma exposure time at 30 W and 50 W. A longer Ar plasma exposure resulted in a thicker damage thickness. The damage thickness was saturated at 5 nm after 40 seconds at 30 W, and at 7 nm after 60 seconds at 50 W. Figure 8-5 (a) shows the simulated Ar ion penetration depth into the Si substrate. The simulation was performed using the ion energy value at the high energy peak of the IEDF (V_{hp}) (Fig. 8-4), where 18 eV at 30 W and 33 eV at 50 W were used. Figure 8-5 (b) shows the damage thickness after Ar plasma exposure at 30 W and 50 W (60 s). The projected range of the ion penetration depth was defined as the damage film thickness. The results showed that the damaged

thickness was relatively consistent with the Ar ion penetration depth. Ar plasma irradiation at 50 W for more than 60 seconds sputtered the damaged layer on the surface, and we found that the damaged film thickness was reduced. However, in the case of the 30W condition, there is a correlation between the damaged film thickness and the ion penetration depth. Therefore, it is speculated that the damage thickness is almost saturated after 60 seconds at 50W. Even in the case of ALE, a lower incident ion energy was required to minimize ion-induced damage as well as the conventional dry etching process.

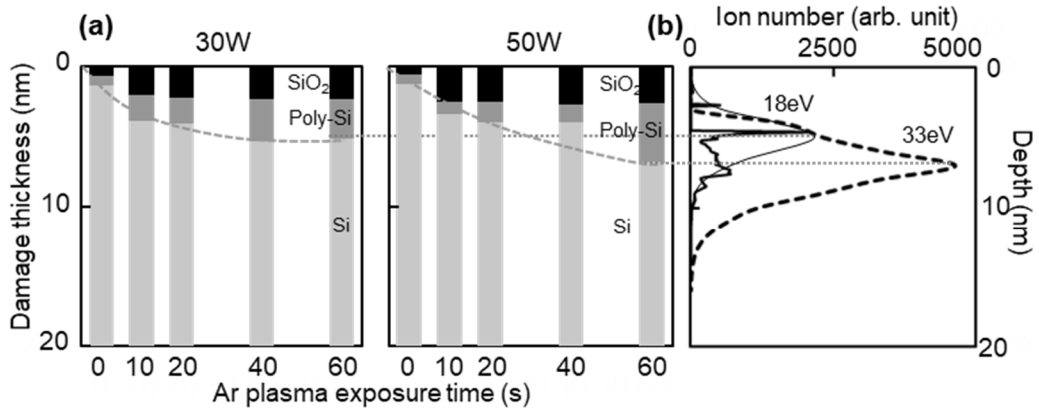


Fig. 8-5 (a) Damage thickness versus Ar desorption time, and (b) Depth profiles of Ar ion penetration in Si by TRIM simulation.

To confirm the relationship between V_{hp} and the damage thicknesses, measured by SE, we performed an additional experiment with a wide energy range and three different systems. A CCP system (Source: 60 MHz, Bias: 13.56 MHz), CCP system (Source: 60 MHz, Bias: 2 MHz), and ICP system (Source: 13.56 MHz, Bias: 400 kHz) were used in this study. We changed the processing time to keep a constant ion dose at 1.64×10^{17} (ion/cm²), and IEDF was obtained by simulation in the range from 0 to 1000 eV of V_{hp} . We confirmed that the thickness of the damaged layer was strongly related to the high energy peak of the IEDF, as shown in Fig. 8-6. There was a

correlation between the damage thickness and the square root of V_{hp} (damage thickness = $0.44 \times \sqrt{V_{hp}}$). The damage thickness has been reported to be related to the averaged voltage of IEDF¹⁶⁾. However, our results showed that the damage thickness is related to V_{hp} . We propose that this discrepancy was caused by the differences of optical models used for the damage analysis. Our model showed that the damage thickness was deeper than that of the previously published results.

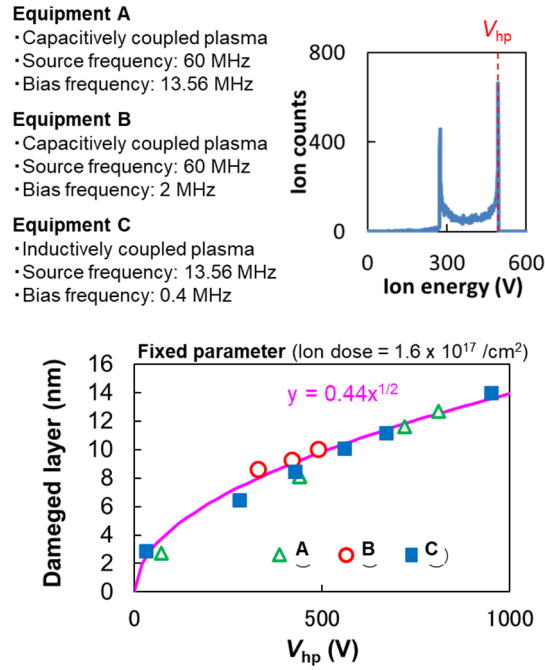


Fig. 8-6 Damage thickness versus high energy peak of ion energy distribution.

8.5 Damage reduction by a protective film

The HFC polymer was evaluated because it reduces the ion energy and has a protective film effect. To investigate the effect of the protective polymer on Si damage generation, the damage thickness with and without a polymer adsorption process was investigated. Figure 8-7 shows the T_{dam_total} as a function of Ar desorption time. There is a damage in the initial sample. It is a native oxide and underlying dislocated Si on Si substrate. The film thickness of the HFC

polymer on Si was 1.2 nm after adsorption (9 s). By applying the HFC polymer on the Si substrate, the damage thickness was decreased to approximately 1 nm. The ion energy at Si substrate can be greatly changed according to the upper HFC polymer¹⁷⁾. When the desorption time became longer, the damage became saturated, which resulted in no change in the thickness. The surface polymer can delay the damage generation process. After complete removal of the surface adsorbed polymer, the damage generation exhibited the same damage generation behavior as the samples without the adsorption step. Thus, a shorter desorption time resulted in a damage reduction. To satisfy the both requirements of the self-limited process and low-damage etching, we selected 30 seconds as the minimum value in the self-limited region (Fig. 8-2). ALE with the shortest desorption time in the self-limited region showed the least damage.

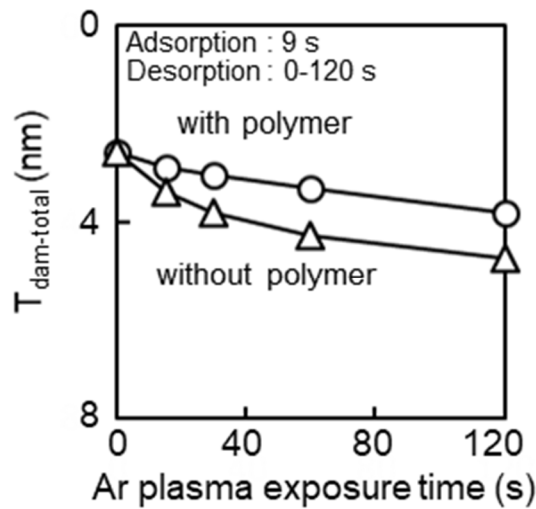


Fig. 8-7 Damage thickness without and with polymer.

Figure 8-8 shows the damage thickness as a function of cycle time of ALE. The desorption time was set at 30 s. It was clearly shown that the surface adsorption of the polymer could effectively reduce the damage generation during the ALE process. The desorption time was

the same as the Ar exposure time of 120 seconds and 4 cycles. Excess damage generation was suppressed by the sequential deposition of the protective film on the Si substrate (Fig. 8-9). Without adsorption, Si damage was generated from long-time Ar exposure. With adsorption, the adsorbed polymer could effectively reduce the underlayer Si damage, owing to the reduction of the ion energy in the polymer layer. Si damage generation was greatly suppressed by sequential deposition of the protective film in ALE.

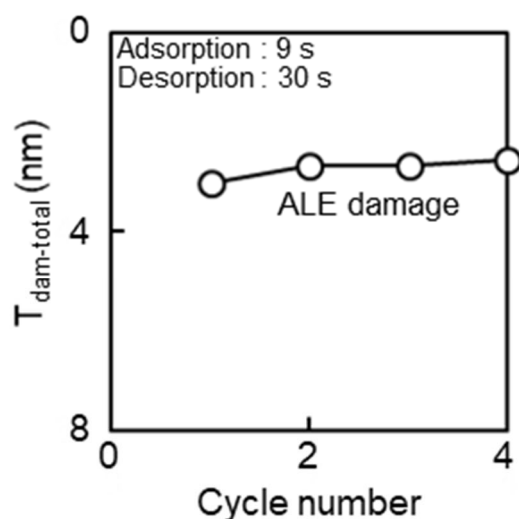


Fig. 8-8 Cycle number dependence of damage thickness after ALE process.

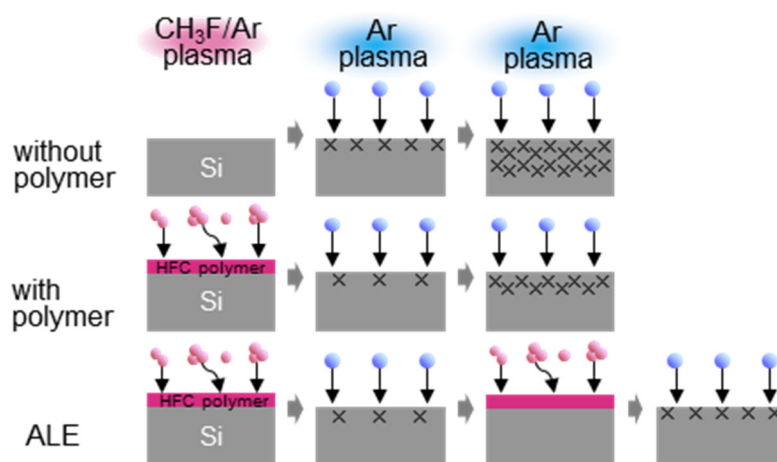


Fig. 8-9 Proposed model of damage reduction in ALE.

8.6 Conclusions

We investigated the underlying Si substrate damage generated during upper SiN ALE. Even in the case of ALE, damage was generated on the Si substrate, owing to the accumulation of incident ions. On-wafer IEDF measurement revealed that the damage thickness measured by SE was defined by the incident ion energy at the high energy peak of the IEDF. Adsorbed polymer can effectively reduce the underlying Si damage, owing to the ion energy loss in the polymer layer. Si damage generation was greatly suppressed by sequential deposition of a protective film during ALE. To suppress the damage generation during the ALE process, precise control of the ion energy, thickness of adsorbed polymer, and Ar desorption time are strongly required. For low-damage ALE, a very low ion energy is required. Therefore, a low electron temperature plasma source, high bias frequency, and low power generator are required. Additionally, precise control of V_{hp} in the IEDF is strongly required. Thus, measurement and prediction of the IEDF, and low-damage ALE equipment with a precise IEDF control system need to be developed.

8.7 References

- ¹ Y. Ishii, K. Okuma, T. Saldana, K. Maeda, N. Negishi, and J. Manos: Jpn. J. Appl. Phys. **56**, 06HB07 (2017).
- ² E. Holmström, A. Kuronen, and K. Nordlund: Physical Review B **78**, 045202 (2008).
- ³ M. V. Ramana Murty and H. A. Atwater: Phys. Rev. B **45**, 1507 (1992).
- ⁴ A. Hirata, M. Fukasawa, K. Kugimiya, K. Nagaoka, K. Karahashi, S. Hamaguchi, and H. Iwamoto: Journal of Vacuum Science & Technology A **38**, 062601 (2020).
- ⁵ M. Honda: Proc. IEEE Int. Interconnect Technology Conf. San Francisco, CA, 2005.
- ⁶ M. Haass, M. Darnon, G. Cunge, O. Joubert, and D. Gahan: J. Vac. Sci. Technol. B **33** (2015).
- ⁷ D. Gahan, S. Daniels, C. Hayden, D. O. Sullivan, and M. B. Hopkins: Plasma Sources Science and Technology **21**, 015002 (2012).
- ⁸ T. F. e. al.: Proc. The 40th International Symposium on Dry Process F-3 p 49. Nagoya, Japan, 2018.

CHAPTER 8

- ⁹ H. Ohta and S. Hamaguchi: J. Vac. Sci. Technol. A **19**, 2373 (2001).
- ¹⁰ M. Fukasawa, Y. Nakakubo, A. Matsuda, Y. Takao, K. Eriguchi, K. Ono, M. Minami, F. Uesawa, and T. Tatsumi: Journal of Vacuum Science & Technology A: Vacuum, Surfaces, and Films **29**, 041301 (2011).
- ¹¹ Y. Nakakubo, A. Matsuda, M. Fukasawa, Y. Takao, T. Tatsumi, K. Eriguchi, and K. Ono: Japanese Journal of Applied Physics **49**, 08jd02 (2010).
- ¹² J. F. Z. [<http://www.srim.org>].
- ¹³ J. F. Ziegler: Nucl. Instrum. Methods Phys. Res. B **219-220**, 1027 (2004).
- ¹⁴ J. P. Chang, J. C. Arnold, G. C. H. Zau, H.-S. Shin, and H. H. Sawin: J. Vac. Sci. Technol. A **15**, 1853 (1997).
- ¹⁵ D. C. Gray: Journal of Vacuum Science & Technology B: Microelectronics and Nanometer Structures **11** (1993).
- ¹⁶ K. Eriguchi, Y. Nakakubo, A. Matsuda, Y. Takao, and K. Ono: Jpn. J. Appl. Phys. **49** (2010).
- ¹⁷ T. Tatsumi, M. Matsui, M. Okigawa, and M. Sekine: J. Vac. Sci. Technol. B **18**, 1897 (2000).

CHAPTER 9

Summary

1) Mechanism of ITO etching using H₂ plasma

ITO has been widely used as a transparent electrode. In Chapter 3, the etch rate of ITO and the effects of a hydrogen-damaged layer caused by H₂/Ar plasma were investigated using several surface analysis techniques. The ITO etch rate in H₂/Ar plasma increased to about three times that with Ar plasma. ITO was reduced by incident hydrogen species in the H₂/Ar plasma, and an In-rich layer was formed on the surface. The In-rich layer had a higher sputtering yield, resulting in an increase in the etch rate in the H₂/Ar plasma. Thus, ITO etching is determined by the balance between the formation of an In-rich damaged layer by H ion irradiation and sputtering by relatively heavy inert gas ions.

2) Mechanism of ITO cyclic etching

To investigate the effect of hydrogen-induced modification on ITO etch rate increase, in Chapter 4, we demonstrated the cyclic thin-layer etching of ITO. Hydrogen plasma generates a modified layer on the ITO surface, which has a high etching rate in Ar plasma. The thickness of the modified layer was about 10 nm in V_{pp} 960 V. Only the hydrogen-induced modified layer of ITO can be etched by precisely controlling ion energy; the rate of etching the underlying non modified ITO is almost zero. Thus, the self-limiting etching of ITO was demonstrated. Cyclic etching was investigated using hydrogen plasma, followed by Ar plasma for highly selective etching of ITO/SiO₂. Silicon, which is generated from the top electrode, was deposited on the SiO₂ surface selectively during the cyclic process; the amount of deposited Si on the modified ITO surface was negligible. Therefore, highly selective etching of ITO over SiO₂ (mask material) can be achieved by the selective surface adsorption of a protective film. And it was suggested that cyclic etching by selective surface adsorption of Si can precisely control the etch rates of ITO and

SiO₂, resulting in an almost infinite selectivity for ITO over SiO₂ and in improved profile controllability.

3) Damage recovery and low-damage ITO etching

H₂ plasma required for ITO etching reduced the ITO surface and damaged it in the form of generating metallic-In. To investigate the damage recovery, in Chapter 5, potential of O₂ plasma and the potential of using H₂/CO plasma as a low-damage etching technique was studied. Damage recovery for device fabrication was possible using H₂/CO plasma, O₂ plasma caused excess oxidation of the ITO surface. When using H₂/CO plasma, the final resistivity was close to that of the initial sample. Simultaneous injection of hydrogen and oxygen recovered the reduced ITO to its initial state. The etch rate of the ITO was thus increased by the mixture of hydrogen and oxygen plasma compared with O₂ single gas and H₂ single gas. The He ion injection generated a polycrystalline ITO surface, the number of grain boundaries increased. We concluded that the increase of the ITO sputter rate was caused by both generations of metallic-ITO via the reduction of ITO and an increase in the number of grain boundaries. Patterned samples were etched by the H₂/CO/Ar plasma without any residue remaining and without any sidewall roughness. The addition of Ar eliminates the residues on the underlayer, due to the increase of physical sputtering effect. With hydrogen and oxygen-mixed plasma, we were able to achieve low-damage etching by controlling the balance between surface reduction and oxidation. Thus, mixed hydrogen and oxygen gas chemistry is a potential candidate for achieving low damage ITO etching as well as for achieving a damage recovery process after etching with hydrogen-containing plasma

4) Surface reaction mechanism of SiN ALE

ALE has been studied extensively for surface reactions, and thus, little has been reported about the fluctuation of ALE performances in device fabrication. In Chapter 6, we investigated SiN ALE with process optimization of the adsorption and desorption steps, and we focus on the cycle number dependence of EPC fluctuation of ALE. We also studied the ALE performance variation caused by the chamber wall conditions. Excess polymer deposition, which originates from residual carbon after desorption step, causes the etch stop of SiN ALE. The reason of residual carbon is that the HFC polymer, which has many C–C bonds, is difficult to sputter. Thus, a thick carbon layer causes an etch stop, and suppression of C deposition is required for stable SiN ALE. Addition of O₂ to the desorption step or a three-step O₂ ashing process can suppress C deposition and realize stable ALE. The high EPC of the three-step ALE was caused by the presence of abundant fluorine atoms in the HFC during Ar desorption, compared with O₂/Ar desorption. Hence, the three-step ALE is appropriate for device manufacturing. CF_x desorption from the chamber wall causes etch enhancement of ALE. The desorbed CF₂ enhance the EPC at the wafer edge during Ar desorption. We found that control of fluorine and carbon amounts is critical for stable SiN ALE. To realize stable SiN ALE, it is necessary to keep the same surface conditions in every cycle. It is also important to control the influence of desorbed species from the chamber components.

5) Stabilization of SiN by multi-step ALE

To investigate the effect of the surface conditions, in Chapter 7, we studied stabilization of the EPC in SiN ALE by using an ICP system. And we investigated the etch-stop mechanism in SiN ALE and examined multi-step ALE for stabilization. Etch-stop of SiN ALE is caused by polymer deposition. MD simulation shows that Si–C bonds remain on the SiN surface after the

ALE process. The remaining Si–C bonds are a trigger for carbon accumulation, which is generated during the ALE cycles. The etch-stop is suppressed with an O₂ flash step. However, the EPC decreases after one cycle of ALE, which is caused by the surface oxidation of SiN. For a stable ALE process, the surface SiO₂ is removed by SiO₂ ALE. By optimizing the SiO₂ ALE sequence, a quasi-self-limited behavior of SiO₂ ALE is realized. By combining the three-step SiN ALE with a subsequent SiO₂ ALE to remove residual SiO₂, multi-step ALE is realized. The EPC of SiN is approximately equal to that of SiO₂. Non-selective ALE is developed for next-generation devices. To stabilize the ALE process, because ALE is extremely sensitive to the surface conditions, understanding and precise control of the plasma–surface interactions are critical.

6) Mechanism of ALE damage generation

In Chapter 8, we investigated the underlying Si substrate damage generated during upper SiN ALE. Even in the case of ALE, damage was generated on the Si substrate, owing to the accumulation of incident ions. On-wafer IEDF measurement revealed that the damage thickness measured by SE was defined by the incident ion energy at the high energy peak of the IEDF. Adsorbed polymer can effectively reduce the underlying Si damage, owing to the ion energy loss in the polymer layer. Si damage generation was greatly suppressed by sequential deposition of a protective film during ALE. To suppress the damage generation during the ALE process, precise control of the ion energy, thickness of adsorbed polymer, and Ar desorption time are strongly required. For low-damage ALE, a very low ion energy is required. Therefore, a low electron temperature plasma source, high bias frequency, and low power generator are required. Additionally, precise control of V_{hp} in the IEDF is strongly required.

Research Achievement

Refereed Journals

[1] Akiko Hirata, Masanaga Fukasawa, Jomar U. Tercero, Katsuhisa Kugimiya, Kojiro Nagaoka, Kazuhiro Karahashi, Satoshi Hamaguchi and Hayato Iwamoto: “Plasma-enhanced conversion atomic layer etching for stable etched amount per cycle in SiN etching”, Jpn. J. Appl. Phys. in preparation.

[2] Hu Li, Kazuhiro Karahashi, Akiko Hirata, and Satoshi Hamaguchi: “Effects of hydrogen radicals on the surface reactions of Zinc oxide etching by hydrocarbon plasmas”, J. Vac. Sci. Technol. in preparation.

[3] Akiko Hirata, Masanaga Fukasawa, Katsuhisa Kugimiya, Kojiro Nagaoka, Kazuhiro Karahashi, Satoshi Hamaguchi, and Hayato Iwamoto: “Mechanism of SiN etching rate fluctuation in atomic layer etching”, J. Vac. Sci. Technol. A 38, 062601 (2020).

[4] Akiko Hirata, Masanaga Fukasawa, Katsuhisa Kugimiya, Kojiro Nagaoka, Kazuhiro Karahashi, Satoshi Hamaguchi and Hayato Iwamoto: “On-wafer monitoring and control of ion energy distribution for damage minimization in atomic layer etching processes”, Jpn. J. Appl. Phys. 59, SJJC01 (2020).

[5] Akiko Hirata, Masanaga Fukasawa, Katsuhisa Kugimiya, Kazuhiro Karahashi, Satoshi Hamaguchi and Kojiro Nagaoka: “Damage recovery and low-damage etching of ITO in H₂/CO plasma: Effects of hydrogen or oxygen”, Plasma Process. Polym. 16 (2019) 1900029.

[6] Akiko Hirata, Masanaga Fukasawa, Kazunori Nagahata, Hu Li, Kazuhiro Karahashi, Satoshi Hamaguchi, and Tetsuya Tatsumi: “Cyclic etching of tin-doped indium oxide using hydrogen-induced modified layer”, Jpn. J. Appl. Phys. 57, 06JB02 (2018).

[7] Hu Li, Kazuhiro Karahashi, Pascal Friederich, Karin Fink, Masanaga Fukasawa, Akiko Hirata, Kazunori Nagahata, Tetsuya Tatsumi, Wolfgang Wenzel, and Satoshi Hamaguchi: “Enhanced etching of tin-doped indium oxide due to surface modification by hydrogen ion injection”, Jpn. J. Appl. Phys. 57, 06JC05 (2018).

[8] Akiko Hirata, Masanaga Fukasawa, Takushi Shigetoshi, Masaki Okamoto, Kazunori Nagahata, Hu Li, Kazuhiro Karahashi, Satoshi Hamaguchi, and Tetsuya Tatsumi: “Effects of hydrogen-damaged layer on tin-doped indium oxide etching by H₂/Ar plasma”, Jpn. J. Appl. Phys. 56, 06HD02 (2017).

[9] Hu Li, Kazuhiro Karahashi, Pascal Friederich, Karin Fink, Masanaga Fukasawa, Akiko Hirata, Kazunori Nagahata, Tetsuya Tatsumi, Wolfgang Wenzel, and Satoshi Hamaguchi: “Effects of hydrogen ion irradiation on zinc oxide etching”, J. Vac. Sci. Technol. A 35, 05C303 (2017).

International conferences (Oral)

- [1] Akiko Hirata: “Reduction of Process-induced damage in atomic layer etching”, 20th International Workshop on Junction Technology 2021, On-line, (2021/6/10-2021/6/11). **(Invited)**
- [2] Akiko Hirata, Masanaga Fukasawa, Jomar Tercero, Katsuhisa Kugimiya, Kojiro Nagaoka, Kazuhiro Karahashi, Satoshi Hamaguchi, and Hayato Iwamoto: “Plasma-enhanced conversion atomic layer etching for stable etched amount per cycle in SiN etching”, 12th EU-Japan Joint Symposium on Plasma Processing, On-line, (2021/4/2).
- [3] Akiko Hirata: “Highly selective atomic layer etching for semiconductor application”, 7th International Atomic Layer Etching Workshop, On Demand, ALE1-TuM3, (2020.06.29-07.01). **(Invited)**
- [4] Akiko Hirata, Masanaga Fukasawa, Katsuhisa Kugimiya, Kazuhiro Karahashi, Satoshi Hamaguchi, Kojiro Nagaoka, and Hayato Iwamoto: “On-wafer monitoring of ion energy distributions and precise ion energy control (< 100 eV) for damage reduction in atomic layer etching”, 41st International Symposium on Dry Process, Hiroshima, A-3, (2019/11/21).
- [5] Akiko Hirata, Masanaga Fukasawa, Katsuhisa Kugimiya, Kazuhiro Karahashi, Satoshi Hamaguchi, and Kojiro Nagaoka: “The mechanism of SiN etching rate fluctuation in atomic layer etching”, AVS 66th International Symposium, Columbus, Ohio, PS+2D+EM+SS+TF-ThA03, (2019/10/24).
- [6] Akiko Hirata, Masanaga Fukasawa, Kazunori Nagahata, Hu Li, Kazuhiro Karahashi, Satoshi Hamaguchi and Tetsuya Tatsumi “Cyclic etching of ITO using controlled modified-layer”, 39th International Symposium on Dry Process E-1, Tokyo, (2017/11/17).
- [7] Akiko Hirata, Masanaga Fukasawa, Takushi Shigetoshi, Masaki Okamoto, Kazunori Nagahata, Hu Li, Kazuhiro Karahashi, Satoshi Hamaguchi and Tetsuya Tatsumi: “Effects of hydrogen-damaged-layer on ITO etching by H₂/Ar plasma”, 38th International Symposium on Dry Process C-2, Hokkaido, (2016/11/21).

Domestic (Japanese) conferences (Oral)

- [1] 平田 瑛子、深沢 正永、釘宮 克尚、萩本 賢哉、岩元 勇人、Jomar U. Tercero、磯部 倫郎、伊藤 智子、唐橋 一浩、浜口 智志：「SiN Atomic Layer Etching の H ダメージ解析」 第 81 回応用物理学会 秋季学術講演会、オンライン開催、11p-Z03-6 (2020/9/11).
- [2] 平田 瑛子、深沢 正永、釘宮 克尚、長岡 弘二郎、岩元 勇人、唐橋 一浩、浜口 智志：「ALE プロセスでのダメージ最小化に向けたイオンエネルギー分布のオンウエハモ

ニタリングと制御」シリコンテクノロジー分科会第 223 回研究集会, 東京大学, (2020/02/14) (招待講演).

[3] 平田 瑛子, 深沢 正永, 釘宮 克尚, 長岡 弘二郎, 唐橋 一浩, 浜口 智志:「SiN Atomic Layer Etching 表面状態の変動解析」第 80 回応用物理学会 秋季学術講演会、北海道大学 札幌キャンパス、20p-N304-10 (2019/9/20).

[4] 平田 瑛子:「ITO の表面反応メカニズムとサイクル加工」 第 80 回応用物理学会 秋季学術講演会、北海道大学 札幌キャンパス、18a-C309-5 (2019/9/18) (招待 応用物理学会優秀論文賞受賞記念講演).

[5] 平田 瑛子:「ITO の表面反応メカニズムとサイクル加工」 第 4 回 Atomic Layer Process (ALP) Workshop 大阪大学 中之島センター (2019/6/21) (招待講演).

[6] 平田 瑛子:「異分野から半導体業界へのチャレンジ」第 68 回応用物理学会 春季学術講演会 特別シンポジウム 就活生必見！知ってますか？エレクトロニクス産業が拡大し続けていることを！ ～日本が支える世界のスマート化社会と若手エンジニアが語る「やりがい」～ 11a-W241-4 (2019/03/11) (招待講演).

[7] 平田 瑛子, 深沢 正永, 長畑 和典, 李 虎, 伊藤 智子, 浜口 智志, 辰巳 哲也:「H による変質層を用いた ITO エッチレートの高精度制御」 第 78 回応用物理学会 秋季学術講演会 7p-A402-2 (2017/09/07).

[8] 平田 瑛子, 深沢 正永, 重歳 卓志, 岡本 正喜, 長畑 和典, 李 虎, 浜口 智志, 辰巳 哲也:「H₂/Ar プラズマによる ITO エッチングに対する水素変質層の効果」 第 63 回応用物理学会 春季学術講演会 19p-W621-6 (2016/03/19).

Domestic (Japanese) conference (Poster)

[1] 平田 瑛子, 深沢 正永, 釘宮克尚, 長岡弘二郎, 辰巳哲也, 唐橋一浩, 浜口智志:「表面変質層を用いた ITO 加工メカニズム解明とサイクル加工への応用」 応用物理学会 界面ナノ電子化学研究会 第 4 回ポスター発表展 (2019/03/11).

Other conferences (Co-author)

- [1] Jomar Tercero, Akiko Hirata, Michiro Isobe, Masanaga Fukasawa, Magdaleno Vasquez, Jr., and Satoshi Hamaguchi: “Etch-stop mechanisms in plasma-assisted atomic layer etching of silicon nitride: a molecular dynamics study”, 21st International Conference on Atomic Layer Deposition, Tampa, Florida, (2021/6/27-2021/6/30).
- [2] Jomar Tercero, Akiko Hirata, Michiro Isobe, Masanaga Fukasawa, Magdaleno Vasquez, Jr., and Satoshi Hamaguchi: “Effect of Hydrogen in the Plasma-Enhanced Atomic Layer Etching of Silicon Nitride: A Molecular Dynamics Study”, 第 68 回 応用物理学会 春季学術講演会、オンライン開催 (2021/3/16-2021/3/19).
- [3] Jomar Tercero, Michiro Isobe, Tomoko Ito, Kazuhiro Karahashi, Akiko Hirata, Masanaga Fukasawa, and Satoshi Hamaguchi: “Mechanisms of Excess Deposition of Carbon in SiN Atomic-Layer Etching (ALE) by Hydrofluorocarbon Plasmas; Comparison between Molecular Dynamics (MD) simulation and Experiments”, AVS 67th International Symposium. 開催中止
- [4] Kazuhiro Karahashi, Hu Li, Michiro Isobe, Kohei Mizotani, Shunpei Shigeno, Masanaga Fukasawa, Akiko Hirata, Tetsuya Tatsumi, and Satoshi Hamaguchi: “Effects of light Ion (H^+ and He^+) Irradiation in Plasma Etching process”, AVS 65th International Symposium, PS+EM+NS+SS-TuA12, Long Beach, CA, (2018/10/23).
- [5] Hu Li, Kazuhiro Karahashi, Akiko Hirata, Masanaga Fukasawa, Kazunori Nagahata, Tetsuya Tatsumi, Pascal Friederich, Karin Fink, Wolfgang Wenzel, and Satoshi Hamaguchi: “Etching Mechanisms of ITO by Low Energy Hydrocarbon ions”, 39th International Symposium on Dry Process P-7, Tokyo, (2017/11/17).
- [6] 李 虎, 伊藤 智子, 唐橋 一浩, 深沢 正永, 平田 瑛子, 長畑 和典, 辰巳 哲也, 浜口 智志: 「 He^+ イオン照射により前処理された ZnO エッチング機構の解明」 第 78 回 応用物理学会 秋季学術講演会、7a-A402-3 (2017/09/07).

Awards

- [1] 第 41 回 応用物理学会 優秀論文賞 2019
- [2] 応用物理学会 界面ナノ電子化学研究会 第 4 回 ポスター発表展 2019, 優秀講演賞
- [3] 39th International Symposium on Dry Process 2017, Young Researcher Award

Patents

- [1] 特開 2020-113637 「酸化物半導体膜のエッチング方法および酸化物半導体加工物ならびに電子デバイス」 発明者：平田瑛子、深沢正永
- [2] 特開 2019-197773 「酸化物半導体膜のエッチング方法」 発明者：平田瑛子、深沢正永
- [3] 特開 2019-003234 「酸化物半導体膜のエッチング方法」 発明者：平田瑛子、辰巳哲也、深沢正永、浜口智志、唐橋一浩

Newsletter

- [1] 平田瑛子：「応用物理学会優秀論文賞を受賞して」 プラズマエレクトロニクス分科会・会報（No.71）.

Acknowledgments

I would like to express my gratitude to Prof. Satoshi Hamaguchi, for helpful discussions and comments on the manuscript. I am thankful for giving me the opportunity to collaborate research and support of consideration. I am sincerely grateful to Prof. Kazuhiro Karahashi for thoughtful advice on analyzing the beam experiment data. I also thank to Prof. Tomoko Ito, Dr. Michiro Isobe, Dr. Hu Li, and Mr. Jomar U. Tercero at Osaka University for discussions on analyzing the beam experiment data and MD simulation.

I would like to show my greatest appreciation to Dr. Masanaga Fukasawa for experiment and discussions helped me to further improve my research. I would like to thank Mr. Katsuhisa Kugimiya, Mr. Yoshiya Hagimoto, and Mr. Hayato Iwamoto at Sony Semiconductor Solutions Corporation for their fruitful discussions. I am thankful for giving me the opportunity to collaborate with the Osaka university and academic career.